POLITECNICO
MILANO 1863

SCUOLA DI INGEGNERIA INDUSTRIALE E
DELL'INFORMAZIONE
Laurea Magistrale in Ingegneria Meccanica

# Numerical analysis of wind-break fences for road vehicle stability in crosswind

Supervisor: Prof. Paolo SCHITO
Prof. Michele VIGNATI

Candidate: Emanuele PELLEGRINO
Student ID: 920459

**Academic Year 2019-2020**

---

Politecnico di Milano:
www.polimi.it

School of Industrial and Information Engineering:
www.ingindinf.polimi.it

*“Nella vita non conta tanto dove arrivi,*
*quanto chi ti accompagna lungo il cammino.”*

*Ai miei genitori e Zio Giovanni che mi*
*hanno insegnato a camminare.*
*A Chiara e Sandro che mi hanno*
*accompagnato in questi 5 anni.*

# Acknowledgements

I would have never had the chance to work on this thesis without the influence and support of a number of inspiring individuals met in my academic journey. I would like to thank my supervisor Prof. Paolo Schito for supporting me with enthusiasm and optimism during this work despite the complex historical period and I also want to express my gratitude to my co-supervisor Prof. Michele Vignati for providing me many valuable inputs for this thesis. I gratefully acknowledge Prof. Mauro Filippini without whom I would have never had the possibility to attend the amazing lectures on the aerodynamics of road vehicles from Prof. Christian Navid Nayeri and Prof. Lennart Löfdahl in TU-Berlin. I am forever thankful to my Milanese family of Chiara and Sandro, to Cesare and to my colleagues Paolo and Leonardo for supporting me from the beginning to the end of my PoliMi journey. I feel blessed to have had such a great day-by-day support during this work from my girlfriend Katia and my sister Sidonie to whom I am grateful. Finally, my deep and sincere gratitude to my parents and Zio Giovanni, for their continuous and unparalleled love, help and support.

*Milano, April 2021* E. P.

# Contents

# List of Figures

# List of Tables

# Sommario

In questo lavoro è stata studiata l'efficacia di una coppia di barriere frangivento appositamente progettate per far fronte a un improvviso forte vento laterale per un modello di camion e di auto.

Secondo quanto riportato dall'ISTAT [1], nel 2018 sulle strade italiane sono avvenuti 271 incidenti gravi o mortali a causa del forte vento, argomento cruciale nella progettazione d'infrastrutture in siti extraurbani particolarmente esposti, come ponti e viadotti.

Questo studio nasce dall'ipotesi che ci siano svariati casi in cui il pericolo sia dovuto più allo sviluppo improvviso dei carichi aerodinamici che al valore stazionario del vento, che risulterebbe invece gestibile dal conducente.

Due differenti modelli di barriere frangivento basate sui progetti di Tagliavia Ramírez [2] sono state disegnate e testate. Entrambi i modelli vedono la propria altezza diminuire ogni 12,5 m, così da far aumentare gradualmente i carichi aerodinamici e allungare il transitorio di sviluppo degli stessi. L'efficacia di queste barriere è stata studiata riproducendo uno scenario realistico, comparando la risposta dinamica dei due veicoli a un forte vento laterale in uscita da una galleria con e senza le barriere. Questa comparazione è stata realizzata accoppiando simulazioni CFD con mesh in movimento (validate in galleria del vento) e modelli di dinamica del veicolo, studiando l'influenza di numerosi parametri attraverso la definizione di due indici di sicurezza e confrontando lo spostamento laterale massimo.

Entrambi i modelli di barriera hanno mostrato una grande efficacia sul camion, riducendo lo spostamento laterale massimo del -14,8% e -34,5% rispettivamente nel caso più critico. Similmente è avvenuto per l'auto, con riduzioni del -16,4% e -35,9%, anche se quest'ultima è molto meno soggetta al forte vento laterale. Il risultato chiave si è ottenuto studiando l'influenza del peso del camion: aumentando quest'ultimo infatti, aumenta anche l'instabilità al rollio del veicolo. Per questa ragione sono stati effettuati dei test tenendo costanti $v_{veicolo} = 25\,\mathrm{m/s}$ e $U_{vento} = 30\,\mathrm{m/s}$, per $m = 0,5m_{max}$, $m = 0,75m_{max}$ e $m = m_{max}$. Senza barriere a fine galleria, il camion invade la corsia adiacente quando $m = 0,5m_{max}$ e si ribalta quando $m = m_{max}$. Entrambi i modelli di barriera si sono dimostrati efficaci riducendo notevolmente lo spostamento laterale quando $m = 0,5m_{max}$ ed evitando il ribaltamento quando $m = m_{max}$, dimostrando l'ipotesi a monte di questa tesi.

A conclusione di questo studio, sono state condotte alcune promettenti analisi sul simulatore di guida dinamico DiM400 che hanno aperto nuovi orizzonti per le future ricerche sull'argomento.

**Keywords:** Forte Vento Laterale, Barriere Frangivento, CFD, Galleria del Vento, Aerodinamica, Dinamica del Veicolo, Simulatore di Guida Dinamico Dim400.

# Abstract

In this work, the effectiveness of two designed wind-break fences on a sudden strong crosswind has been investigated for a truck and a car.

According to ISTAT [1], in 2018, 271 accidents causing death or personal injuries happened on the Italian roads due to strong wind, that is a crucial topic when designing exposed sites outside urban areas such as viaducts and bridges.

This study has been driven by hypothesis that there are many cases in which the danger is due more to the sudden rise of the aerodynamic loads rather than to the steady state value of the wind which can be, instead, managed by a driver.

Two different wind-break fences based on the work of Tagliavia Ramírez [2] have been designed. Both the models decrease their height each 12,5 m to let the aerodynamic loads increase smoothly and so stretch the transient time of rise of these loads. The effectiveness of these fences has been studied in a realistic scenario case study; a comparison of the dynamic responses of the two vehicles to a strong crosswind while leaving a tunnel with and without the fences has been made. This has been done through to the coupling of moving mesh CFD simulations (validated in a wind tunnel) and vehicle dynamics simulations, studying the influence of many parameters via the definition of two safety indices and comparing the maximum lateral displacement.

Both the fences models have shown a great effectiveness on the truck model, reducing the maximum lateral displacement of -14,8% and -34,5% respectively in the most critical case. Similar results have been obtained for the car model (even if this last resulted to be much less affected by crosswind), with a reduction of -16,4% and -35,9%. The key result has been obtained studying the influence of the weight of the truck: increasing this last, also the roll instability of the truck increases. For this reason some tests have been done keeping $v_{vehicle} = 25\,\mathrm{m/s}$ and $U_{wind} = 30\,\mathrm{m/s}$, for $m = 0,5m_{max}$, $m = 0,75m_{max}$ and $m = m_{max}$. When no fences are placed at the end of the tunnel, the truck undergoes a tremendous lateral displacement (invading the contiguous lane) when $m = 0,5m_{max}$, and rolls over when $m = m_{max}$. Both the fences have shown the capability to reduce significantly the lateral displacement when $m = 0,5m_{max}$ and avoiding the roll over when $m = m_{max}$, demonstrating the hypothesis behind this thesis.

At the end of the work, some promising preliminary analyses on the Dim400 dynamic driving simulator have been conducted, thus opening up new horizons for the future researches on this topic.

**Keywords:** Crosswind, Wind-break Fences, CFD, Wind Tunnel, Aerodynamics, Vehicle Dynamics, Dim400 Dynamic Driving Simulator.

# Introduction

## 0.1 Introduction to the Framework

According to ISTAT [1], in 2018, 271 accidents causing death or personal injuries happened on the Italian roads due to strong wind, 35,79% of whom outside urban areas. These are only 0,15% of the 2018 total number of road accidents, but are 11,09% of the accidents linked to one bad weather condition excluding rain. Considering then that 10113 other accidents (5,86% of the total) happened due to the combination of two or more bad weather conditions and that 37,16% of these happened outside urban areas, it is reasonable to state that crosswind is not only one of the main causes of road vehicles accidents due to weather conditions, but also a crucial topic when designing exposed sites outside urban areas such as embankments, viaducts and bridges.

According to the work of Salati [3], high-sided lorries and trucks, especially when crossing the mentioned sites, can be at risk of wind-induced accidents like overturning and/or side-slip. It is reasonable so, to imagine that also other vehicles could be in danger under these conditions. While driving a car at high speed on a highway, one may easily experience the sudden response of the vehicle due to crosswind and sometimes the necessity of a very skilled driver action to overcome a danger situation. Taking as a reference the Italian road regulations, crosswind is reported with a danger signal that implies to proceed with caution, take care of possible vehicles out of control and slow down [4].

For all these reasons, it has been found of particular interest the study of barriers such as wind fences that could mitigate these problems.

In the present work, vehicle dynamics and aerodynamics are coupled through dynamic mesh CFD simulations and complex numerical vehicle dynamics model. By means of these tools, the study of the response of the vehicles to crosswind as well as the analysis of the effectiveness of two kinds of wind barriers based on the work of Tagliavia Ramírez [2] will be presented.

The present thesis work has been developed at Politecnico di Milano in the frame of the Alliance4Tech programme thanks to which a portion of the experimental part has been conducted in a previous experience at TU-Berlin.

## 0.2 The Role of Aerodynamics in Vehicle Design

After approximately one century of research, aerodynamics is well known as a crucial topic for the design of both vehicles and infrastructure. Taking as a

reference the design of a car, there are many properties affected by aerodynamics. The first things that are common to think about are related to the performance of the vehicle both in terms of top speed and fuel economy (and so emissions); both are determined by aerodynamic drag. However, even if fundamental, drag is only one of the several aspects to consider when designing a vehicle. In Figure 1 it is reported a list of the main tasks of vehicle aerodynamics.

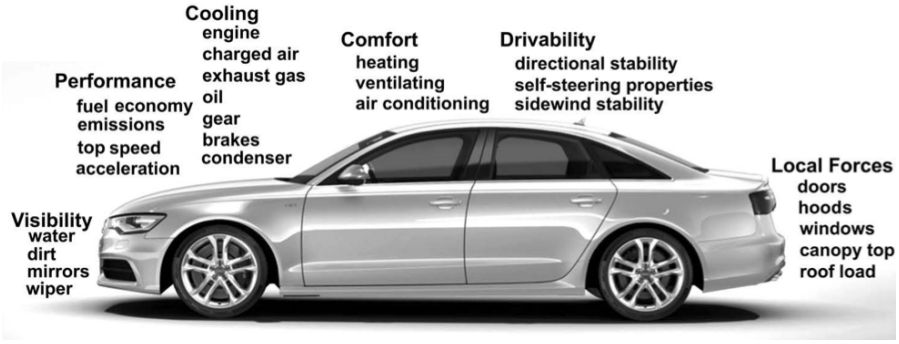


**Figure 1:** Spectrum of tasks for vehicle aerodynamics [5]

The flow processes to which a moving vehicle is subjected fall into three categories [5]:

1. Flow of air around the vehicle;
2. Flow of air through the body of the vehicle;
3. Flow processes within the machinery of vehicle.

Being this work focused on crosswind, it is important to stress that the flow around a vehicle is responsible for its directional stability in terms of straight line stability, dynamic passive steering and response to crosswind. Obviously not only the shape and so the kind of vehicle, but also the shape of the infrastructure has a wide influence on the aerodynamic of the vehicle and so on its handling performances [5–7].

### 0.2.1 A Bit of History

To better understand how the role of aerodynamics has changed so much during the last century and why today this is a crucial topic, it is worth mentioning briefly the history of aerodynamics in the automotive sector.

At the beginning of the automotive industry era, aerodynamics has been viewed with scepticism. The first reason was that for cars, there weren't examples to follow from nature like birds for planes and fish for ships and trying to borrow shapes from these last turned out to be wrong. Breakthroughs in automobile aerodynamics came only when they broke away from these improper examples [5]. The second main reason was that it was too early to see results from the change of the shape of a vehicle since at that time cars were quite slow; nowadays it is well known that the

influence of drag resistance starts to become predominant above around 70 km/h as well described in Figure 2.

Another key aspect to be kept in mind is that from the beginning to the sixties, aerodynamic studies were done by individuals, often coming from outside the automotive industry. After the Second World War, due to the collapse of the oil price, there was a lack of interest in commercial vehicle aerodynamics, leading this field to be a peculiarity of sport cars. Only in the seventies, commercial car companies started taking over the discipline of vehicle aerodynamics inside the car development teams. This is probably linked not only to the growing complexity and performances of the commercial vehicles, but also to the 1973 oil crisis. With the increase of the oil price, lowering the drag resistance and so the consumptions became a pressing need. This could be considered the starting point for all the subsequent researches and studies that led the industry to the current point.

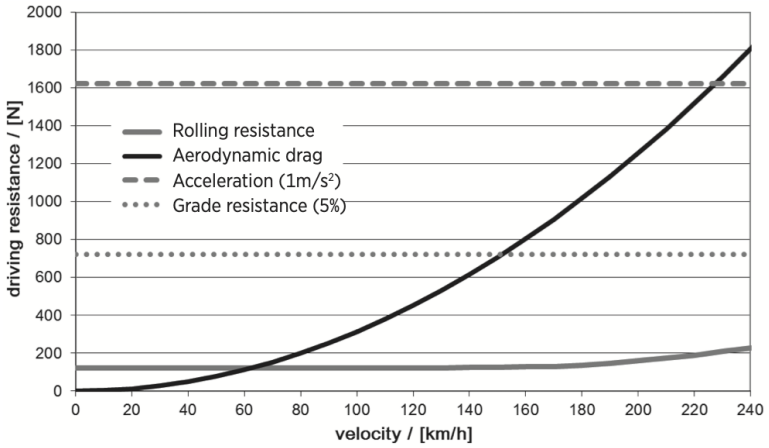


**Figure 2:** Progressional plotted curvature of air and rolling resistance as well as acceleration and grade resistance in relation to speed [5]

Among all the contributions, there is one that could be considered a milestone in vehicle aerodynamics studies: the work of Ahmed and Ramm [8]. From 1984 on the so-called "Ahmed body" (Figure 3), a simplified vehicle model, has become a standard for the study of the wake of vehicles inside as well as outside academic environments.

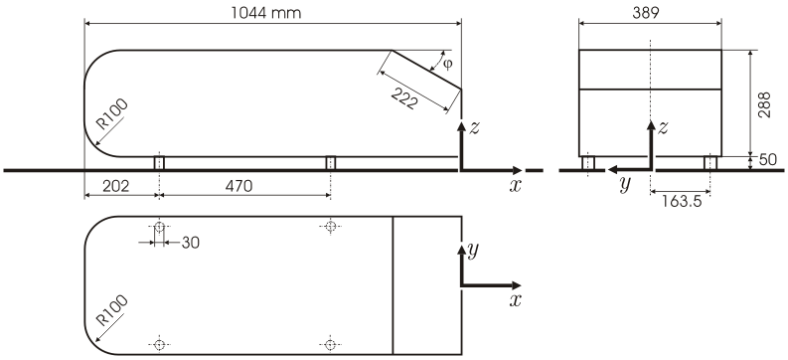


**Figure 3:** Design of an Ahmed body

It is easy to notice that almost all the mentioned investigations aimed to reduce the drag resistance, but as stated at the beginning of this section, drag is only one of the aspects to consider when designing a vehicle. Another key parameter, related to directional stability and so to the handling performances and the safety of vehicles, is the side force. In the last 30 years, this consequence of the crosswind on vehicles has been studied more in depth, mostly in an academic way, focusing more on trains than road vehicles. The main object of these studies has been the effect that crosswind can have on trains and in heavy road vehicles when exposed to strong gusts of wind, in areas such as viaducts and embankments.

For what concerns the tools developed to investigate air flows around vehicles, it is a wrong belief that wind tunnels are something new, being the first wind tunnel designed in 1871 [9] and being used since 1934 to test vehicles (as shown in Figure 4), but nevertheless, as it will be better explained in Section 1.4.1, it remains of fundamental importance and validity. In the last 30 years, a new tool has become more and more reliable: the computational fluid dynamics simulation, better known as CFD. This tool has given the chance of reducing significantly the cost of the design and test phase and the opportunity to increase the range of the possible researches. Since CFD have a central role in this work, it is worth dedicating an entire section to better explain how this tool turned out to be revolutionary for the aerodynamics studies; for this reason, in Section 1.4 an overview on both CFD and wind tunnel tests is reported.

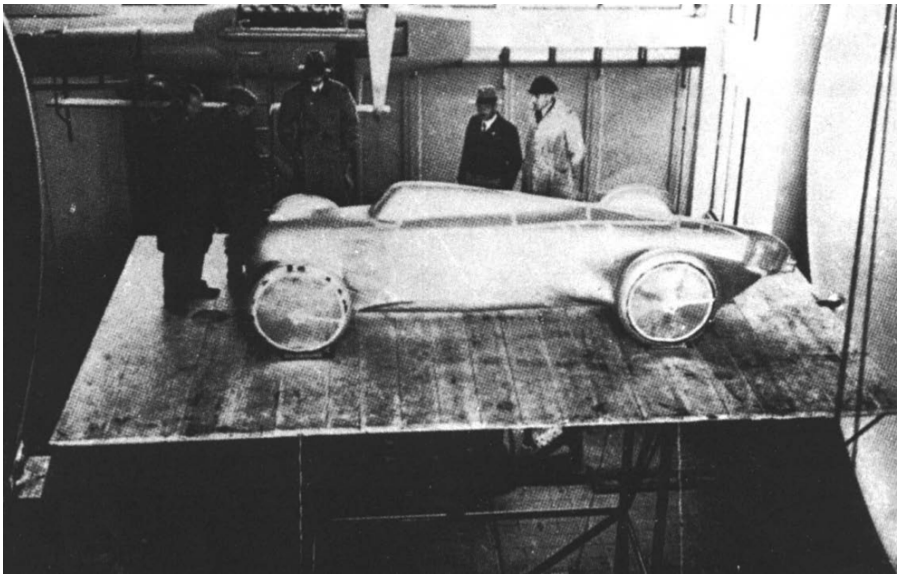

**Figure 4:** An Auto Union racing car in the wind tunnel of DVL in Adlershof, Berlin, 1934 [10]

## 0.3 State of the Art

According to the work of Salati [3], vehicles, in particular high-sided lorries and trucks, can be at risk of wind-induced accidents such as overturning and/or side-slip, especially on exposed sites such as embankments, viaducts and bridges.

For this reason, in the last 30 years many studies have been developed to estimate and mitigate the risk of crosswind-induced road accidents [2, 11–24].

The majority of the works mentioned refer to high-sided road vehicles like trucks, but thanks to the work developed in the last ten years in the German academic environments, some studies related to crosswind on a 1:4 scale car model (the "DrivAer") can be found. Some interesting examples are the one developed in TU-Berlin and TU-Munich by Strangfeld et al. [22], Wieser, Nayeri, and Paschereit [23] and Wieser et al. [25].

Due to the complexity of the vehicle dynamics model, there is little examples of studies of motorcycles under crosswind; an interesting study is the one made by Fintelman et al. [20]. On the other hand, the scientific literature is full of studies concerning the crosswind effects on rail vehicles like 'Cross-wind effects on road and rail vehicles'[26]. However, both motorcycles and trains are out of the scope of this work and for this reason these works are reported just as a reference.

A possible solution to the mentioned risks related to crosswind is to protect vehicles with specific designed fences. This is a particularly challenging topic since requires the coupling between two models representing aerodynamic forces and vehicle dynamic response (with or without a driver model). However, in the last decade, some interesting preliminary studies had shown the possible effectiveness of this solution [2, 3, 19, 27]. The two main difficulties when approaching to this problem are related to the correct estimation of the aerodynamic loads and to the accurate simulation of the dynamic response of the vehicles as explained in Baker et al. [26]. Concerning the first issue, the aerodynamic loads are generally obtained through CFD models like in the work of Tagliavia Ramírez [2] Alonso-Estébanez et al. [27] and Fintelman et al. [20] and/or wind tunnel simulations as done by Charuvisit, Kimura, and Fujino [18], Cheli et al. [15], Rocchi et al. [28], Forbes et al. [24] and Wieser, Nayeri, and Paschereit [23]. It is a common practice to use the results obtained from wind tunnel simulations as a reference to validate the numerical CFD simulations as made by Salati, Schito, and Cheli [16], Salati et al. [17], Tagliavia Ramírez [2] and Wang et al. [21] being these last less expensive. Regarding then the vehicle dynamics models, different solutions with different complexity have been proposed. In Charuvisit, Kimura, and Fujino [19] a 2 d.o.f. model is proposed to study the effectiveness of wind barriers protecting a truck from crosswind while passing in the wake of a bridge tower; a much more complex model is proposed by Rocchi et al. [28] and Sabbioni et al. [29], in which a Multi Body model is employed to study the same problem.

For what concerns the design of the mentioned fences, several solutions have been proposed. In Kwon et al. [30] and in Kim et al. [31] a methodology to assess the effectiveness of wind barriers through wind tunnel simulations and the use of the commercial software CarSim is presented. In the works of Salati et al. [17], Argentini et al. [32] and Sabbioni et al. [29], a very simple horizontal plates wind barrier is proposed, while in Charuvisit, Kimura, and Fujino [19] a porous barrier is proposed. Çoşkun et al. [33], have studied the benefit of fractal forms for the barriers, finding that these shapes are not only less effective than the one with circular holes, but could produce turbulences that are not desirable when designing a barrier to protect vehicles from crosswind. In Alonso-Estébanez et al. [27], different fences with a focus on the possible configurations of geometry, porosity, distance and height are

proposed to protect vehicles from crosswind when they are stationary. Starting from this last work, Tagliavia Ramírez [2] has developed his solutions that will be taken as a starting point for the design of the fences of this work.

Even if protective barrier could seem something stuck in academic studies, for some years now, some of these solutions have been implemented in viaducts like the Črni Kal viaduct in Slovenia and bridges like the Queensferry Crossing in Scotland, both shown in Figure 5. However, it is clear that not all the possible benefits and the actual effectiveness of these solutions have been deeply enough studied.

**Figure 5:** An overview of the Črni Kal viaduct in Slovenia (left) and a detail of the Queensferry Crossing bridge in Scotland (rigth)

Currently, apart from the vehicle speed reduction, in Italy there are nor general solutions neither norms to be applied when designing roads on exposed sites [4, 34]; infrastructure managers and designers have to conduct a case-by-case assessment. Finding so an effective solution to the problem, could be the first step to write new regulations concerning this issue.

Another topic that deserves attention is linked to the complexity of CFD models. Salati [3] presents two moving mesh strategies: a topological change of the mesh and a rigid motion of the mesh, finding the second as the best solution. The implementation of moving mesh strategies is considered also in other studies; it is the case for example of Wang et al. [21] and Forbes et al. [24]. Being moving mesh strategies very complex and time-consuming from a computational point of view, in many works like Tagliavia Ramírez [2], Alonso-Estébanez et al. [27] and Fintelman et al. [20] a static mesh strategy has been chosen.

## 0.4 Motivation

Summing up the previous points, it is important to state the scope and the novelty of the present work before concluding this chapter. Following the hypothesis that there are many situations in which the danger of crosswind is due to the sudden rise of aerodynamic loads, the goal of this work will be to design and test ad hoc wind-break fences in order to mitigate the effects of a sudden strong crosswind

on two kinds of vehicles: a Truck model and a Car model. These fences should stretch the transient time of rise of the aerodynamic loads so as to reduce the instability of the vehicles due to low transient time. In other words, the hypothesis is that there are many cases in which the danger is due more to the sudden rise of the aerodynamic loads rather than to the steady state value of the wind which can be, instead, managed by a driver. Taking a leaf from the studies of Salati [3] and Tagliavia Ramírez [2], the effectiveness of the designed barriers will be assessed through the coupling of moving mesh CFD simulations and complex vehicle dynamics models applied to a case study (i.e. the exit of a tunnel on a wind exposed site), while taking into account the standards for road design and the feasibility of the proposed solution. Wind tunnel tests, as well as scientific literature, will be used to validate the moving mesh CFD models developed and to draw realistic conclusions from the obtained results.

## Outline

The present work is divided into the following chapters:

**Chapter 1** focuses on the essential background on fluid dynamics in general and aerodynamics needed to understand this work.

**Chapter 2** describes the numerical setup developed for the CFD simulations and the design of the wind-break fences.

**Chapter 3** is dedicated to present the methodology and the results of the wind tunnel experiments conducted to validate the CFD models.

**Chapter 4** presents the vehicle dynamics models developed to study the response of the vehicles and the indices to evaluate their safety conditions.

**Chapter 5** is dedicated to the description of all the results obtained in this work.

**Chapter 6** describes the experiments conducted on the DiM400 dynamic driving simulator.

**Conclusions** summarizes and discuss the results obtained reporting all the possible improvements and suggestions for future researches.

# Chapter 1

# Theory Background

Before of the explanation of the methodology and the tools proposed in this study, it has been deemed useful to dedicate a chapter to present the fundamental equations that govern the fluid dynamics. In the following sections, after a brief explanation of the assumptions followed by CFD software, the governing equations and their discretization will be presented. Particular attention will be paid to the discretization of the Navier-Stokes equations. The mathematical turbulence models RANS, URANS, DES and LES will be presented to better understand the choice made for this study. Several books and articles on these topics could be found in the scientific literature; the following sections could be deepened in *Fluid Mechanics*, *Computational Methods for Fluid Dynamics*, *An Introduction to Computational Fluid Dynamics* [35–37].

## 1.1 Governing Equations

The fundamental assumption followed by CFD software about the governing fluid dynamics equations is to keep mass, energy, and momentum constant in each discretized element of the domain. The air around the vehicles is considered as an incompressible flow and the thermal effects are neglected. From the previous statement, only the equations that ensure that the mass and the momentum are conserved will be required [37].

The mass conservation equation states that the variation of mass inside a fluid volume is equal to the net rate of flow of mass into the element across its faces. Moving the left-hand side of the equals sign all the terms of the mass balance and dividing the entire expression by the element volume $\delta x \delta y \delta z$:

$$\frac{\partial \rho}{\partial t} + \frac{\partial (\rho u)}{\partial x} + \frac{\partial (\rho v)}{\partial y} + \frac{\partial (\rho w)}{\partial z} = 0$$

where $\rho$ is the density of the fluid and $u$, $v$ and $w$ are the velocity component in the $x$, $y$ and $z$ directions. In a more compact vector notation:

$$\frac{\partial \rho}{\partial t} + \nabla (\rho \overrightarrow{u}) = 0 \tag{1.1}$$

Equation 1.1 is the unsteady, three-dimensional mass conservation or continuity equation at a point in a compressible fluid.

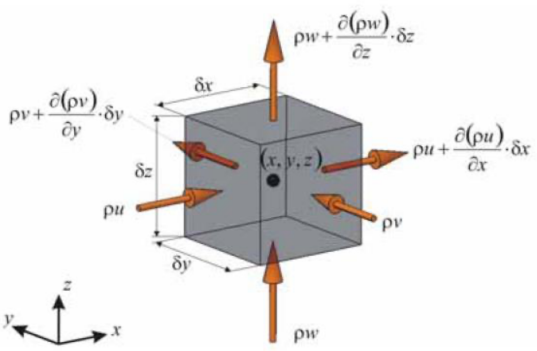


**Figure 1.1:** Scheme of mass conservation [3]

Taking into account the hypothesis of incompressible flow, the density $\rho$ is constant and so Equation 1.1 becomes:

$$\frac{\partial u}{\partial x} + \frac{\partial v}{\partial y} + \frac{\partial w}{\partial z} = 0 \tag{1.2}$$

The momentum equation derives directly from the second Newton law concerning the balance of forces acting on a body; this law is applied to a finite fluid volume, on which we distinguish two kinds of forces:

- surface forces: which act directly on the surface of the fluid element (pressure forces due to the surrounding fluid and viscous forces due to shear and normal stress acting on the surface),
- volume forces: which act directly on the volumetric mass of the fluid element (gravitational, electric, magnetic force).

Newton's second law states that the rate of change of momentum of a fluid particle equals the sum of the forces on the particle [37]. The rates of increase of x-momentum per unit volume of a fluid particle is given by: $\rho\frac{Du}{Dt}$.

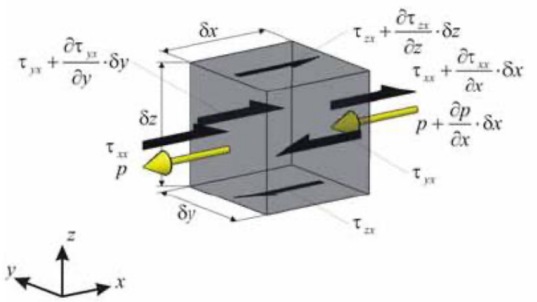


**Figure 1.2:** Scheme of momentum conservation [3]

The total force per unit volume on the fluid due to the surface stresses in the x-direction visible in Figure 1.2 divided by the element volume $\delta x\delta y\delta z$ is equal to:

$$\rho\frac{Du}{Dt} = \frac{\partial(-p+\tau_{xx})}{\partial x} + \frac{\partial(\tau_{yx})}{\partial y} + \frac{\partial(\tau_{zx})}{\partial z} \tag{1.3}$$

Accordingly, for the y and z direction:

$$\rho\frac{Dv}{Dt} = \frac{\partial(\tau_{xy})}{\partial x} + \frac{\partial(-p+\tau_{yy})}{\partial y} + \frac{\partial(\tau_{zy})}{\partial z} \tag{1.4}$$

$$\rho\frac{Dw}{Dt} = \frac{\partial(\tau_{xz})}{\partial x} + \frac{\partial(\tau_{yz})}{\partial y} + \frac{\partial(-p+\tau_{zz})}{\partial z} \tag{1.5}$$

The above equations could not be solved due the impossibility to measure the shear stresses in the fluid. It is necessary so to introduce an approximation, that is considering the fluid as a Newtonian fluid. In a Newtonian fluid, stresses are proportional to the rates of deformation; this relationship can be used to evaluate the normal and shear stresses in the fluid knowing the dynamic viscosity of the fluid $\mu$ that is measured experimentally. In a Newtonian fluid, $\mu$ is considered constant, which means that the relationship between the deformations and the stresses is linear. The time rate of the change of the strain is given by the partial derivatives of the velocity components in the direction of the coordinate axes. The constant that relates stresses to the volumetric deformation is called $\lambda$. Totally, there should be nine equations for the stresses but, since the incompressible fluid is considered isotropic, there are only six independent equations:

$$\tau_{xx} = 2\mu\frac{\partial u}{\partial x} + \lambda\nabla\cdot\overrightarrow{u} \tag{1.6a}$$

$$\tau_{yy} = 2\mu\frac{\partial v}{\partial y} + \lambda\nabla\cdot\overrightarrow{u} \tag{1.6b}$$

$$\tau_{zz} = 2\mu\frac{\partial w}{\partial z} + \lambda\nabla\cdot\overrightarrow{u} \tag{1.6c}$$

$$\tau_{xy} = \tau_{yx} = \mu\left(\frac{\partial u}{\partial y} + \frac{\partial v}{\partial x}\right) \tag{1.6d}$$

$$\tau_{xz} = \tau_{zx} = \mu\left(\frac{\partial u}{\partial z} + \frac{\partial w}{\partial x}\right) \tag{1.6e}$$

$$\tau_{yz} = \tau_{zy} = \mu\left(\frac{\partial v}{\partial z} + \frac{\partial w}{\partial y}\right) \tag{1.6f}$$

Not much is known about $\lambda$, because its effect is small in practice [37]. Anyway due to Equation 1.2, the viscous stresses are just twice the local rate of linear deformation times the dynamic viscosity.

Substituting Equations 1.6 in Equations 1.3, 1.4 and 1.5, applying the definition of material derivative and deleting the small contribution due to the momentum source (even smaller when $\lambda$=0) the following results are obtained:

$$\frac{\partial(\rho u)}{\partial t} + \nabla\cdot(\rho u\overrightarrow{u}) = -\frac{\partial p}{\partial x} + \nabla\cdot(\mu\nabla u) \tag{1.7}$$

$$\frac{\partial(\rho v)}{\partial t} + \nabla\cdot(\rho v\overrightarrow{u}) = -\frac{\partial p}{\partial y} + \nabla\cdot(\mu\nabla v) \tag{1.8}$$

$$\frac{\partial(\rho w)}{\partial t} + \nabla\cdot(\rho w\overrightarrow{u}) = -\frac{\partial p}{\partial z} + \nabla\cdot(\mu\nabla w) \tag{1.9}$$

Equations 1.7, 1.8 and 1.9 are the Navier-Stokes equations, named after the two nineteenth-century scientists who derived them independently. In general these equations are nonlinear partial differential equations, which means that require a boundary condition and an initial condition to be solved.

## 1.2 Discretization of the Navier-Stokes equations

Navier-Stokes equations, have analytical solution only in few simple cases with laminar flow and simple geometries. Apart from these cases, they have to be solved numerically [36]. Numerical solutions exist only in discrete points of the domain, the grid points; all the solutions at other locations could be determined only by interpolating the results at the grid points. Even if in general the distance between two successive grid points in the three coordinates directions is different, CFD solvers compute the solution in the so-called transformed computational space, which contains uniform spacing between successive points. It is worth mentioning that the numerical method could handle both structured and unstructured grids.

Since real fluid flows are generally tridimensional turbulent flows, the governing equations of Section 1.1 must be discretized both in time and space. The discretization introduces an obvious approximation, but there are two more issues related to this numerical problem: the iterative method could diverge and the equations may contain simplifications. For all these reasons, CFD results must be validated and this is generally done with wind tunnel tests.

There is a complex relation between the computational cost and the computational error that within certain boundaries is: the greater the first, the lower the second. Actually this is a crucial task when approaching a new CFD problem: in some cases, simulations could require weeks or months to be completed if the degree of accuracy is too much high or if the computational resources are not enough. Finding the right compromise between computational time and accuracy has been a widely investigated topic during this work as it will be explained in Section 2.3.

A discretization method, is a method to approximate the differential equations by a system of algebraic equations for the variables at some set of discrete locations in space and time [36]. There are many approaches, but since the one chosen for the present work because natively implemented in the OpenFOAM software [38] is the Finite Volume (FV) method, it will be the only one to be presented. For further details on the other approaches such as Finite Difference (FD) and Finite Elements (FE) just to mention a couple of examples, refer to *Computational Methods for Fluid Dynamics*[36]. The FV method uses the integral form of the conservation equations as its starting point. The solution domain is subdivided into a finite number of contiguous control volumes (CVs), and the conservation equations are applied to each CV [36]. The computational node, in which the solutions have to be computed is in the centre of this CV; to express the solutions at the CV surface it is necessary to interpolate. Surface and volume integrals are approximated using suitable quadrature formulae. As a result, one obtains an algebraic equation for each CV, in which a number of neighbour nodal values appear [36]. A fundamental advantage of this method is the possibility of handling any kind of grid and so geometry. Once obtained the system of algebraic equations,

it is necessary a numerical method to provide the solution to the system.

When dealing with turbulent flow, that are flows with a random nature and a complex 3D shape, a closure model is needed to predict the turbulence flow. The direct simulation of the fluctuation could be very expensive due to the small scale and the high frequency involved, so the governing equations could be discretized in time to give a time averaged solution. Moreover, these equations could be manipulated in order to neglect the small-scale fluctuations. This procedure generates discretized equations lowering significantly the computational cost. There are many models available in literature such as: Direct Numerical Simulation (DNS), Large Eddy Simulation (LES), Detached Eddy Simulation (DES) and Reynolds Averaging. None of these could be universally considered superior to the other for all the possible problems: the right choice of the turbulence model is another crucial aspect of CFD simulations. The next section will be dedicated to investigate the different turbulence models.

## 1.3 Turbulence Modelling

### 1.3.1 Introduction to Turbulence

Most of the engineering problems including the one in this study, involve turbulent flows. These last are characterized by the following properties [36]:

- They are highly unsteady. A plot of the velocity as a function of time at most points in the flow would appear random to an observer unfamiliar with these flows (see Figure 1.3),
- they are three-dimensional. The time-averaged velocity may be a function of only two coordinates, but the instantaneous field fluctuates rapidly in all three spatial dimensions,
- they contain a great deal of vorticity,
- turbulence increases the rate at which conserved quantities are stirred (turbulent diffusion),
- turbulence, by means of turbulence diffusion and so mixing, is a dissipative process,
- turbulent flows contain coherent structures-repeatable and essentially deterministic even if there is a random component in the flow,
- turbulent flows fluctuate on a broad range of length and time scales.

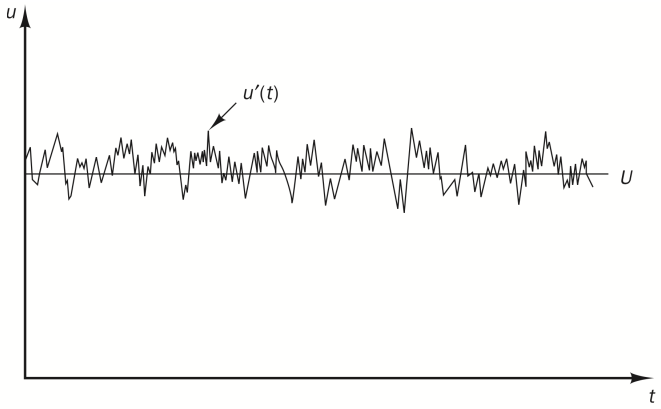


**Figure 1.3:** Typical point velocity measurement in turbulent flow [37]

The visualization of the turbulent flows shows a rotational flow structure, the so-called eddies, that can have a wide range of length scales. The larger eddies are dominated by an inertial effect, while the viscous effect becomes negligible; moreover, they are anisotropic and the flow is strongly influenced by the mean flow. On the other hand, the smaller eddies are isotropic. The smallest scales of motion in a typical engineering problem turbulent flow have lengths of the order of 0.1 to 0,01 mm and frequencies around 10 kHz [37], so time steps of 100 µs would be needed to describe the highest frequency events. This would require a very high computational cost even for a half second simulation of a domain of few $m^3$, making this approach totally impractical if not impossible to follow. Fortunately, most of these engineering problems could be solved with time averaged properties. This approach is the core of the RANS method.

### 1.3.2 Reynolds Averaged Navier-Stokes Equations

In this method, the velocity and pressure terms of Equation 1.7, 1.8 and 1.9 are replaced by a mean term and a fluctuating term each. For instance: $u = \overline{U} + u'$, $v = \overline{V} + v'$, $w = \overline{W} + w'$ and $p = \overline{P} + p'$. Every mean value could be found by integrating the starting value in the $T$ interval: $\overline{U} = \frac{1}{T}\int_0^T u\,dt$, $\overline{V} = \frac{1}{T}\int_0^T v\,dt$, $\overline{W} = \frac{1}{T}\int_0^T w\,dt$ and $\overline{P} = \frac{1}{T}\int_0^T p\,dt$. Substituting the previous results in Equation 1.2, 1.7, 1.8 and 1.9 and remembering the hypothesis of incompressible flow:

$$\frac{\partial \overline{U}}{\partial x} + \frac{\partial \overline{V}}{\partial y} + \frac{\partial \overline{W}}{\partial z} = 0 \tag{1.10}$$

$$\frac{\partial(\rho U)}{\partial t} + \nabla\cdot(\rho U\overrightarrow{U}) = -\frac{\partial P}{\partial x} + \nabla\cdot(\mu\nabla U) + \left[\frac{\partial(-\rho\overline{u'^2})}{\partial x} + \frac{\partial(-\rho\overline{u'v'})}{\partial y} + \frac{\partial(-\rho\overline{u'w'})}{\partial z}\right] \tag{1.11}$$

$$\frac{\partial(\rho V)}{\partial t} + \nabla\cdot(\rho V\overrightarrow{U}) = -\frac{\partial P}{\partial x} + \nabla\cdot(\mu\nabla V) + \left[\frac{\partial(-\rho\overline{u'v'})}{\partial x} + \frac{\partial(-\rho\overline{v'^2})}{\partial y} + \frac{\partial(-\rho\overline{v'w'})}{\partial z}\right] \tag{1.12}$$

$$\frac{\partial(\rho W)}{\partial t} + \nabla\cdot(\rho W\overrightarrow{U}) = -\frac{\partial P}{\partial x} + \nabla\cdot(\mu\nabla W) + \left[\frac{\partial(-\rho\overline{u'w'})}{\partial x} + \frac{\partial(-\rho\overline{v'w'})}{\partial y} + \frac{\partial(-\rho\overline{w'^2})}{\partial z}\right] \tag{1.13}$$

This substitution introduces in the equations other six unknowns, the turbulent stressed known as Reynold Stresses. In order to be able to compute turbulent flows with the RANS equations it is necessary to develop turbulence models to predict the Reynolds stresses and close the system of equations. The most common RANS turbulence models are classified on the basis of the number of additional transport equations that need to be solved along with the RANS flow equations [37]:

- Zero equations: Mixing length model,
- one equation: Spalart–Allmaras model,
- two equations: $k-\varepsilon$ model, $k-\omega$ model and $SST\ k-\omega$ model,
- seven equations: Reynolds stress models.

These models form the basis of standard turbulence calculation procedures in the currently available commercial CFD codes [37]. Of the listed models the mixing length and $k-\varepsilon$ models have been widely used and validated; they are based on the assumption that there exists an analogy between the action of viscous stresses and Reynolds stresses on the mean flow. Boussinesq proposed in 1877 that Reynolds stresses might be proportional to mean rates of deformation; he introduced the turbulent or eddy viscosity $\mu_t$ as unknown to close the system of equations. The viscosity becomes $\mu_{eff} = \mu_t + \mu$. There is also a kinematic turbulent or eddy viscosity given by $\nu_t = \frac{\mu_t}{\rho}$.

### Mixing length models

The idea under this model is to describe the stresses by means of simple algebraic formulae for $\nu_t$ as a function of position. If one velocity scale and one length scale are enough to describe the effects of turbulence:

$$\nu_t = {l_m}^2 \left| \frac{\partial U}{\partial y} \right| \tag{1.14}$$

where $l_m$ is the so-called length scale and $\frac{\partial U}{\partial y}$ is the only significant mean velocity gradient.

### Spalart–Allmaras model

This model was originally proposed to predict the flow field around an airfoil in the transonic region in 1992 [36]. This method has the advantage of using just one equation, and it is also suitable to predict the flow in particular situations such as mixing layer, wakes, boundary layer and in the transition region between laminar and turbulent flow.

### Standard $k-\varepsilon$ model

This is a well known model in the scientific literature and one of the most used in CFD studies due to its robustness and simplicity. Two additional transport equations are added for two additional quantities: $k = \frac{1}{2}(\overline{u'^2} + \overline{v'^2} + \overline{w'^2})$, the

turbulent kinetic energy and $\varepsilon$, the turbulent dissipation. This last term, represent the rate of dissipation of the turbulent kinetic energy. The turbulent viscosity will be computed as:

$$\nu_t = 0.09\frac{k^2}{\varepsilon} \tag{1.15}$$

**Standard $k-\omega$ model**

For this model, proposed by Kolmogorov in 1942, the two additional quantities will be: $k = \frac{1}{2}(\overline{u'^2} + \overline{v'^2} + \overline{w'^2})$, the turbulent kinetic energy and $\omega$, the specific dissipation rate. As in the case of the $k-\varepsilon$ model, also in this case it will be necessary to add two transport equations. The turbulent viscosity will be computed as:

$$\nu_t = \frac{k}{\omega} \tag{1.16}$$

**Shear Stress Transport $k-\omega$ model**

Menter introduced this model in 1992 after noticing that the results of the $k-\varepsilon$ model are much less sensitive to the (arbitrary) assumed values in the free stream, but its near-wall performance is unsatisfactory for boundary layers with adverse pressure gradients. For this reason he suggested a hybrid model transforming of the $k-\varepsilon$ model into a $k-\omega$ model in the near-wall region and the standard $k-\varepsilon$ model in the fully turbulent region far from the wall [37].

### 1.3.3 Large Eddy Simulation

As stated in Section 1.3.1, the larger eddies are anisotropic with a flow strongly influenced by the mean flow while the smaller eddies are isotropic. The LES approach rely on the assumption that the larger eddies need to be computed for each problem with a time-dependent simulation while the general behaviour of the smaller eddies could be computed with a compact model [37]. Instead of the time-averaging, the LES method uses a spatial filtering in order to separate the larger and the smaller eddies by means of a filtering function and a fixed cut-off width. All the eddies greater than the cut-off width will be solved in an unsteady flow computation. There is also a cut-off timescale. The idea is that above those scales the solution will be computed while below just modelled. This filtering, and the interaction effects between the larger, resolved eddies and the smaller unresolved ones, determines the formation of the sub-grid-scale stresses or SGS stresses. An SGS model will be required in order to describe this effect. Similarly to RANS, in LES there is the sub-grid-scale viscosity $\nu_{SGS}$ and so $\nu_{eff} = \nu_{SGS} + \nu$. In most of the LES, $\nu_{SGS} = 0.094\Delta\sqrt{k}$, where $\Delta$ is the cut-off length scale and $k$ has to be found with the Smagorinsky-Lilly model. The filtering function for a general flux variable $\varphi(x,t)$ is:

$$\overline{\varphi(x,t)} = \int_{-\infty}^{+\infty}\int_{-\infty}^{+\infty} \varphi(x',t')G(x-x',t-t')\,dt'\,dx' \tag{1.17}$$

In LES part of the turbulence is depicted in the mesh, in RANS this does not apply. If there is interest in this, LES could be a very powerful tool, otherwise RANS are to be chosen in order to diminish computational cost.

### 1.3.4 Unsteady RANS

To perform an accurate LES, it is necessary a very fine mesh, otherwise it would be impossible to catch the large turbulent structures of the flow, which is the aim of LES. URANS is thought to give accurate predictions in the boundary layer of a coarser mesh. The URANS equation is the RANS equation with the addition of the transient term. The free variables in this case will depend on both time and space. An URANS could give very good results if compared to a RANS, especially in cases in which a transient has to be studied. The computational cost is obviously much higher than the one of RANS. This method has been chosen for most of the simulations of this work; only in very few cases, to study the influence of some parameters or to initialize a flow around a body before running URANS, RANS have been chosen.

### 1.3.5 Detached Eddy Simulation

DES is a hybrid method between URANS and LES: the first model is employed in the boundary layer close to the walls (where turbulence scales are very small) while the second is applied in the other regions; there is a blending function that determines which approach has to be used. DES is very useful especially when with high Reynolds number solve a LES in the near-wall region would be impossible due to the unaffordable computational cost. This doesn't mean that DES require a low computational cost: this last is lower than LES, but greater than URANS. It could be a good compromise between the two in some cases, especially if the blending function is well-defined.

## 1.4 Methodologies for Aerodynamic Studies

As stated in the introduction to this work, there are two main tools developed to investigate air flows around vehicles: wind tunnel experiments and computational fluid dynamics (CFD) simulations. This section is meant to give an overview on this two fundamental tools, aiming to explain why they are complementary and which are the strengths and weaknesses of both. Some may think that both are new tools, but this is a wrong belief for what concerns wind tunnels: the first wind tunnel has been designed in 1871 [9] and since 1934 wind tunnels have been used to test vehicles (as shown in Figure 4). Nevertheless, as it will be better explained in Section 1.4.1, they remain of fundamental importance and validity. CFD simulations are instead a "younger" tool: in the last 30 years they have been developed becoming more and more reliable [37].

### 1.4.1 Wind Tunnel Experiments

According to Schuetz [5], for a long time, the aerodynamic development of automobiles was executed almost exclusively in wind tunnels, initially in those built for aeronautical purposes. At the beginning the test were in almost every case on small scale models (such as 1:10), then with the development of larger wind tunnels, test on bigger models (such as 1:5 or 1:4) were performed. However, it has been clear from the beginning that due to the Reynolds numbers effects, real scale models are always the best choice when possible. In Figure 1.4 a comparison between measurements on two different full scale models of vehicle and their equivalent smaller scale models is visible. However, sometimes small scale models may give accurate results if a good Reynolds number dependency study is done and if there is a big difference between the frontal area of the model and the cross-section of the wind tunnel (in order to avoid the "blockage effect"). In the last twenty years, there has been a focus on the reproduction of the relative motion between vehicle and road and in particular to the rotation of the wheels; these things may be reproduced by means of a moving belt under the vehicle. Moreover, the use of a belt could strongly decrease the effect of the lower wall boundary layer which normally affects the results of wind tunnel simulations. The best way to validate wind tunnel test results is to perform on-road test runs, but these could be not only unaffordable, but also useless in some cases due to the good reliability of the wind tunnel tests nowadays.

One of the main advantages of performing this kind of test is the possibility to perform a flow visualization with smoke, surface oil flow put on the surface of the vehicle, laser sheets or simply with tufts [39]. Visualize the flow may help a lot to understand the aerodynamic of a vehicle, but there are many other advantages of performing wind tunnel test, for example the possibility to have very precise measurements done with pressure probes for what concerns the flow or with accurate 6 d.o.f. balances for what concerns forces. Another key aspect of wind tunnel testing is the possibility to do modifications on the spot to the vehicle during tests to compare different solutions. The possibility of varying the flow velocity is another important aspect that is crucial when the reaching of a target Reynolds number is desired.

However, wind tunnel tests may be unaffordable sometimes, in particular with full scale vehicles. Moreover, perform accurate tests may require a lot of time and the validation of the tests could be very difficult if there are not enough data from other validated tests or on-road tests. It also has to be taken into account that the measurements are conducted only where there have been placed probes and sensor, so the data will be discontinuous. Nowadays the scientific literature is full of papers on wind tunnels and wind tunnel tests being this method robust and very useful not only to perform case studies, but also to validate CFD simulations.

In Section 3.1 all the wind tunnel tests performed during this study will be presented. The result of these tests will be then the basis for the validation of the CFD simulations performed in this study as it will be explained in Section 3.2.

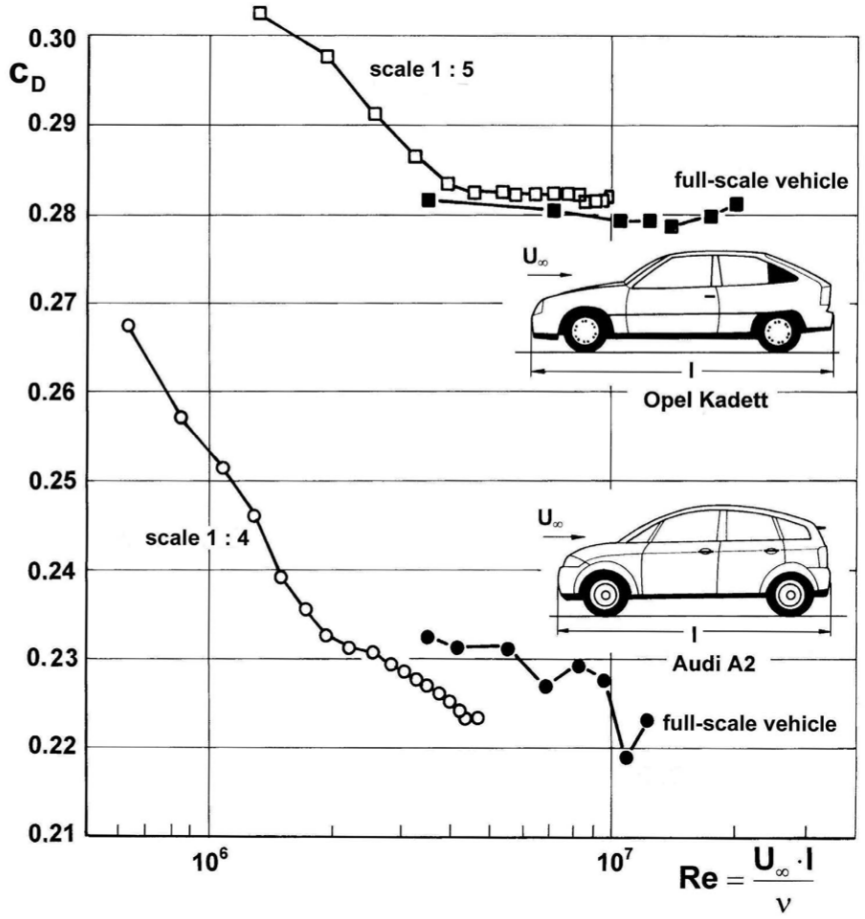


**Figure 1.4:** Effect of Reynolds number on measured drag coefficient with models in scale 1:5, 1:4, and full-scale cars [5]

### 1.4.2 CFD Simulations

From the 1960s onwards the aerospace industry has integrated CFD techniques into the design, research and development and manufacture of aircraft and jet engines [37]. Nowadays CFD simulations are extensively used in the automotive industry in many applications, from the design of the internal combustion engines to the simulation of the air flows in the thermal management conducts to the prediction of the aerodynamic loads on vehicles. It is well known that CFD has become a fundamental tool in the design phase of vehicles. The aim of CFD field is to provide a tool comparable with other CAE (computer-aided engineering) tools such as stress analysis codes [37]. This development of CFD software and the consequent spread has been possible in the last twenty-five years thanks to the availability of relatively affordable high performance computing (HPC) hardware. This tool has given the chance to reduce significantly the cost of the design and test phase and has also given the opportunity to increase the range of the possible researches. Nowadays it is possible to perform CFD simulations with accurate results that in most cases are perfectly affordable and for this reason this tool is becoming more and more widespread.

One of the main advantages of this method is that once computed it is very easy

to visualize the flow. Moreover, in most of the cases useful for automotive industry, it is possible to obtain a very good estimation of variables such as pressure or velocity that are crucial for aerodynamic studies. Another key aspect is that the variables (even if averaged as explained in Section 1.2) are available in all the computational domain. In general CFD simulations have a lower cost if compared to wind tunnel tests or on-road measurements. However, to obtain reliable results it is fundamental to validate the model and so to compare the results with wind tunnel tests or data available in the scientific literature. The main disadvantage is probably that in order to perform accurate simulations, a very high computational cost could be required. Nowadays there are many possibilities to perform simulations on online clusters and this may help to overcome the problem of the supplying of computational resources. Another drawback is probably the not so user-friendly interface that most of the CFD software currently have (in particular the open source ones) and the difficulty to find training material sometimes also for what concern the availability of specific university courses, resulting frequently in the necessity of self-training activities. Nevertheless, the potential of this kind of simulations is becoming more and more clear both in the automotive industry and in the academic world and for this reason the scientific literature on this field is growing very fast.

In Section 2.2 the numerical setup for the CFD simulations performed during this study will be presented. The result of these simulations will be then validated in Section 3.2 with the help of the wind tunnel test explained in Section 3.1.

# Chapter 2

# Numerical Setup

## 2.1 Geometries

In this section, an overview of the geometries used in this work is presented. For what concerns the vehicles, it has been chosen to use models already validated in other works in order to have the possibility to validate the CFD models not only with self-made wind tunnel measurements, but also with data available in scientific literature.

### 2.1.1 Truck

For the design of the truck, the same model presented in Sterling et al. [40] has been used: a simplified reproduction of the DAF LF commercial truck; this is also the same model chosen by Tagliavia Ramírez [2] and so in the scientific literature there already were two works (the first with wind tunnel measurements and the second with static mesh simulations) to compare with the present work during the validation phase. Obviously w.r.t. a real truck there are some simplifications (such as the avoiding of windows, air intakes and lights), that don't affect much the results while studying crosswind, but may help to reduce computational time. However, all the relevant details for this study have been kept as much as possible similar to the originals. In Figure 2.1 it is possible to see an overview of the truck model used, while in Table 2.1 the maximum dimensions of the model are reported.

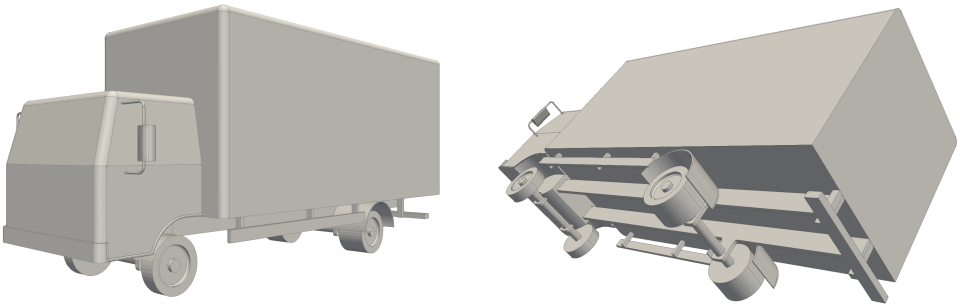

**Figure 2.1:** An overview of the truck model used in CFD and wind tunnel simulations

| parameter | unit | value |
|---|---|---|
| $l_{max}$ | m | 7.83 |
| $w_{max}$ | m | 2.80 |
| $h_{max}$ | m | 3.52 |

**Table 2.1:** Maximum dimensions of the Truck model

### 2.1.2 DrivAer

The choice of the car model has been the "DrivAer", which is a 1:4 scale open-source design-hybrid of an "Audi A4" and a "BMW 3 Series" developed in the TU-Munich. The cooperation of Audi and BMW in introducing this model is mainly aimed to make researchers switch from general analysis, such as the ones that can be developed using the Ahmed Body [8], to more industrial-oriented tests. As stated on the TU-Munich DrivAer webpage [41], to allow for a large variety of investigations, the DrivAer body was developed as a modular concept with 18 different mock up configurations with different geometries of the top, of the underbody, of the mirrors, of the wheels and eventually also of the cooler configuration. The design chosen for this study is the notchback model with smooth underbody, mirrors and smooth wheels. In Figure 2.2 it is possible to see an overview of the specific model used, while in Table 2.2 the maximum dimensions of the model are reported.

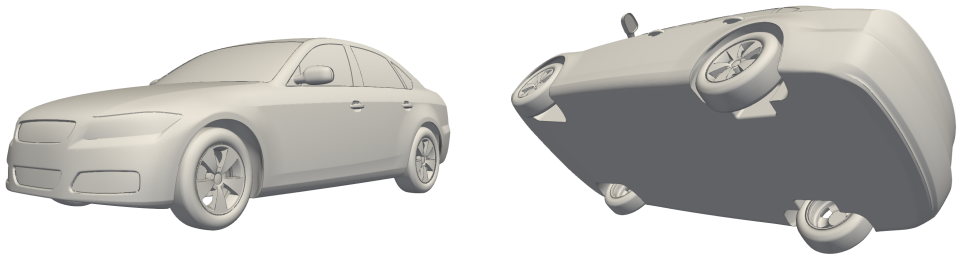

**Figure 2.2:** An overview of the DrivAer model used in CFD and wind tunnel simulations

| parameter | unit | value |
|---|---|---|
| $l_{max}$ | m | 4.61 |
| $w_{max}$ | m | 2.03 |
| $h_{max}$ | m | 1.41 |

**Table 2.2:** Maximum dimensions of the DrivAer model

### 2.1.3 Fences

Wind-break fences design has been a crucial topic for the development of this work. Being the first work whom aim has been to stretch the transient time of rise of the aerodynamic loads, it would have been impossible to test already existing fences for this purpose. However, a modification of the fences designed by Tagliavia

Ramírez [2] (visible in Figure 2.3) and based on the work of Alonso-Estébanez et al. [27] has been made.

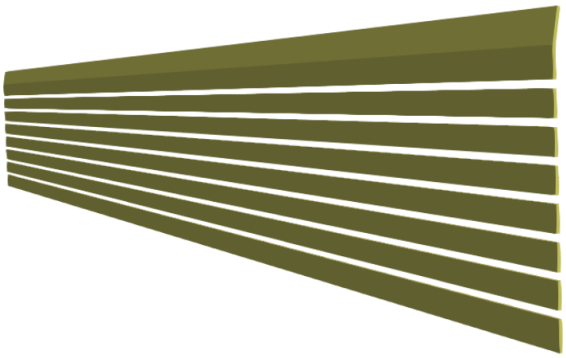

**Figure 2.3:** Wind-break fences with rectangular openings, a porosity of 20%, a height of 4 m, a and a deflector of 80° which is 0,5 m high (Tagliavia Ramírez [2])

It has been kept the fundamental design of Tagliavia Ramírez [2] fences with rectangular openings, a 20% porosity, a deflector of 80° 0,5 m high at the upper part and an initial height of 4 m adapting this design to the aim of this work by reducing the height of the barriers every 12,5 m and adding a vertical element to join all the different modules of 12,5 m as visible in Figure 2.5, making this design more realistic and industrially feasible. Two kinds of fences have been tested:

- Model 1 ("fences 1", see Figure 2.5): medium size length fences made of four 12,5 m modules, the first of which 4,5 m high (including the deflector) and the last 1,5 m high (each module is 1 m lower than the previous)

- Model 2 ("fences 2", see Figure 2.6): large size length fences made of six 12,5 m modules. The first four modules are equal to the ones of fences 1, the penultimate is 1 m high and the last is 0,5 m high and has no deflector.

The choice of the length of the modules has been made in order to optimize the overall geometry for the common speed for heavy-weight vehicles of 25 m/s (90 km/h); for example, the fences 2 should stretch the transient of the rise time of aerodynamic loads from 0 to 3 s.

**Figure 2.4:** An overview of the two designed wind-break fences tested in this work: on the upper part the fences 1, on the lower part the fences 2

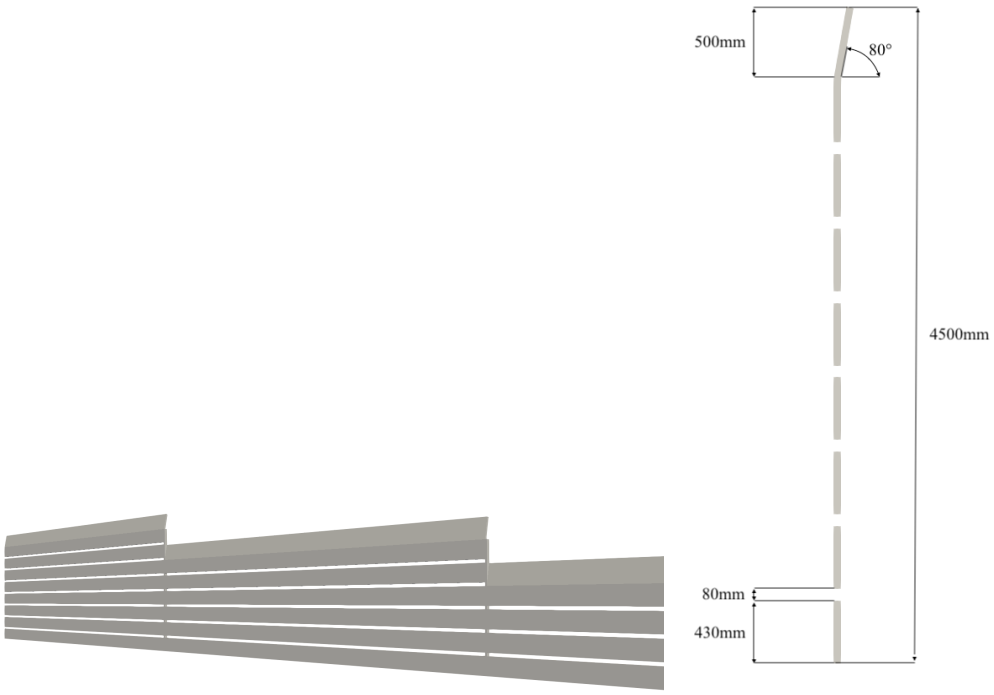


**Figure 2.5:** A detail and a section view of the wind-break fences 1

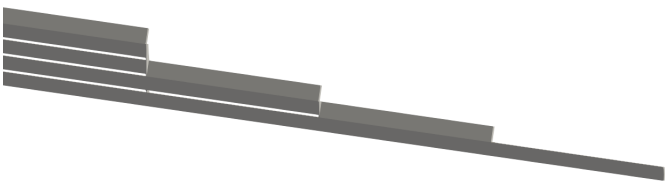

**Figure 2.6:** A detail of the final part of the wind-break fences 2

## 2.2 Numerical Setup

Several simulations have been run during this study: in this section an overview of the numerical setup of both moving and static mesh simulations is presented. The simulations have been run thanks to two clusters, without whom it would have been impossible to run such computationally expensive simulations: the "CFDHub" cluster of Politecnico di Milano [42] and the "GALILEO" cluster of CINECA under the ISCRA initiative [43].

### 2.2.1 Moving Mesh Cases

Being the aim of this work the study of the transient time of rise of lateral aerodynamic forces in situations in which a sudden strong wind reaches the vehicle (e.g. when a vehicle leaves a tunnel on an exposed site), moving mesh simulations are the more realistic way (and so probably the best way) to study such situations. There are two possibilities to run a moving mesh simulation:

1. Topological mesh change;
2. Rigid motion of the mesh.

In both situations it is necessary to define two blocks: a moving block (that will move thanks to a topological change or by a rigid movement) and a static block.

In the first case, the cells of the mesh are stretched and squeezed to allow the mesh movement and when a certain aspect ratio is achieved in these elements, in order to allow for large displacements, new elements are added behind the moving mesh (to plug the hole created in the domain) while in front of this mesh some elements are deleted. The whole process would run continuously to a fixed speed. As well explained and tested by Salati [3] this technique is not often used in external aerodynamics (especially for parallelization limits) and for this reason has not been tested in the present work.

The second case is much easier to understand: the cells are rigidly moved at a constant speed without changing shape or volume during their movement. In this way the quality of the mesh does not change during the simulation, saving computational time. Unfortunately, this strategy needs a particular attention to the patches around the moving part of the domain, that are solved with the Arbitrary Coupled Mesh Interface (*ACMI*) on which not much scientific literature has been produced yet.

Before digging deeper in the *ACMI* tool and in the numerical details of the simulations, it could be useful to have a look to the computational domain defined for the simulations, the reference system and the boundary conditions. As it is possible to understand from Figure 2.7, the computational domain has been defined as follows: there is a static outer domain (in black in Figure 2.7) and a moving inner domain (in red in Figure 2.7) which contains the vehicle. The dimensions of the domain have been chosen in order to avoid the blockage effect of the vehicles. For the purpose of this study, in all the moving mesh simulations, the vehicle has a speed in the direction of the positive $x$ axis while the wind has a speed in the direction of the positive $y$ axis (reference system visible in Figure 2.7). For what

concerns the boundary conditions as it could be understood from Figure 2.7, apart from the *ACMI* conditons with which the static-dynamic interfaces are treated, there are three faces considered as an *inlet* (the ones reached by the arrows) and one as an *outlet*. The ground is treated as a *wall* and the vehicle is treated as a *wall* too with a *movingWallVelocity* condition defined according to the sliding speed of the moving domain; in the static mesh simulations used to initialize the flow that will be explained in a later paragraph, this last condition becomes a *fixedValue* condition. Zero pressure has been set up at the *outlet* and *slip* wall is used for the *top* boundary. Obviously, on the vehicle wall functions have also been defined.

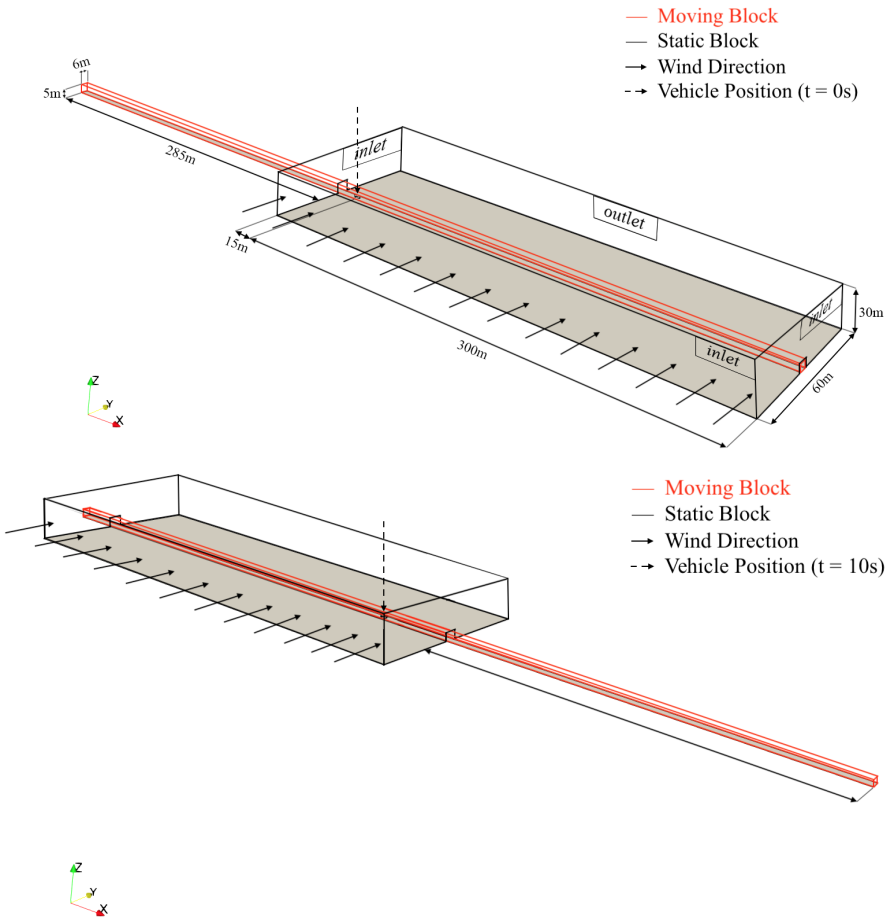


**Figure 2.7:** An overview of the computational domain used for the validation of the numerical model at the beginning (top) and at the end of the simulation (bottom)

To understand how the *ACMI* works, it is fundamental to know how the Arbitrary Mesh Interface (*AMI*) tool works. This tool works weighting the quantities of each cell at one side of the interface with the corresponding cells on the other side and in particular it does a weighting based on the shared portion of face between the cells on the two parts.

Referring to Figure 2.8 the *AMI* allows so the stationary part of the mesh (called $P$ in Figure 2.8) to exchange information with the dynamic one (called $E$

in Figure 2.8) according to the frontal overlap area that the two cells share [3].

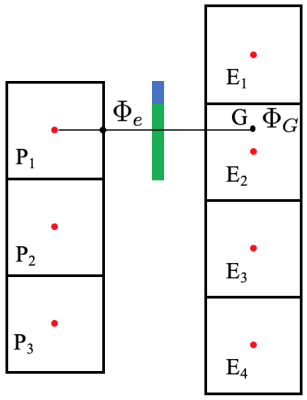


**Figure 2.8:** Scheme of the *AMI*

In formulae:

$$\Phi_e = \Phi_G + (1-\alpha)\Phi_P,\ \alpha = \frac{x_e - x_P}{x_G - x_P},$$

$$\Phi_G = \sum_i \alpha_i \Phi_{E_i},\ \alpha_i = \frac{A_i}{A}$$

As an example, the cell $P_1$ in Figure 2.8 exchanges information with cell $E_2$ according to the frontal overlap area represented in green.

The *ACMI* works as an *AMI* in the region where there overlap between the moving domain and the static domain (in green in Figure 2.9) while in the non-overlap region it is possible to introduce any other boundary condition (in blue in Figure 2.9).

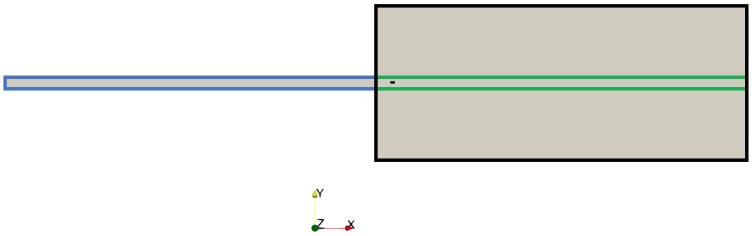

**Figure 2.9:** Scheme of the *ACMI* to the domain of this work

The moving block and so the vehicle, slide as defined in the *dynamicMeshDict* contained in the *constant* folder. Regarding the validation cases, the defined speed for the vehicles has been 25 m/s, while a speed of 4,41 m/s has been imposed to the wind in order to reach a yaw angle of 10° as explained in Section 3.2.

The reference system for the computation of the forces is a moving reference system placed on the ground and in the centre of the front axle of both the vehicles with positive $x$ axis in the direction of motion and positive $z$ axis from the bottom to the top of the vehicle.

The aerodynamic coefficients, fundamental for the validation of the models have been computed according to the relations:

$$C_x = \frac{2F_x}{\rho U^2 A_{ref}} \tag{2.1a}$$

$$C_y = \frac{2F_y}{\rho U^2 A_{ref}} \tag{2.1b}$$

$$C_z = \frac{2F_z}{\rho U^2 A_{ref}} \tag{2.1c}$$

$$C_{Mx} = \frac{2M_x}{\rho U^2 A_{ref} l} \tag{2.1d}$$

$$C_{My} = \frac{2M_y}{\rho U^2 A_{ref} l} \tag{2.1e}$$

$$C_{Mz} = \frac{2M_z}{\rho U^2 A_{ref} l} \tag{2.1f}$$

where $F$ are the aerodynamic forces, $M$ the aerodynamic moments, $\rho$ is the air density, $U_\infty$ is the relative wind speed, $A_{ref}$ is the reference surface and $l$ the length of the vehicle. Please notice that due to the fact that the direction of motion of vehicle and of the wind are always perpendicular, the relative wind speed could be computed as:

$$U = \sqrt{v^2 + U_\infty^2} \tag{2.2}$$

where $v$ is the speed of the vehicle and $U_\infty$ is the speed of the flow far from the vehicle. As a consequence, the relative yaw angle will be:

$$\alpha = \arctan \frac{U_\infty}{v} \tag{2.3}$$

For what concerns the mesh around the vehicles, apart from the refinement on the surface of the vehicles, two refinement boxes have been defined one inside the other, in order to correctly compute the flow; the greatest of the two has been defined in order to match perfectly the static-dynamic interface. On this interface, on the static part in fact, it has been defined a refinement box that goes from the very beginning to the end of the static block with a height equal to the one of the moving block. This makes the interface the best possible for this application. For a better comprehension refer to Figure 2.10. Moreover, for both the vehicles five layers have been defined in order to achieve a desirable $y+$ to correctly predict the flow near the surfaces [37].

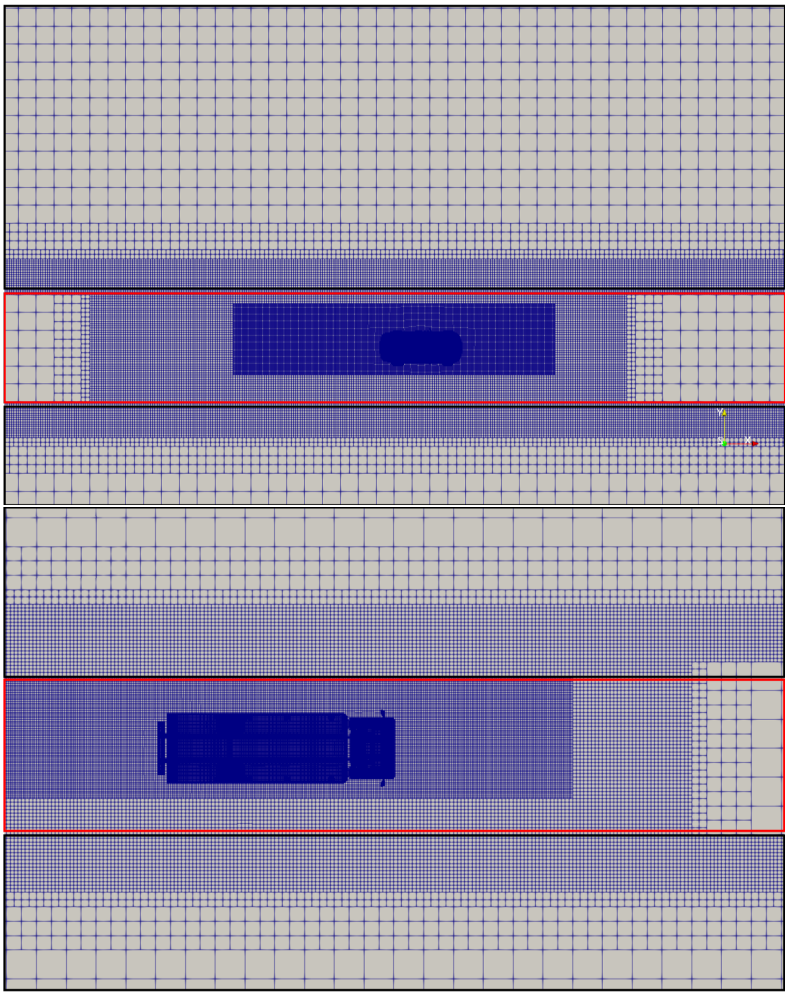

**Figure 2.10:** Overview of the refinement boxes around the vehicles (DrivAer seen from the top in the top figure, Truck from the top in the bottom figure) and of the interface between the static (in black) and dynamic domain (in red)

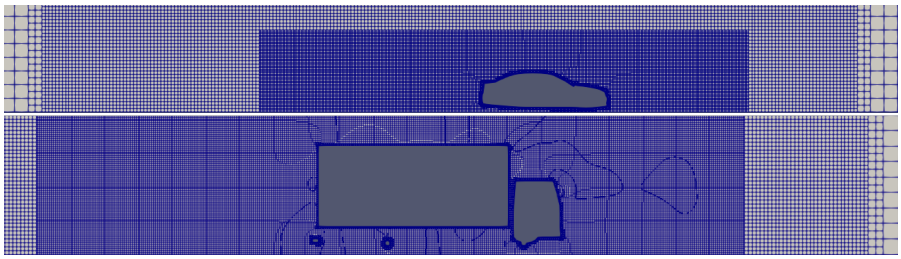

**Figure 2.11:** Overview of the refinement boxes and the layers around the two vehicles

Time variant incompressible URANS equations have been solved with the *pimpleFOAM* standard solver with the *dynamicMesh* option and for the two equations of the $k-\omega$ model (see Section 1.3) the SST turbulence model have been used. So PIMPLE which is a combination of PISO (Pressure Implicit with Splitting of Operator) and SIMPLE (Semi-Implicit Method for Pressure-Linked Equations) algorithms has been used [37] and a second order upwind discretization scheme has been applied.

In order to speed up the simulations and save computational time, the simulations have been initialized with the potential solver *potentialFOAM* and the mesh renumbered in order to be represented by a diagonal matrix with the *renumberMesh* option. Moreover, all the simulations have been initialized with *simpleFOAM* standard solver simulations in order once again to save computational time. All the dynamic simulations have been run with a time step low enough to keep the Courant number as near as possible to 1. The order of magnitude of the time step has been $10^{-4}s$, leading to a very high computational cost even with hundreds of processors as it will better explained in Section 2.3.

### 2.2.2 The Case Study

In order to test the effectiveness of the two kinds of wind-break fences in a realistic scenario, it has been decided to test the exit of a vehicle from a tunnel on an exposed site. In Figure 2.12 an overview of both the base case (the one without wind-break fences) and of one of the cases with the fences is reported; apart from the presence of the wind-break fences in the static domain, the two case studies are perfectly identical.

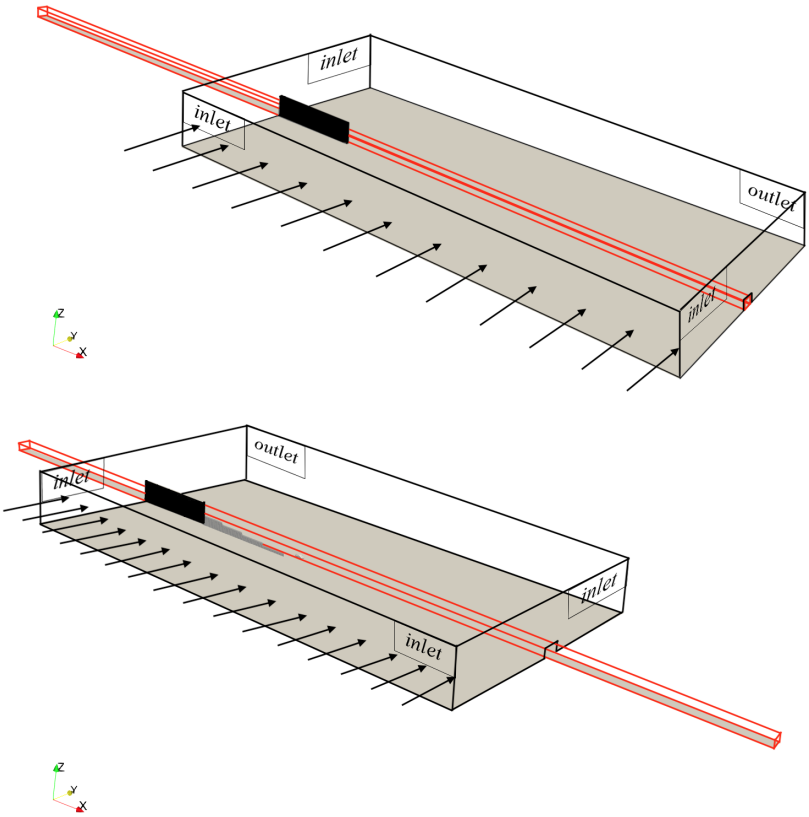


**Figure 2.12:** Overview of the two kind of simulated case studies: the base case without the wind-break fences (top) and one of the two cases with the fences (bottom)

The dimension of the lanes as well as the position of the fences has been set according to the Italian road regulations [34]. The fences have been placed just over the guard-rail, that is placed at the end of the emergency lane. According to the Italian road regulations, a normal highway lane is 3,5 m wide (as visible in Figure 2.13), while the emergency lane is 3 m wide [34]; for this reason, the fences have been placed 3,5 m away from the end of the first lane in order to be just over the guard-rail (as visible in Figure 2.13).

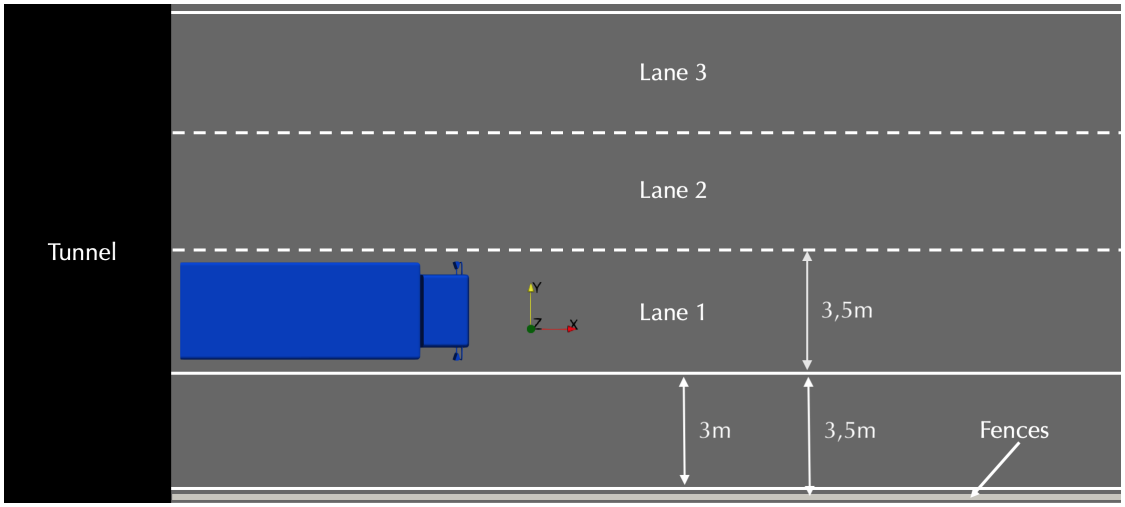


**Figure 2.13:** Top overview of the simulated case studies

First of all, it has been necessary to decide which part of the domain should move and which should not; for the purpose of this study since what matters is the relative motion between vehicle and fences, there would be no difference if instead of moving the vehicle, would be the barrier to be in motion. However, this last approach has turned out to be a bit more expensive than the first.

Another key point has been related to the initialization of the flow around the vehicles: it has been assessed after some trials that with the previously described setup, that after the time invariant simulation used as a zero condition for the simulation, about other 4 s were necessary for the flow to be fully stable around the vehicle; for this reason it has been decided to run 5 s of simulation before each case study simulation in order to have a fully initialized flow. The main drawback of this approach is that a longer domain is needed and so many other mesh elements have to be added, increasing so the computational effort.

It is worth mentioning that thanks to the properties of the *ACMI* interface, another tested possibility has been to initialize the flow by means of the *blockage* condition when the moving domain is still out the static box, but this has turned out to be a bad initialization due to the small height and width of the moving block.

Before concluding this section two more things have to be stated: the first is related to the tunnel, that has been reproduced with a wall (much higher than the two vehicles). This approximation has been necessary in order to save mesh elements and so reduce the computational effort, but due to the horizontal nature of the tested wind condition, this approximation has been deemed acceptable. The

second is related to the mesh of the wind-break fences: a particular attention has been kept on this mesh, that has to be perfectly refined in order to give reliable results. In Figure 2.14, it is possible to see an overview of the mesh around the fences and two particulars of the same mesh. It is important to state that between the horizontal plates, 11 mesh elements have been placed (by means of the layers control), as visible between the two black horizontal lines on the lower left part of Figure 2.14.

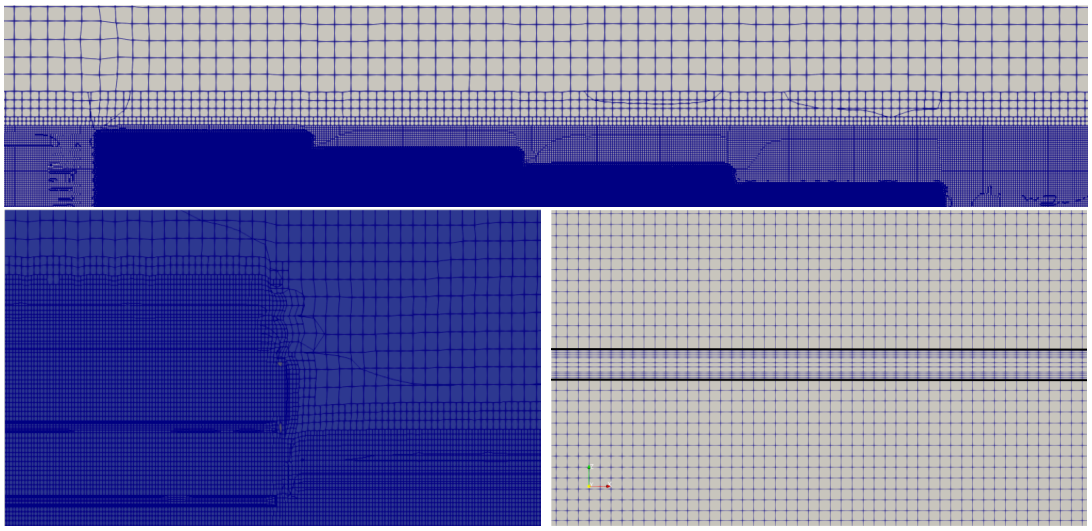

**Figure 2.14:** An overview of the mesh around the wind-break fences (top) and two details of the same mesh (bottom)

### 2.2.3 Static Mesh Cases

As it will better explained in Chapters 4 and 5, one of the main limits of the moving mesh simulations of this study is that the vehicles during the simulations move straight. Apart from the longitudinal motion, the position of the vehicle in terms of yaw angle does not change during the CFD simulations. For this reason, it has been deemed important to state if this means an underestimation or an overestimation of the aerodynamic loads during the simulations studying the influence of yaw angles on the aerodynamic coefficients. This study has been made with a more "classical" CFD approach (i.e. with a static mesh simulation) w.r.t. the other studies of this work.

In Figure 2.15, it is possible to see an overview of the computational domain for these cases. The vehicle is placed inside the domain in a fixed point, so in this case the wind speed and direction will be the one of the relative wind of an equivalent case in which both vehicle and wind are moving. Even in this case, the dimensions of the domain have been chosen in order to avoid the blockage effect of the vehicles. To have consistent results comparable with the ones of the moving mesh cases, the vehicle is placed in the direction of the $x$ axis while the wind has two components: one in the direction of the positive $y$ axis and the other in the direction of the negative $x$ axis. For what concerns the boundary conditions as it could be understood from Figure 2.15, there are two faces considered as an *inlet* (the ones reached by the arrows) and two as an *outlet*. The ground is treated as a

*wall* and the vehicle is treated as a *wall* too with a *fixedValue* condition defined according to the $x$ axis component of the wind. Zero pressure has been set up at the *outlet* and *slip* wall is used for the *top* boundary. Obviously, on the vehicle wall functions have also been defined.

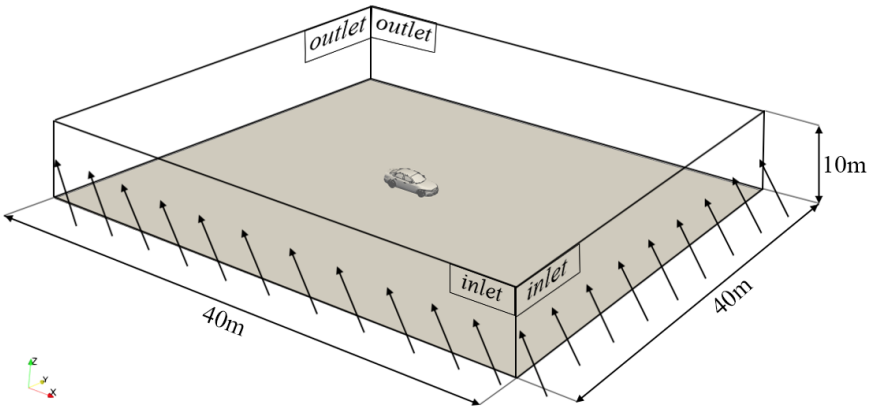


**Figure 2.15:** Overview of the static mesh cases domain

Regarding the validation cases, the defined relative wind speed has been 40 m/s as explained in Section 3.2.

The reference system for the computation of the forces is a fixed reference system placed on the ground and in the centre of the front axle of both the vehicles with positive $x$ axis in the direction of theoretical vehicle motion (so opposite to the wind $x$ component) and positive $z$ axis from the bottom to the top of the vehicle.

The aerodynamic coefficients, also in this case fundamental for the validation of the models have been computed according to the relations:

$$C_x = \frac{2F_x}{\rho U^2 A_{ref}} \tag{2.4a}$$

$$C_y = \frac{2F_y}{\rho U^2 A_{ref}} \tag{2.4b}$$

$$C_z = \frac{2F_z}{\rho U^2 A_{ref}} \tag{2.4c}$$

$$C_{Mx} = \frac{2M_x}{\rho U^2 A_{ref} l} \tag{2.4d}$$

$$C_{My} = \frac{2M_y}{\rho U^2 A_{ref} l} \tag{2.4e}$$

$$C_{Mz} = \frac{2M_z}{\rho U^2 A_{ref} l} \tag{2.4f}$$

where $F$ are the aerodynamic forces, $M$ the aerodynamic moments, $\rho$ is the air density, $U_\infty$ is the relative wind speed, $A_{ref}$ is the reference surface and $l$ the length of the vehicle.

In this case, the relative yaw angle will be:

$$\alpha = \arctan \frac{U_y}{U_x} \tag{2.5}$$

For what concerns the mesh around the vehicles, apart from the refinement on the surface of the vehicles, which as it will be explained in Section 3.2 in this case has been very accurate (due to the low computational cost of these simulations), five refinement boxes have been defined one inside the other, in order to correctly compute the flow and catch well the wake behind the vehicles. Moreover, for both the vehicles five layers have been defined in order to achieve a desirable $y+$ to correctly predict the flow near the surfaces [37]. In Figure 2.16 it is possible to visualize an overview of the mesh for the two vehicles while in Figure 2.17 it is possible to have a look on the layers around the two vehicles.

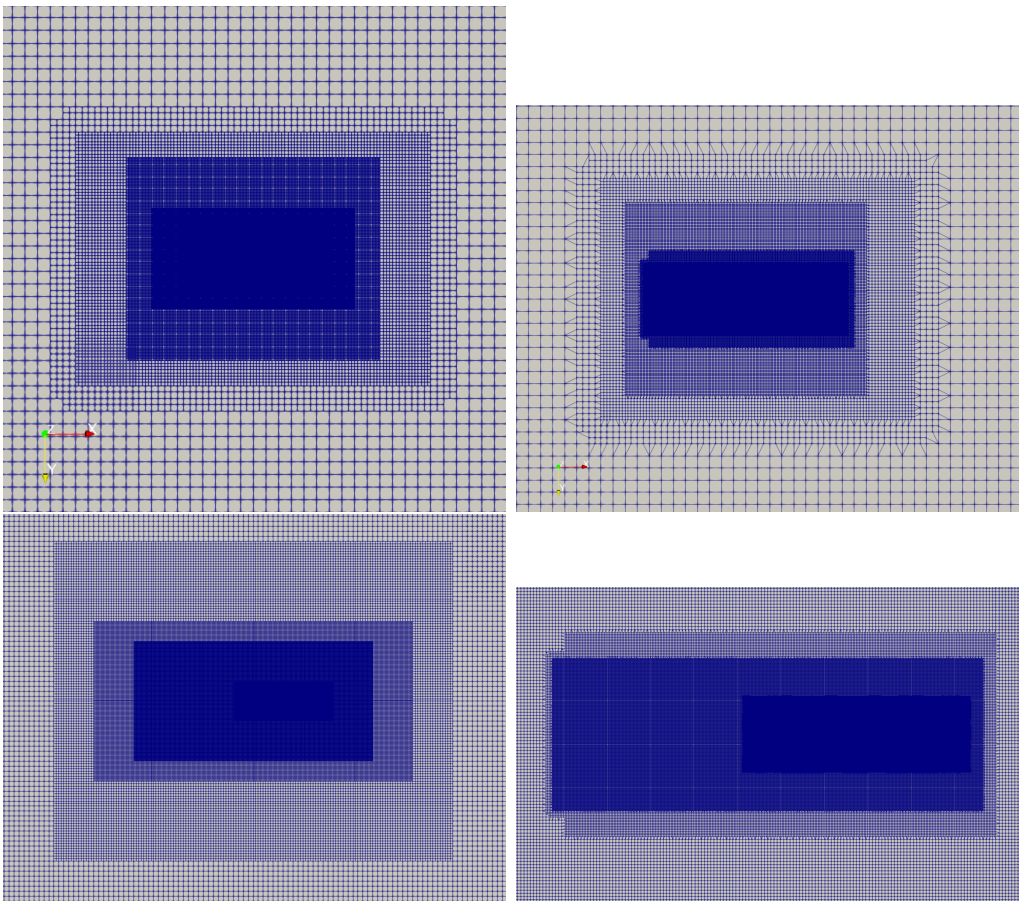

**Figure 2.16:** Overview of the mesh for the two vehicles (DrivAer on the left and Truck on the right) seen from beneath (top) and overview of the refinement boxes (bottom)

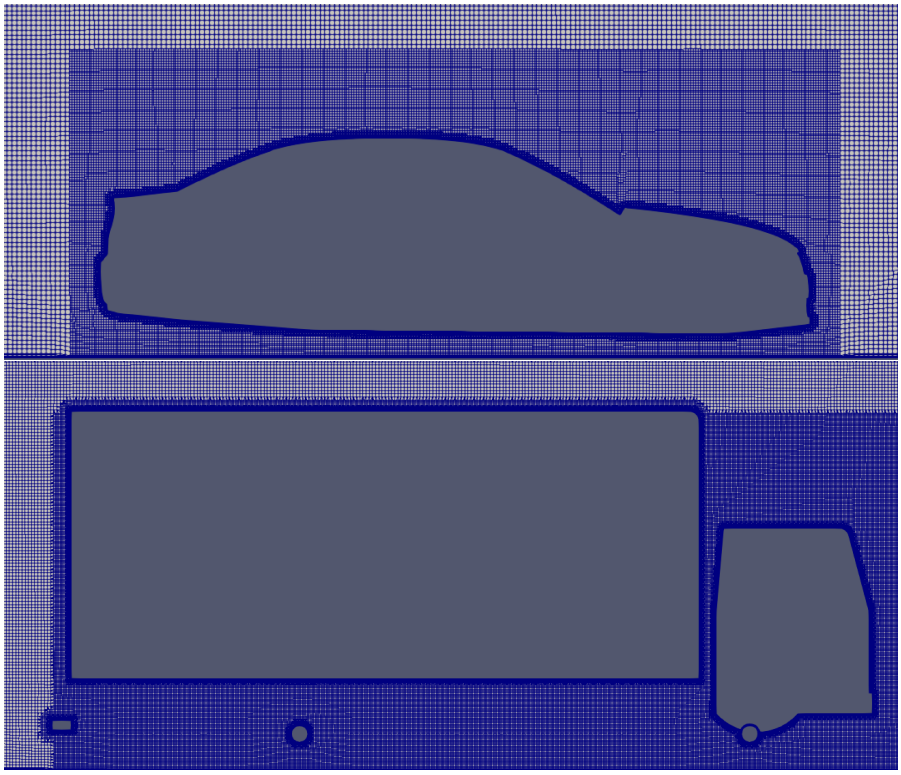

**Figure 2.17:** Overview of the layers of the two vehicles: Drivaer (top) and Truck (bottom)

Time invariant incompressible RANS equations have been solved with the *simpleFOAM* standard solver and for the two equations of the $k-\omega$ model (see Section 1.3) the SST turbulence model have been used. So SIMPLE (Semi-Implicit Method for Pressure-Linked Equations) algorithm has been used [37] and a second order upwind discretization scheme has been applied.

In order to speed up the simulations and save computational time, the simulations have been initialized with the potential solver *potentialFOAM* and the mesh renumbered in order to be represented by a diagonal matrix with the *renumberMesh* option. All the static mesh simulations have been run for 2500 steps even if in almost every case, after 800 time steps the convergence would have been reached.

## 2.3 Scalability Analysis

As stated at the beginning of Section 2.2, the simulations of this study have been run thanks to two clusters, without whom it would have been impossible to run such computationally expensive simulations: the "CFDHub" cluster of Politecnico di Milano [42] and the "GALILEO" cluster of CINECA under the ISCRA initiative [43]. Saving computational time and resources has been one of the most challenging tasks during this study. From one side there have been the necessity to run simulations in a reasonable time (in the order of some days) to have the right time to extract the results and make new analysis and modifications; from the other side, the necessity to save the limited computational resources available. The combination of the two, resulted in most of the cases in the need

of a good trade-off between the hundreds of high performances cores necessary to save computational time and the optimal usage of these lasts. However, as it will be explained in Section 2.3.1, the task has been studied from many points of view, considering also how to reduce the computational weight of the simulations.

One may think that increasing ad libitum cores means a continuous decrease of computational time. Unfortunately, this is not true once overcame a threshold that is different for any case and mesh typology. So a good practice for this kind of studies, is to make a scalability analysis to assess the optimal number of cores in order to save computational time and resources. This is exactly what has been done each time a simulation with a different mesh has been run in this study. In Figure 2.18, an example of scalability analysis for a moving mesh case of $2{\cdot}10^7$ elements is reported; in particular, the data are reported in terms of speedup. On the $x$ axis there is the number of cores, while on the $y$ axis is reported the ratio between the computational time at the minimum number of cores tested and the same time varying the number of cores. As it is clear, the real curve is very far from the ideal one, in which $t$ is halved each time the number of cores is doubled. However, since the purpose of this study is to find an optimal trade off between the computational time and the used resources, it could be helpful also have a look to the second graph reported in Figure 2.18, which reports the actual computational time on the $y$ axis in hours. The first consideration that could be done looking at both the graphs is that over 720 cores, the computational time starts to rise once again, making the parallelization useless. The second important consideration has to be done on the order of magnitude of the computational time: looking at the speedup analysis one may state that 120 cores would be the best option in terms of efficiency, but from the scalability plot it is also clear that in this case the simulation would need almost 6 days, which is a significant amount of time. From this point of view the best choice would be to set the number of cores to 720, but this would mean a highly inefficient use of the computational resources and being these last limited, this would result in a big waste of resources. So the choice of 504 cores has seemed fair enough in order to save computational time (2 days is much more acceptable than 6) and resources, being the 240 cores option once again too much time-consuming (in the order of 3.5 days) and considering the 648 and 720 cores options not worth in terms of time gain.

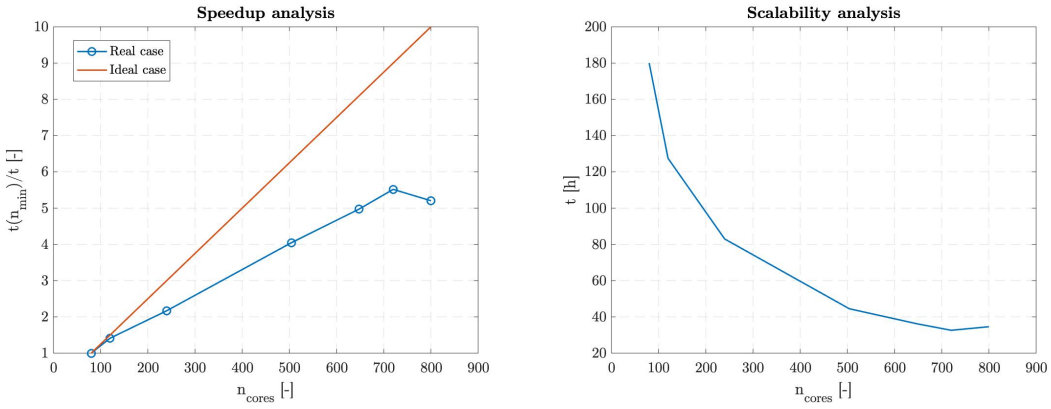


**Figure 2.18:** Speedup and scalability analysis for a moving mesh case of $2{\cdot}10^7$ elements

### 2.3.1 Logical Scheme and Computational Time Optimization

As stated at the beginning of this section, the computational effort has been a crucial topic during this study. Many strategies have been tested in order to reduce as much as possible the amount of computational resources needed to run the simulations in a reasonable time (in the order of some days).

In Section 2.2.2 it has been explained which part of the mesh should be kept in motion and how to initialize the flow around the vehicle; so now it is possible to understand the logical scheme behind each case study simulation. In order to study the effectiveness of the designed wind-break fences, it has been decided to simulate the exit of the two kind of vehicles from a tunnel on an exposed site. To understand so the impact of the presence and of the kind of fences, it has been deemed useful to compare the results with the case without fences (the base case). So if all the other parameters concerning the CFD simulation are fixed (and in particular the direction and speed of the wind and of the vehicle), three different simulations have to be run: the vehicle exiting the tunnel without any wind-break fences and the same manoeuvre with the two kind of fences. These three simulations have a common initial part: in all the three cases, the vehicle has to run 5 s in the tunnel to have the flow fully initialized before the final manoeuvre. Moreover, the three simulations have another common part: the moving mesh (the inner domain) is the same; what changes from one case to another is in fact the static domain: in all the three cases there is the presence of the tunnel, but depending on the case at the end of the tunnel there could be a kind of fences or another (or no fences in the base case).

Now that the general idea should be clear, it is possible to understand the block diagram reported in Figure 2.19, that represents the logical scheme that has been applied for each setup to compute the base case simulation and one of the two cases with the wind-break fences (the third follows the same scheme of the second). The two domains are meshed separately (in order to be re-usable for all the cases having a backup copy in their folders), then they are merged in another folder to simulate the base case (upper branch of the block diagram). Then thanks to two dictionaries (*topoSet* and *createBaffles*) the mesh becomes ready to move (the first dictionary is used to set the moving box, the second to make possible the information exchange between the moving and the fixed domain); the domain on the upper left screenshot of Figure 2.19 is obtained. However, before running the moving mesh simulation, a static mesh simulation with the steady state solver *simpleFoam* is run to initialize the flow in the domain and the result of this simulation is used as initial condition (by means of the *mapFields* dictionary) for the moving mesh simulation (see the central upper screenshot of Figure 2.19). At this point, the first moving mesh simulation is run: 5 s behind the tunnel in order to fully initialize the flow around the vehicle (with the transient solver *pimpleFoam*); the result is visible in the upper right screenshot of Figure 2.19. This is the starting point for both the base case and the other two cases since the vehicle is still behind the tunnel, with a fully initialized flow. Going on with the base case (and so the upper branch), at this point the tunnel exit simulation could be run, but before this, it has been thought to cut the useless part of the domain (so all the static part of the domain behind

the vehicle and all the moving part of the domain already out of the static domain). This is visible in the bottom left and central screenshots of Figure 2.19 and is done with the combination on two dictionaries: *topoSet* and *subsetMesh*. At this point, a much more computationally affordable simulation is run for 3 s (one of which necessary to leave the tunnel) in order to collect all the data to be then post-processed.

For what concerns the other two cases (the ones with the fences), moving so to the lower branch of Figure 2.19 the starting point is the same as before, but in order to get to this point, it is necessary to compute once again the static domain (with the fences added to the tunnel) and merge it with the same moving mesh than before, shifted to the position reached by the moving mesh after 5 s. By doing this and applying the *mapFields* dictionary with the *inconsistent* option (due to the presence of the fences), the new case is initialized and ready to be run. Once again, before doing this thanks to the combination of the *topoSet* and *subsetMesh* dictionaries, a smaller domain is obtained. At this point, depending on the kind of fences to be tested, the simulation could be run for 5 or 6 s in order to collect the data when the vehicle is behind the fences and for 2 s after the end of the fences (in order to compare the results 2 s after the end of the tunnel for the base case and after the fences for the other two cases).

This complex logical scheme is the result of an accurate study on the strategies to reduce the computational time and amount of resources needed that has turned out to be very efficient. By doing this in fact it has been possible to "recycle" many times the same meshes for different setup of wind speed and vehicle speed and running only the necessary steps for each simulation. This led to the saving of a considerable amount of computational resources that have been used to run more setups.

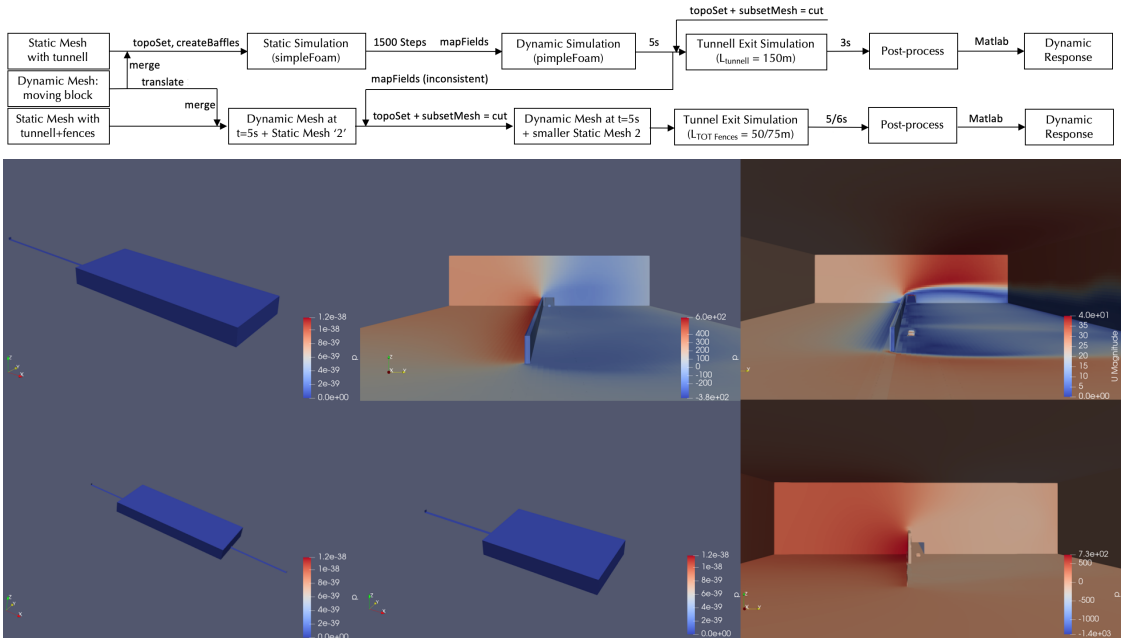


**Figure 2.19:** Logical scheme of the steps followed to simulate the cases and to optimize the computational time (top) and some screenshots of these steps (bottom)

# Chapter 3

# Wind Tunnel Experiments and CFD Models Validation

## 3.1 Wind Tunnel Tests

As already mentioned in the introduction to this study, the present thesis work has been developed at Politecnico di Milano in the frame of the Alliance4Tech programme thanks to which a portion of the experimental part has been conducted in a previous experience at TU-Berlin. In particular, the experimental part previously developed, has been a wind tunnel campaign for a project of the "Automobil- und Bauwerksumströmung" course. For this reason, the Section 3.1.2 is reported here by courtesy of Prof. Christian Navid Nayeri and of the other students involved in this study: Andrea Marinoni, Carmelo Millitarì, Enrico Stella and Leonardo Tartabini [44].

For what concerns the wind tunnel experiments conducted at Politecnico di Milano, a special thanks goes to the supervisor of this work Prof. Paolo Schito for the great opportunity, to Eng. Fabio Semeraro and to the M.Sc. student Andrea Dellavedova for their help in the setup of the experiments and data collection.

### 3.1.1 Truck

In this section, the experiments conducted in the wind tunnel for educational purposes of the Politecnico di Milano presented in Yılmazer [45] on a 1:22 scale Truck model are described. The aim of these experiments has been to compare the aerodynamic coefficients of the model at different yaw angles. The choice for the design of the truck has been the same model presented in Sterling et al. [40]: a simplified reproduction of the DAF LF commercial truck. The frontal area of the model is equal to 0,016 $m^2$, this area has been used as a reference for the drag coefficient calculation, while the lateral surface area, equal to 0,043 $m^2$ has been used as a reference for the others aerodynamic coefficients in order to be consistent with the results obtained by Cheli et al. [13]. The reference system for this study is so that the $x$ axis points from the rear to the front axle of the vehicle and the $z$ axis from the ground to the top of the wind tunnel.

Being the first time that the wind tunnel has been used for these purposes, before working directly on the model, a characterization of the wind tunnel has

been necessary as well as some modifications. After that, an aligning phase of the model, meant to find the real zero yaw angle has been performed, followed by an investigation of the Reynold's Number $Re$ dependency of the drag coefficient. A measure of all the aerodynamic forces and moments acting on the model as a function of the yaw angle for $U_\infty = 16\,\mathrm{m/s}$ has been then conducted. For each step, flow visualization pictures have been collected.

### Wind Tunnel Characterization and Experimental Setup

The experiments took place in the wind tunnel for educational purposes of the Politecnico di Milano presented in Yılmazer [45], which is a small open-circuit subsonic portable wind tunnel for educational purposes whose dimensions are 1 m in length and 0.5 x 0,5 $\mathrm{m}^2$ in the cross-section with a fixed ground. In Figure 3.1 an overview of the structure of the wind tunnel is reported. The cross-section has a fixed ground, which means that no moving belt is installed underneath the model to avoid the presence of the ground boundary layer. The wind tunnel w.r.t. its original configuration has been modified with the addition of a turning table for yaw angle adjustments or side force analysis.

The wind tunnel is equipped with a single-stage axial fan, whose power is 1,1 kW. The wind velocity is set by controlling the fan power, measured in $kW$, via the inverter, and can reach a maximum value of 20 m/s, thanks to the 2:1 ratio of contraction in the test section.

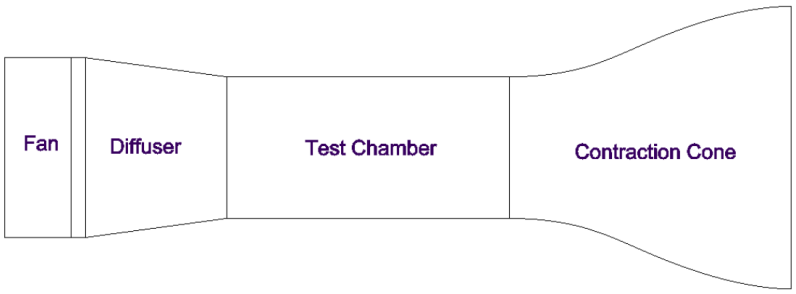


**Figure 3.1:** General Layout of the Open-Circuit Wind Tunnel for educational purposes of Politecnico di Milano [45]

The wind tunnel is equipped with a six-component scale that allows the measure of forces and moments in three directions (see the render in Figure 3.2).


**Figure 3.2:** Render of the scale present in the wind tunnel

A Pitot-static probe of Prandtl type, which is a combination of the Pitot tube and static pressure tapping used for simultaneous measurement of stagnation and static pressures, is installed on the top of the testing area. To obtain flow velocity the following relation is applied:

$$P_{tot} = P_{st} + P_{dyn} = P_{st} + \frac{1}{2}\rho U^2 \tag{3.1}$$

A thermocouple has been used for the thermal measurements, in order to calculate the density of air in the room and inside the tunnel, whose value is needed for the evaluation of the flow velocity and the Reynolds number.

For a faster usage of the wind tunnel, in order to have a reference to follow when setting up the simulations, a characteristic curve of the tunnel has been derived. This curve, visible in Figure 3.3, turned out to be very practical to have an estimation of the Reynolds number achievable for predetermined values of $\Delta P$ before setting up the simulations.

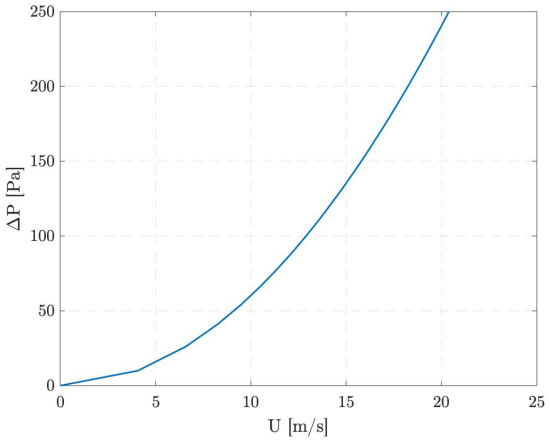


**Figure 3.3:** characteristic curve of the wind tunnel

From the very beginning of this wind tunnel campaign it has been clear the rotational nature of the air inside the wind tunnel due to the rotation of the fan. For this reason, it has been deemed worth the implementation of a honeycomb to be placed before the contraction cone that even if designed in the original project, has never been implemented. The purpose of a honeycomb in general is to increase the flow quality and reduce the turbulence level at the entrance of the tunnel; it aligns the flow with the axis of the tunnel, breaks up larger-scale flow unsteadiness and removes the swirl from the incoming flow minimizing the lateral variations in both mean and fluctuating velocity [46]. In order to better visualize the changes in the flow before and after the honeycomb implementation, four elements like the one in Figure 3.4 equipped with long tufts have been installed in the test section.

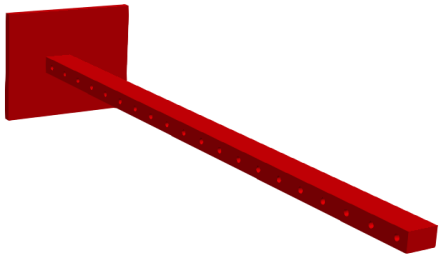

**Figure 3.4:** Render of one the elements used for the study of the flow

In Figure 3.5 a comparison between the flow structure with and without the implementation of the honeycomb is reported. As expected, the implementation of the honeycomb took to a reduction of the rotational effects. This has been confirmed by the side force calibration studies for the Truck model reported in Figure 3.6: before the implementation of the honeycomb the actual 0° Yaw (influenced also by minor non-symmetries of the model) was of 4,8° while after this value moved to 2,7°.

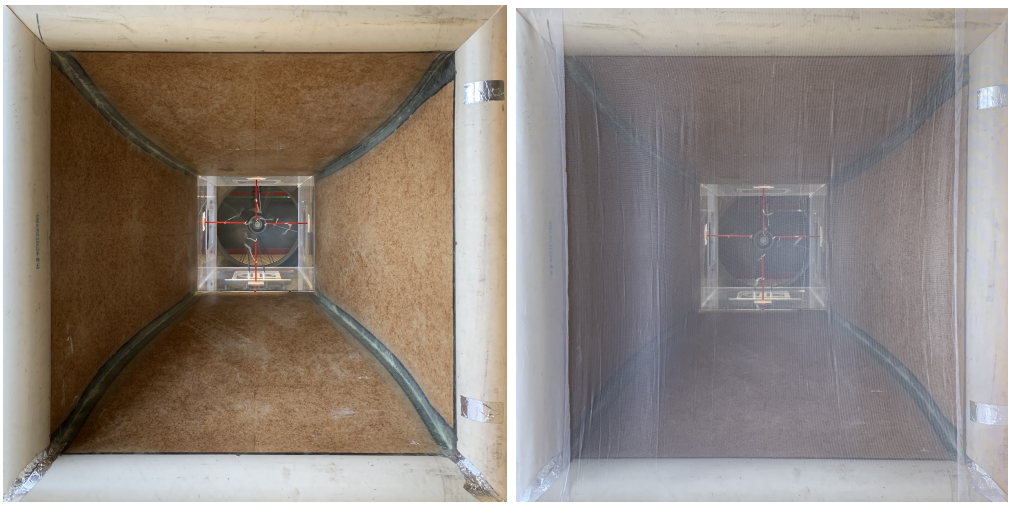

**Figure 3.5:** Flow visualization without (left) and with the honeycomb (right)

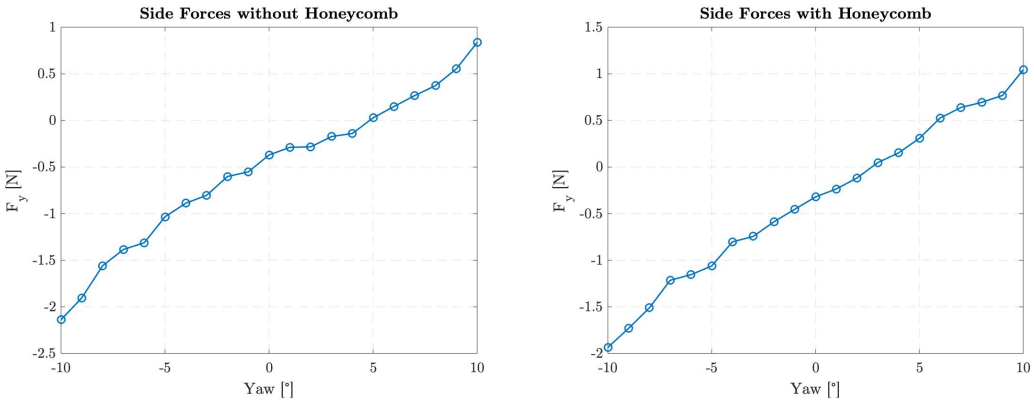


**Figure 3.6:** Side force analysis without (left) and with the honeycomb (right)

For what concerns the Truck studies, in order to get a flow visualization, many tufts have been applied to the model.

### Experiments

At first, in order to obtain consistent results, a side force calibration has been necessary; this has been needed to calibrate the yaw angle in order to have zero side force with zero yaw angle. The results have been reported in the previous section in comparison with the case without the honeycomb, but for the sake of completeness they are also reported in Figure 3.7. The zero side force condition is reached at yaw angle equal 2,7°. The newly found calibrated angle has been therefore set as the reference yaw angle for the following experiments.

Once calibrated the side forces, in order to ensure that the experiments would have been performed in a condition of independence w.r.t. Reynolds number, it has been necessary to test the model in different condition of flow speed, to check the variability of drag coefficient. By acting on the rotational speed of the fan, the values plotted in Figure 3.7 have been found. As clear from this plot, after a certain value of *Re* the fluctuation decreases considerably, suggesting that a Reynolds number independent condition has been reached. It is very interesting to observe the shape of this plot, suggesting that the values after 1.5 x $10^5$ are in super-critical regime, being this value a threshold from the drag crisis zone to the Reynolds independent zone. It is interesting to notice that the results of this Reynolds dependency study matches very well what reported in 'The wind tunnel testing of heavy trucks to reduce fuel consumptions'[47]. In order to perform the following analysis properly, the wind speed has been therefore set to 16 m/s.

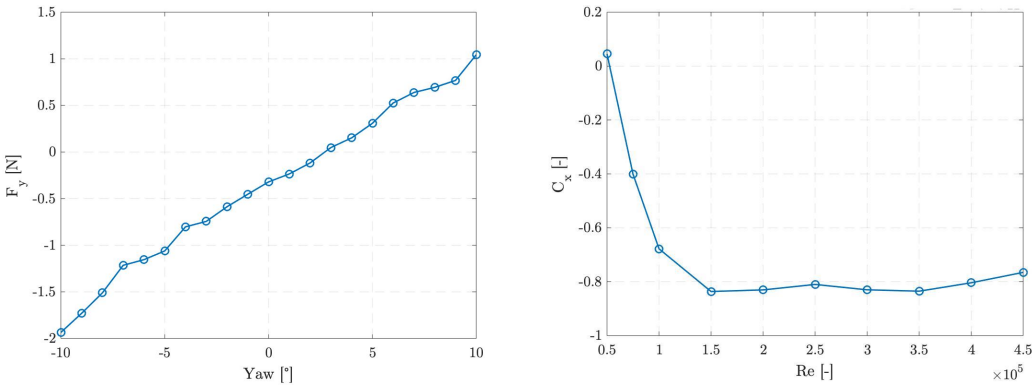


**Figure 3.7:** Zero side force analysis (left) and Reynolds number independency

The results presented in this section have been collected for a speed of the wind of 16 m/s and for a yaw angle variation between 0° and 40°. The first thing that can be seen from Figure 3.8 is the behaviour of the side forces: as expected $C_y$ is 0 in 0° this means that the calibration of the model has been performed correctly. This force is almost linear with the yaw angle and this is reasonable due to the fact that increasing the module of the yaw angle, more side area is hit by the wind, increasing so the module of the force (and so the coefficient). Regarding the drag and lift coefficients the trend of the curves, are as expected [13].

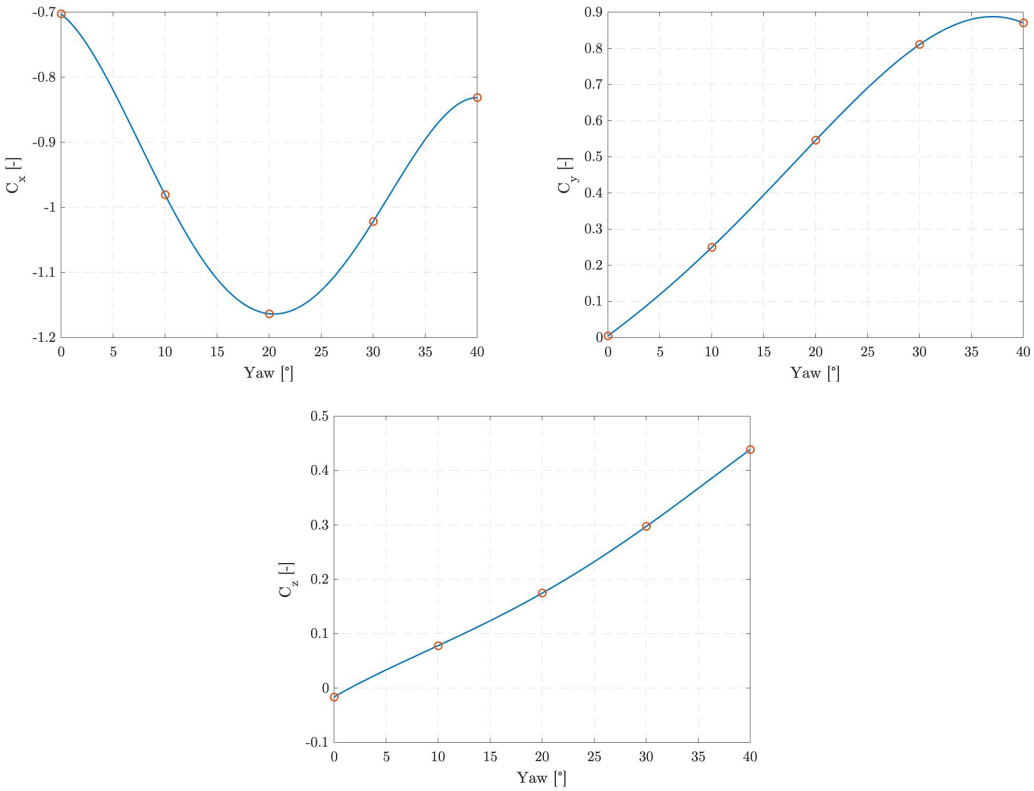


**Figure 3.8:** Aerodynamic coefficients for a yaw angle variation between 0° and 40°: $C_x$ (top left), $C_y$ (top right) and $C_z$ (bottom)

However, even if these results are very consistent with what reported in 'Wind tunnel tests on heavy road vehicles: Cross wind induced loads—Part 1'[13] for what concerns the trend, there is a mismatch due to the blockage effect of small cross-section in the test area of the wind tunnel used w.r.t. the surface of the vehicle [46]. In Figure 3.9 it is possible to compare the results obtained with the ones reported in 'Wind tunnel tests on heavy road vehicles: Cross wind induced loads—Part 1'.

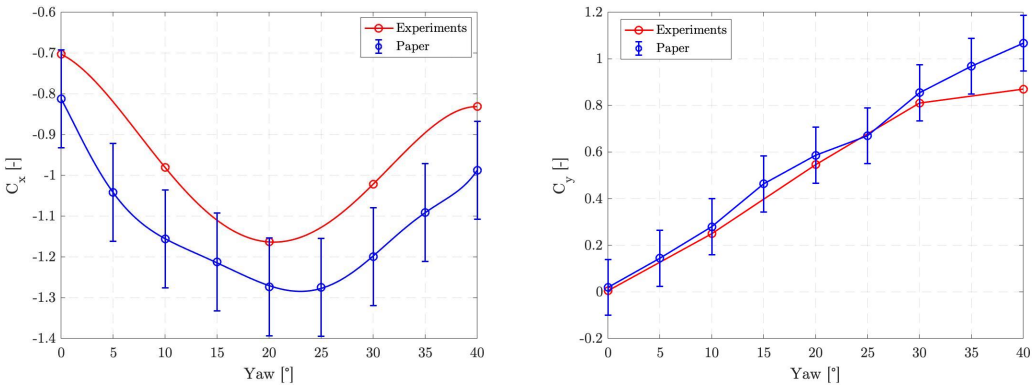


**Figure 3.9:** Comparison between aerodynamic coefficients of this study and the ones obtained by Cheli et al. [13]

### Flow Visualization

The presence of the tufts makes possible some considerations about the behaviour of the flow around the truck. In the left part of Figure 3.10 it is possible to visualize the flow on the front of the truck for a yaw of 0°. It is interesting to notice that between the cab and the trailer there is a high pressure zone and the formation of vortices that are the reason why in most of the modern trucks there is a profile that smooths the passage of the air from the cab to the trailer. In the right part of Figure 3.10 it is possible to visualize the wake of the truck; in particular it is interesting to look the tufts in the middle of the rear that shows the presence of vortices in the dead water and the consequent suction. It is worth mentioning the very good match between these simulations and the CFD simulations reported in Section 5.2, in Figure 3.11 the streamlines visualizations from the same angles of Figure 3.10 is reported.

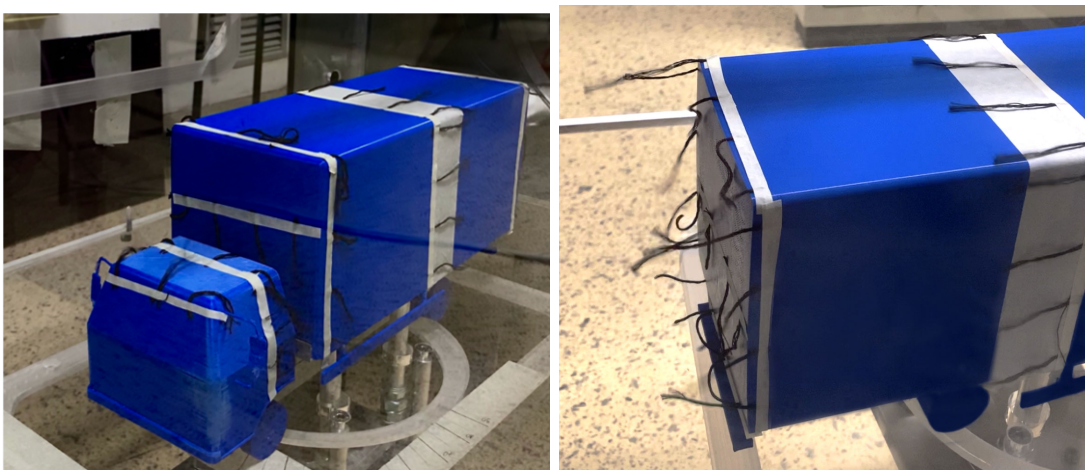

**Figure 3.10:** Flow visualization at a yaw angle of 0°

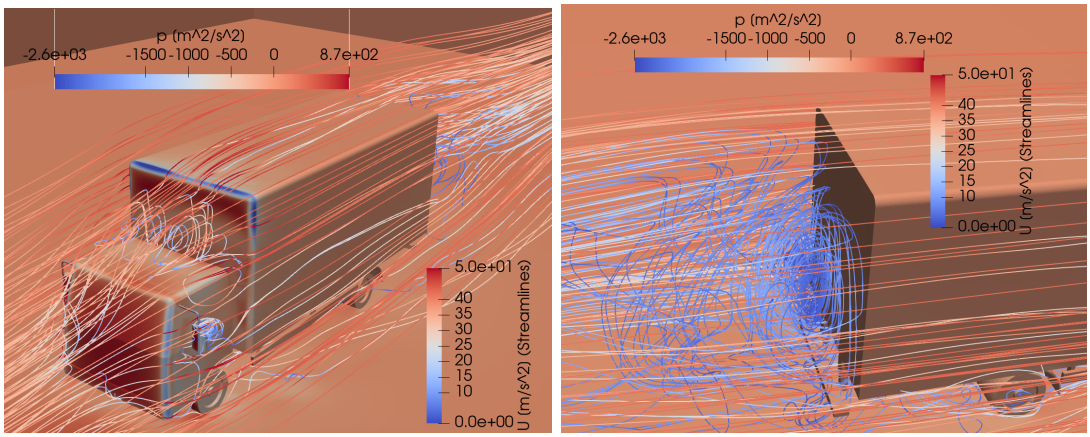


**Figure 3.11:** Streamlines visualization at a yaw angle of 0° from the CFD simulations of Section 5.2

### 3.1.2 DrivAer

In this section, the experiments conducted in the GroWiKa wind tunnel [48] of the TU-Berlin on a 1:4 scale "DrivAer" model are described. The aim of these experiments has been to compare the aerodynamic coefficients of the model at different yaw angles. The choice of the car model has been the "DrivAer", which is a 1:4 scale open-source design-hybrid of an "Audi A4" and a "BMW 3 Series" developed in the TU-Munich. The cooperation of Audi and BMW in introducing this model is mainly aimed to make researchers switch from general analysis, such as the ones that can be developed using the Ahmed Body [8], to more industrial-oriented tests. As stated on the TU-Munich DrivAer webpage [41], to allow for a large variety of investigations, the DrivAer body was developed as a modular concept with 18 different mock up configurations with different geometries of the top, of the underbody, of the mirrors, of the wheels and eventually also of the cooler configuration. The design chosen for this study is the notchback model with smooth underbody, mirrors and detailed wheels.

After the aligning phase of the model, meant to find the real zero yaw angle, a Reynold's Number $Re$ dependency of the drag coefficient has been investigated. A measure of all the aerodynamic forces and moments acting on the model as a function of the yaw angle for $U_\infty = 40\,\mathrm{m/s}$ has been then conducted. For each step, flow visualization pictures have been collected.

#### Experimental Setup

The object of the analysis has been the "DrivAer" model whom detailed dimensions are visible in Figure 3.12. The reference system for this study is reported in Figure 3.12 too. The frontal area of the model is equal to $0{,}135\,\mathrm{m}^2$, this area has been used as a reference for all the aerodynamic coefficients calculations.

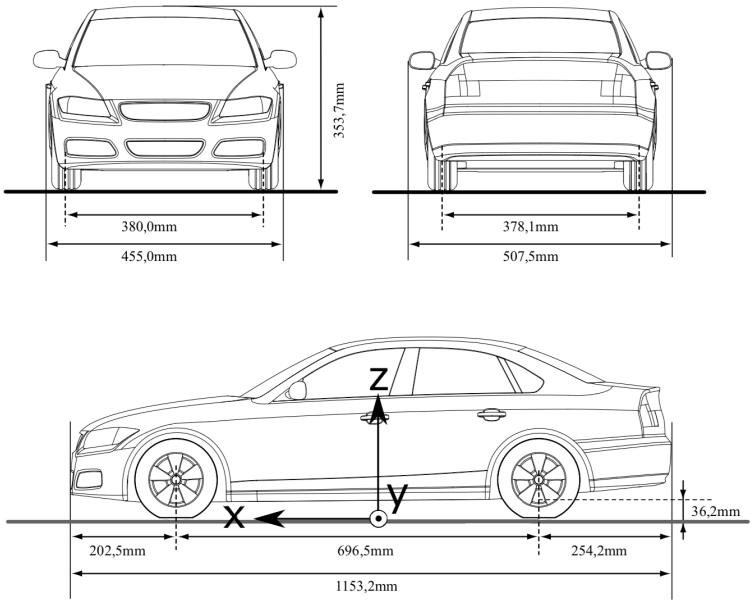


**Figure 3.12:** Technical drawing of the DrivAer model [41]

The experiments took place in the GroWiKa wind tunnel [48], which is a closed-circuit wind tunnel, and in particular in its first compartment of the four present, whose dimensions are 2,5 m in length and 2 x $\sqrt{2}$m$^2$ in the cross-section with a fixed ground. In Figure 3.13 a technical drawing of the wind tunnel is reported. The cross-section has a fixed ground, which means that no moving belt is installed underneath the model to avoid the presence of the ground boundary layer. Such layout is possible because of the presence of an open gap 133 mm high in the front section of the wind tunnel testing area (visible in Figure 3.14) where there is the tunnel contraction, so that the majority of the boundary layer goes inside this cavity and does not affect the flow on the model, being ejected at the rear of the testing area. Another effect taken into account is the influence of rotating wheels on the flow in reality; since the DrivAer model is equipped with steady wheels, this inaccuracy is attenuated by having the model suspended, with the tyres contact patch 6 mm above the ground level. Moreover, the model is installed on a turning table for yaw angle adjustments or side force analysis.

The wind tunnel is equipped with a single-stage axial fan with adjustable blades, whose power is 450 kW. The wind velocity is set by controlling the fan rotational speed, measured in *rpm*, via the user interface, and can reach a maximum value of 70 m/s, thanks to the 6.25:1 ratio of contraction in the test section. Thanks to the introduction of steel nets in proximity of the contraction of the tunnel, the turbulence intensity is kept below 0.5%.

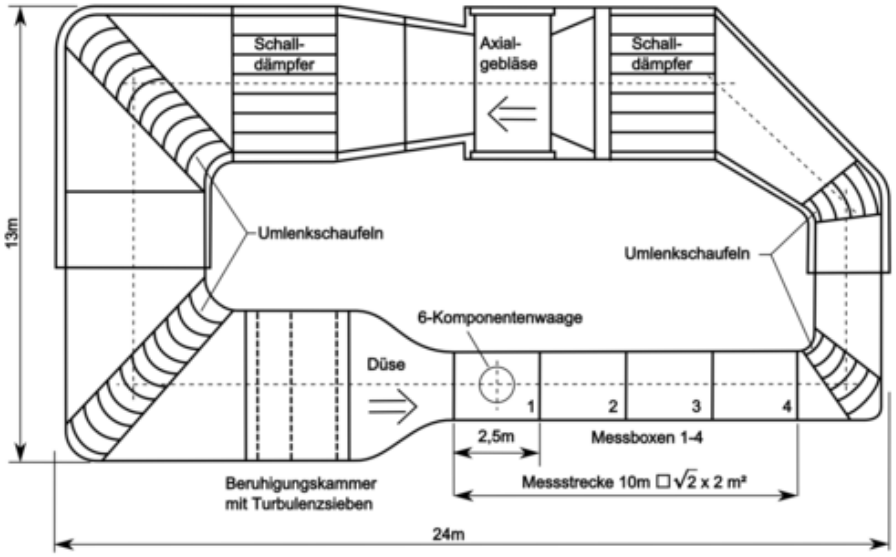


**Figure 3.13:** Technical drawing of the GroWiKa wind tunnel [48]


**Figure 3.14:** Frontal view of the model in the experimental section

The wind tunnel is equipped with a six-component scale with direct force introduction into load cells that allows the measure of forces and moments in three directions (see the scheme in Figure 3.15). The scale is built according to the platform scale principle, therefore features increased stiffness, so higher natural frequencies, but has the disadvantage of increased error due to the distance between the platform and the model center. The maximum allowed model weight is 3000 N. The scale accuracies are 0.1% for drag, lift and side force thus small enough to provide enough precision for our purposes. However, at the moment of the measurements the balance had a bias that has been corrected in the post-process phase. This is the main reason why, for the sake of intellectual integrity, these studies where only taken into account as one among many references for the validation of the CFD models for the DrivAer.

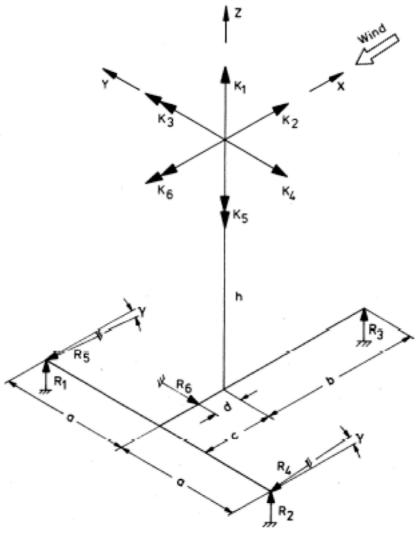


**Figure 3.15:** Scheme of the scale present in the GroWiKa wind tunnel

A Prandtl tube 305 mm long is installed on the top of the testing area (visible in Figure 3.16), and it has been used to measure both dynamic and static pressures inside the wind tunnel by means of a barometer (visible in Figure 3.16) to obtain flow velocity from the relation:

$$P_{tot} = P_{st} + P_{dyn} = P_{st} + \frac{1}{2}\rho U^2 \tag{3.2}$$

A thermocouple has been used for the thermal measurements, in order to calculate the density of air in the tunnel, whose value is needed for the evaluation of the flow velocity and the Reynolds number.

In order to get a flow visualization, tufts have been applied to the model, especially in the area covered by the wake, which is the most interesting area.


**Figure 3.16:** Pictures of the Pitot tube inside the tunnel (left) and of the barometer (rigth)

### Experiments

At first, in order to obtain consistent results, a side force calibration has been necessary; indeed, due to some minor non-symmetries in the model, when the model longitudinal plane is parallel to the direction of the flow a small value of side force arises, as a result of the interaction between model and wind. Thus it has been necessary to calibrate the yaw angle in order to have zero side force. By rotating the model of few degrees around the zero position, with steps of 0,1°, the graph in Figure 3.17 has been derived, which shows that the zero side force condition is reached at yaw angle equal $-0{,}5°$. The newly found calibrated angle has been therefore set as the reference zero yaw angle for the following experiments.

Once calibrated the side forces, in order to ensure that the experiments would have been performed in a condition of independence w.r.t. Reynolds number, it has been necessary to test the model in different condition of flow speed, to check the variability of drag coefficient. By acting on the rotational speed of the fan, the values plotted in Figure 3.17 have been found. As clear from this plot, after a certain value of $Re$ the fluctuation decreases considerably, suggesting that a Reynolds number indipendent condition has been reached. The residual bounded fluctuation is probably due to noise in the measurements and thermal evolution of the wind tunnel. In order to perform the following analysis properly, the wind speed has been therefore set to 40 m/s.

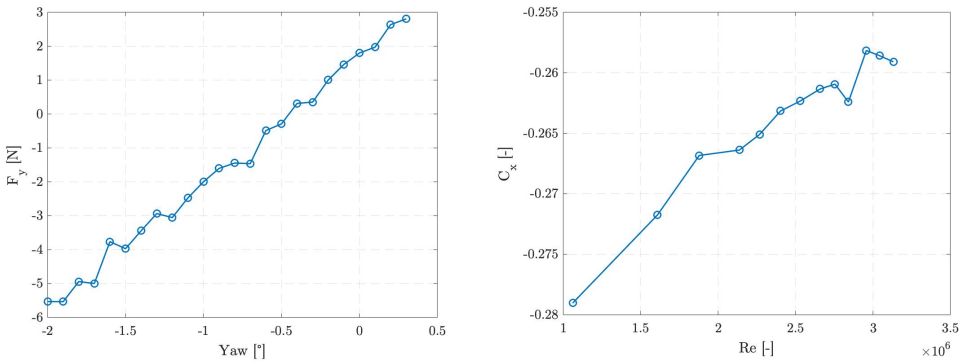


**Figure 3.17:** Zero side force analysis (left) and Reynolds number independency (right)

The results presented in this section have been collected for a speed of the wind of 40 m/s and for a yaw angle variation between $-10°$ and $10°$. The first thing that can be seen from Figure 3.18 is the behaviour of the side forces: as expected $C_y$ is 0 in 0° this means that the calibration of the model has been performed correctly. This force is linear with the yaw angle and this is reasonable due to the symmetry of the model: increasing the module of the yaw angle, more side area is hit by the wind, increasing so the module of the force (and so the coefficient). Regarding the drag coefficient the non-symmetry of the curve is due to the not perfect symmetry of the DriveAer model. The trend of the curve, is the one expected [22, 23]. For what concerns the lift coefficient, apart from a clear measurement error (due to disturbances) for a yaw angle of 5°, the trend of the curve is as expected [22, 23].

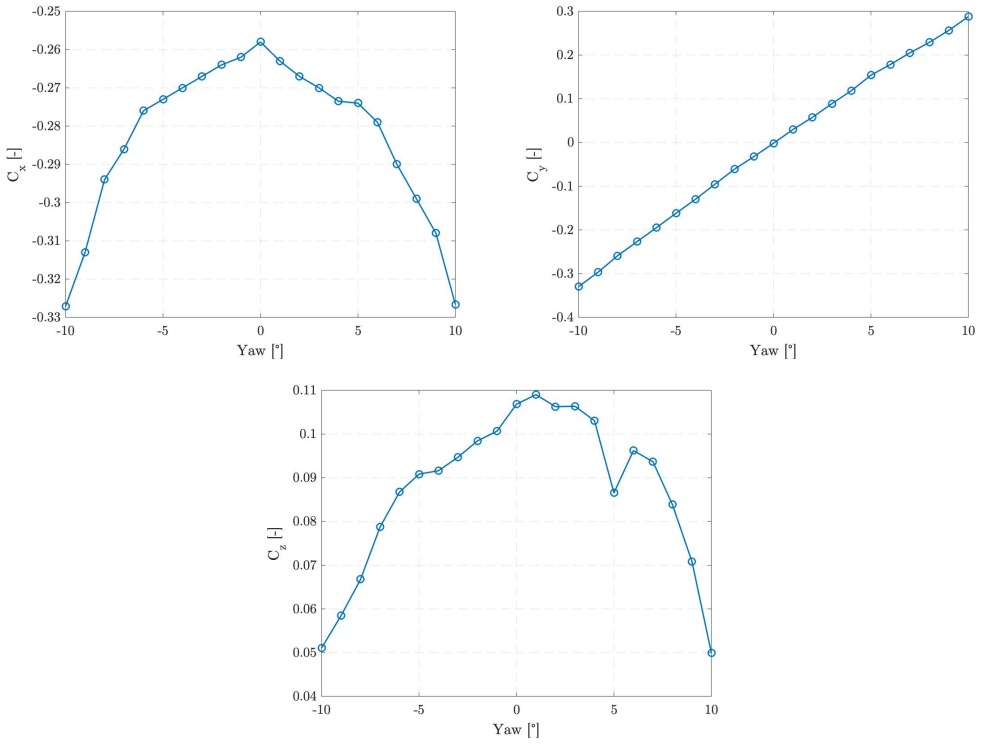


**Figure 3.18:** Aerodynamic coefficients for a yaw angle variation between $-10°$ and $10°$: $C_x$ (top left), $C_y$ (top right) and $C_z$ (bottom)

#### Flow Visualization

The presence of the tufts make possible some considerations about the behaviour of the flow around the car. In the left part of Figure 3.19 it is possible to visualise the wake on the rear end of the car for a yaw of 0°: the top tufts underline the formation of the shear layer, while the tufts in the middle of the rear shows the presence of vortices in the dead water. In the right part of Figure 3.19 it is possible to visualise the effects of the changing of the yaw angle to 10°: on the side and on the top of the car, the tufts are slanted not perpendicular to the longitudinal axle of the car, in the direction of the flow, while on the rear of the car, the effects of the increasing of the delta vortex of that side is clear thank to the tufts movement.

**Figure 3.19:** Flow visualization at a yaw angle of 0° (left) and 10° (right)

## 3.2 Validation

### 3.2.1 Moving Mesh Cases

For both the vehicles, the overall drag coefficient has been used to check for the grid independency in agreement with the SAE Standard J2966 [49], but nonetheless also the lift and side force coefficient will be reported. The set up for the validation at 10° has been once again in accordance with the SAE Standard J2966 [49]. In the next two sections, an overview on the method and results obtained in order to validate the CFD models with the wind tunnel simulations results is presented. Moreover, in order to check for the reliability of the obtained results, a comparison with data available in scientific literature is provided. Being the mesh setup for the Truck model derived from the setup for the DrivAer model, it has been decided to present firstly this last.

#### DrivAer

In order to validate the CFD model and assess the grid independency of the results obtained, three different meshes have been developed and tested. The numerical setup of these last, has been explained in Section 2.2. The general idea behind each mesh is the one visible in Figure 2.7, 2.9, 2.10 and 2.11. Nevertheless, while the second and third mesh are exactly as presented in Section 2.2, with just a refinement difference, the first mesh tested has been developed without a refinement box on the outlet interface between the dynamic and the static domain. This is clearly visible in Figure 3.20.

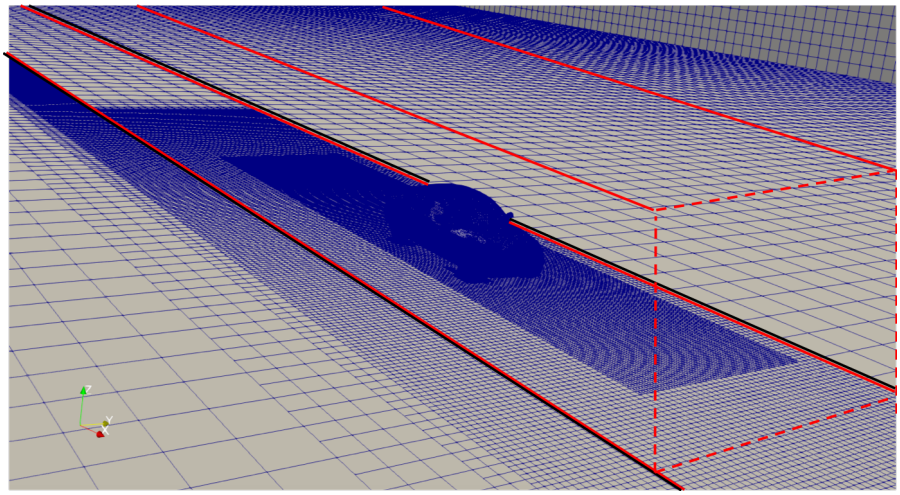

**Figure 3.20:** Particular of the first mesh developed. The outer static domain is the one with black contour while the inner dynamic domain has a red contour

All the simulations have been run with the same setup: the absolute wind speed has been set to $U = 4{,}41\,\mathrm{m/s}$ from the negative to the positive $y$ direction, while the speed of the vehicle has been set to $v = 25\,\mathrm{m/s}$ from the negative to the positive $x$ direction. These parameters have been set in order to reach a relative yaw angle of $\beta = 10°$ and a Reynolds number of $Re = 7.805{\cdot}10^6$, higher than the one of the wind tunnel simulations. All the simulations have been run for $t = 10\,\mathrm{s}$ in order to be sure to reach aerodynamic coefficients and pressure residuals convergence. In Table 3.1 the differences between the 3 developed meshes is reported. As clear, there is a consistent difference between the number of elements of the first mesh and the other two; this because of the coarser layers around the vehicle and the absence of the long refinement box as previously explained. The differences between the second and the third meshes are only the number of layers levels (6 in the third and 5 in the second) that is the reason why the $y+$ of the third mesh is lower and the background mesh size. These two differences led to a tremendous increase of computational effort; however, run this simulation has been fundamental to assess the grid independency. The choice of the time step has been driven by the necessity to have a maximum Courant number ($CFL$) as much as possible near to 1 in order to have stable and reliable results [37]. For what concerns the adimensional $y+$ value, as well known, in order to have a good description of the velocity profile of the field near the wall surfaces, it is important to keep it between 30 and 300 [37]. Before analysing the results one last comment has to be done on the very low number of mesh elements in error, 24 over $14.6{\cdot}10^6$ cells: this has been achieved with a deep study of the refinement parameters of the mesh; the elements in error are all due to their skewness, that anyway is in an acceptable range. However, this is a common problem when dealing with an interface between static and moving mesh.

| Data | mesh 1 | mesh 2 | mesh 3 | unit |
|---|---|---|---|---|
| $n.cells$ | $4.4{\cdot}10^{6}$ | $14.6{\cdot}10^{6}$ | $22.4{\cdot}10^{6}$ | – |
| $L_{blockMesh}$ | 1 | 1 | 0.5 | m |
| $L_{blockMIN}$ | $15.6{\cdot}10^{-}3$ | $15.6{\cdot}10^{-}3$ | $7.8{\cdot}10^{-}3$ | m |
| $Skewness_{MAX}$ | 6.54 (23 cells) | 6.73 (24 cells) | 4.61 (2 cells) | – |
| $\Delta t$ | $2.5{\cdot}10^{-}4$ | $2.5{\cdot}10^{-}4$ | $2{\cdot}10^{-}4$ | s |
| $CFL_{MAX}$ | 1.415 | 1.499 | 2.030 | – |
| $y{+}_{meanDrivAer}$ | 320.43 | 135.08 | 98.65 | – |
| $p_{residual}$ | $1.5{\cdot}10^{-}4$ | $2.3{\cdot}10^{-}4$ | $4{\cdot}10^{-}4$ | $m^2/s^2$ |
| $n_{cores}$ | 80 | 120 | 520 | – |
| $t_{computational}$ | 5 | 6 | 2.5 | *days* |

**Table 3.1:** Comparison of the 3 different meshes tested for the DrivAer model

In Figure 3.21 it is possible to see the trend of the ratio between the simulated aerodynamic coefficients and the ones measured in the wind tunnel simulations. From this plot is clear that there is no consistent difference between the results of the second and third mesh and that both are capable of describing well what measured in the wind tunnel. For this reason and since there is a great difference of computational effort between the two, the choice of the second mesh as a base for all the other simulations of this work has seemed obvious. For the sake of clarity, in Table 3.2, the aerodynamic coefficients obtained from CFD simulations as well as the ones from wind tunnel simulations and from Wieser et al. [25] and Strangfeld et al. [22] are reported. It has to be noticed that in Wieser et al. [25], it is mentioned 'Improving aerodynamic characteristics: Challenges and opportunities' in which the drag coefficient is the one reported. Moreover, the study of Strangfeld et al. [22] has been conducted on a fastback DrivAer model, which has a lower side area w.r.t. the notchback model of this study [41].

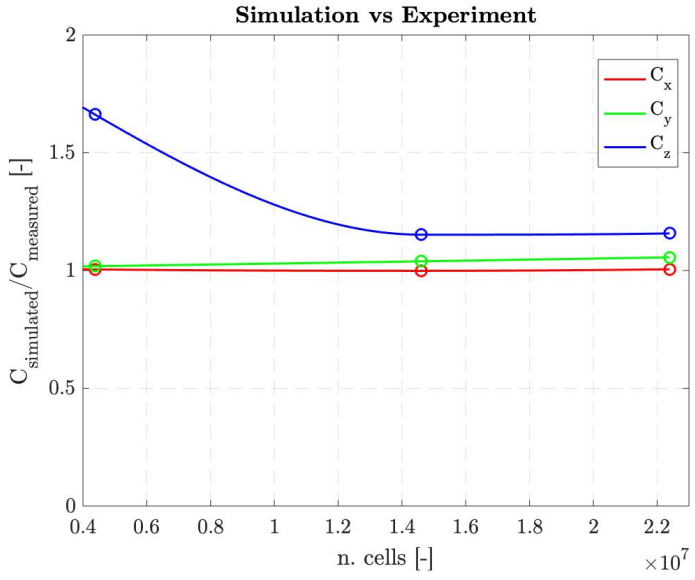


**Figure 3.21:** Trend of the ratio between the simulated aerodynamic coefficients and the ones measured in the wind tunnel simulations

| Source | $C_x$ | $C_y$ | $C_z$ |
|---|---|---|---|
| Mesh 1 | −0.328 | 0.293 | 0.084 |
| Mesh 2 | −0.326 | 0.299 | 0.058 |
| Mesh 3 | −0.328 | 0.304 | 0.059 |
| Wind Tunnel | −0.327 | 0.287 | 0.051 |
| Paper 1 [25] | −0.332 | – | 0.056 |
| Paper 2 [22] | – | 0.285 | 0.050 |

**Table 3.2:** Comparison of the results obtained from the 3 different meshes tested for the DrivAer model, the wind tunnel tests and two other studies

### Truck

Having already validated the DrivAer CFD model, in order to validate the CFD model and assess the grid independency of the results obtained for the Truck, two different meshes have been developed and tested starting from the mesh 2 of the DrivAer validation. For this reason the two meshes will be called mesh "2" and mesh "2.1". The numerical setup of these last, has been explained in Section 2.2. The general idea behind each mesh is the one visible in Figure 2.7, 2.9, 2.10 and 2.11. The two meshes are equal apart from a refinement difference.

Also in this case, the simulations have been run with the same setup: the absolute wind speed has been set to $U = 4{,}41\,\mathrm{m/s}$ from the negative to the positive $y$ direction, while the speed of the vehicle has been set to $v = 25\,\mathrm{m/s}$ from the negative to the positive $x$ direction. These parameters have been set in order to reach a relative yaw angle of $\beta = 10°$ and a Reynolds number of $Re = 1.325{\cdot}10^7$, much higher than the one of the wind tunnel simulations. All the simulations have been run for $t = 10\,\mathrm{s}$ in order to be sure to reach aerodynamic coefficients and pressure residuals convergence. In Table 3.3 the differences between the 2 developed meshes is reported. The difference between the first and second meshes (mesh 2 and 2.1) is only related to the definition of the layers (that is the reason why the $y+$ of the mesh 2.1 is lower). The choice of the time step has been driven by the necessity to have a maximum Courant number ($CFL$) as much as possible near to 1 in order to have stable and reliable results [37]. For what concerns the adimensional $y+$ value, as well known, in order to have a good description of the velocity profile of the field near the wall surfaces, it is important to keep it between 30 and 300 [37]. Before analysing the results one last comment has to be done on the very low number of mesh elements in error of the mesh 2.1, 55 over $18.3{\cdot}10^6$ cells: this has been achieved with a deep study of the refinement parameters of the mesh; the elements in error are all due to their skewness, that anyway is in an acceptable range. However, this is a common problem when dealing with an interface between static and moving mesh.

| Data | mesh 2 | mesh 2.1 | unit |
|---|---|---|---|
| $n.cells$ | $15.9{\cdot}10^6$ | $18.3{\cdot}10^6$ | – |
| $L_{blockMesh}$ | 1 | 1 | m |
| $L_{blockMIN}$ | $15.6{\cdot}10^{-}3$ | $15.6{\cdot}10^{-}3$ | m |
| $Skewness_{MAX}$ | 36.9 (72 cells) | 8.86 (55 cells) | – |
| $\Delta t$ | $2{\cdot}10^{-}4$ | $2{\cdot}10^{-}4$ | s |
| $CFL_{MAX}$ | 1.343 | 1.293 | – |
| $y{+}_{meanTruck}$ | 249.09 | 108.26 | – |
| $p_{residual}$ | $6.4{\cdot}10^{-}4$ | $7.9{\cdot}10^{-}4$ | $m^2/s^2$ |
| $n_{cores}$ | 80 | 120 | – |
| $t_{computational}$ | 6 | 5 | *days* |

**Table 3.3:** Comparison of the 2 different meshes tested for the Truck model

In Figure 3.22 it is possible to see the trend of the ratio between the simulated aerodynamic coefficients and the ones measured in the wind tunnel simulations. From this plot is clear that there is no consistent difference between the results of the mesh 2 and 2.1, but it is also clear that the mesh 2.1 is more capable of represent the results of wind tunnel simulations w.r.t. the mesh 2. For this reason and since there is not a big computational effort difference between the two, the choice of the mesh 2.1 as a base for all the other simulations of this work has seemed obvious. For the sake of clarity, in Table 3.4, the aerodynamic coefficients obtained from CFD simulations as well as the ones from wind tunnel simulations and from Cheli et al. [13] and Tagliavia Ramírez [2] are reported. It has to be noticed that in Cheli et al. [13],the coefficients come from wind tunnel simulations, while in Tagliavia Ramírez [2] they come from static mesh CFD simulations.

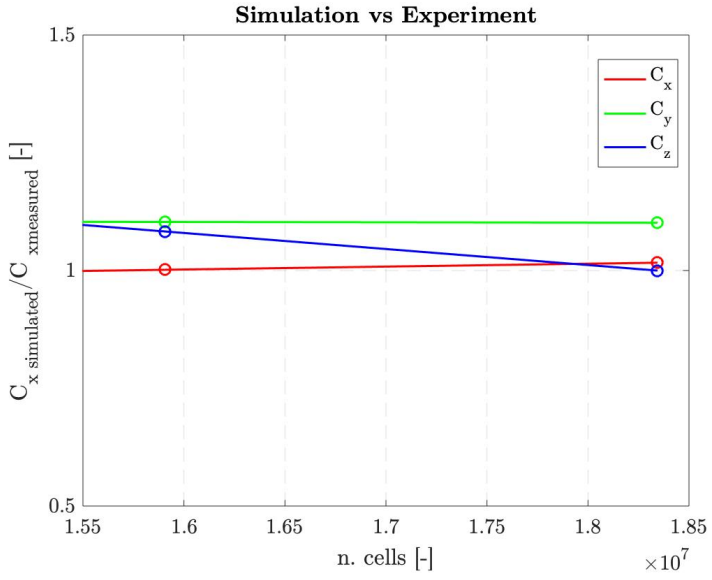


**Figure 3.22:** Trend of the ratio between the simulated aerodynamic coefficients and the ones measured in the wind tunnel simulations

| Source | $C_x$ | $C_y$ | $C_z$ |
|---|---|---|---|
| Mesh 2 | $-0.982$ | 0.275 | 0.084 |
| Mesh 2.1 | $-0.986$ | 0.274 | 0.078 |
| Wind Tunnel | $-0.980$ | 0.249 | 0.078 |
| Paper 1 [13] | $-1.03$ $-1.27$ | 0.16 0.40 | $-0.02$ 0.06 |
| Paper 2 [2] | $-0.98$ | 0.25 | 0.12 |

**Table 3.4:** Comparison of the results obtained from the 2 different meshes tested for the Truck model, the wind tunnel tests and two other studies

### 3.2.2 Static Mesh Cases

For reasons that will be clarified in Chapter 5, it has been necessary to develop a static mesh CFD model whom validation will be presented in this section. For both the vehicles, the overall drag coefficient has been used to check for the grid independency in agreement with the SAE Standard J2966 [49], but nonetheless also the lift and side force coefficient will be reported. The set up for the validation at 10° has been once again in accordance with the SAE Standard J2966 [49]. In the next two sections, an overview on the method and results obtained in order to validate the CFD models with the wind tunnel simulations results is presented.

#### DrivAer

In order to validate the CFD model and assess the grid independency of the results obtained, three different meshes have been developed and tested. The numerical setup of these last, has been explained in Section 2.2. The general idea behind each mesh is the one visible in Figure 2.15, 2.16 and 2.17. Nevertheless, the three meshes are refined differently for what concerns the number of layers and the refinement boxes dimensions. The chosen mesh is the one visible in the previously mentioned figures.

All the simulations have been run with the same setup: the relative wind speed has been set to $U = 40\,\mathrm{m/s}$. The relative yaw angle has been set to $\beta = 10°$ and the resulting Reynolds number has been $Re = 1.004{\cdot}10^7$, much higher than the one of the wind tunnel simulations. All the simulations have been run for 5000 time steps in order to be sure to reach aerodynamic coefficients and pressure residuals convergence. In Table 3.5 the differences between the 3 developed meshes is reported. As clear, the number of elements from the first to the third mesh increases. The $y+$ of the third mesh is the best possible according to the theory [37].

| Data | mesh 1 | mesh 2 | mesh 3 | unit |
|---|---|---|---|---|
| $n.cells$ | $20.2{\cdot}10^6$ | $27.2{\cdot}10^6$ | $34.1{\cdot}10^6$ | – |
| $L_{blockMesh}$ | 1 | 1 | 1 | m |
| $L_{blockMIN}$ | $7.8{\cdot}10^{-}3$ | $3.9{\cdot}10^{-}3$ | $3.9{\cdot}10^{-}3$ | m |
| $y+_{meanDrivAer}$ | 150.22 | 100.23 | 35.90 | – |
| $p_{residual}$ | $7.22{\cdot}10^{-}4$ | $4.03{\cdot}10^{-}5$ | $9.05{\cdot}10^{-}5$ | $m^2/s^2$ |
| $n_{cores}$ | 56 | 56 | 56 | – |
| $t_{computational}$ | 10 | 13 | 16 | $hours$ |

**Table 3.5:** Comparison of the 3 different meshes tested for the DrivAer model

In Figure 3.23 it is possible to see the trend of the ratio between the simulated aerodynamic coefficients and the ones measured in the wind tunnel simulations. Being these simulations much less computationally expensive w.r.t. the moving mesh ones, the choice of the third mesh as a base for all the other simulations of this work has seemed obvious. For the sake of clarity, in Table 3.6, the aerodynamic coefficients obtained from CFD simulations as well as the ones from wind tunnel simulations are reported. It has to be noticed that there is a consistent difference between $C_{zMeasured}$ and $C_{zSimulated}$, but these are very small numbers and unfortunately this kind of errors are common when dealing with lift coefficients.

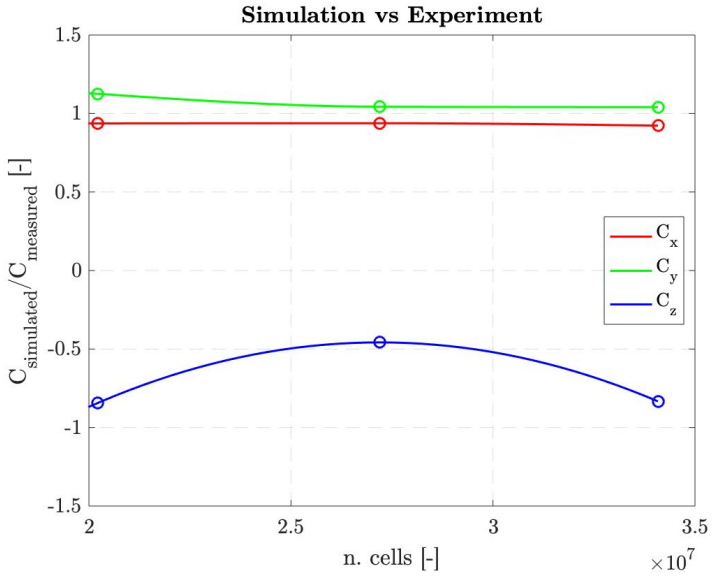


**Figure 3.23:** Trend of the ratio between the simulated aerodynamic coefficients and the ones measured in the wind tunnel simulations

| Source | $C_x$ | $C_y$ | $C_z$ |
|---|---|---|---|
| Mesh 1 | −0.306 | 0.324 | −0.043 |
| Mesh 2 | −0.307 | 0.300 | −0.023 |
| Mesh 3 | −0.302 | 0.298 | −0.042 |
| Wind Tunnel | −0.327 | 0.287 | 0.051 |

**Table 3.6:** Comparison of the results obtained from the 3 different meshes tested for the DrivAer model with the wind tunnel tests

### Truck

In order to validate the CFD model and assess the grid independency of the results obtained, three different meshes have been developed and tested. The numerical setup of these last, has been explained in Section 2.2. The general idea behind each mesh is the one visible in Figure 2.15, 2.16 and 2.17. Nevertheless, the three meshes are refined differently for what concerns the number of layers and the refinement boxes dimensions. The chosen mesh is the one visible in the previously mentioned figures.

All the simulations have been run with the same setup: the relative wind speed has been set to $U = 40\,\mathrm{m/s}$. The relative yaw angle has been set to $\beta = 10°$ and the resulting Reynolds number has been $Re = 2.088{\cdot}10^7$, much higher than the one of the wind tunnel simulations. All the simulations have been run for 5000 time steps in order to be sure to reach aerodynamic coefficients and pressure residuals convergence. In Table 3.7 the differences between the 3 developed meshes is reported. As clear, the number of elements from the first to the third mesh increases. The $y+$ of the third mesh is the best possible according to the theory [37].

| Data | mesh 1 | mesh 2 | mesh 3 | unit |
|---|---|---|---|---|
| $n.cells$ | $23.6{\cdot}10^6$ | $75.9{\cdot}10^6$ | $104.2{\cdot}10^6$ | – |
| $L_{blockMesh}$ | 1 | 1 | 0.5 | m |
| $L_{blockMIN}$ | $7.8{\cdot}10^{-}3$ | $3.9{\cdot}10^{-}3$ | $3.9{\cdot}10^{-}3$ | m |
| $y+_{meanTruck}$ | 225.32 | 105.21 | 36.66 | – |
| $p_{residual}$ | $1.12{\cdot}10^{-}4$ | $6.70{\cdot}10^{-}5$ | $9.95{\cdot}10^{-}6$ | $m^2/s^2$ |
| $n_{cores}$ | 56 | 56 | 56 | – |
| $t_{computational}$ | 11 | 20 | 26 | *hours* |

**Table 3.7:** Comparison of the 3 different meshes tested for the Truck model

In Figure 3.24 it is possible to see the trend of the ratio between the simulated aerodynamic coefficients and the ones measured in the wind tunnel simulations. Being these simulations much less computationally expensive w.r.t. the moving mesh ones, the choice of the third mesh as a base for all the other simulations of this work has seemed obvious. For the sake of clarity, in Table 3.8, the aerodynamic coefficients obtained from CFD simulations as well as the ones from wind tunnel simulations are reported.

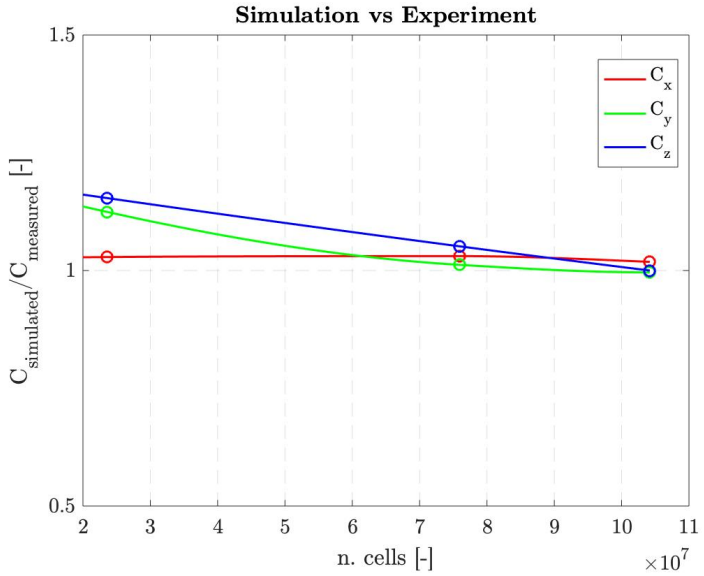


**Figure 3.24:** Trend of the ratio between the simulated aerodynamic coefficients and the ones measured in the wind tunnel simulations

| Source | $C_x$ | $C_y$ | $C_z$ |
|---|---|---|---|
| Mesh 1 | $-0.980$ | 0.280 | 0.090 |
| Mesh 2 | $-1.008$ | 0.252 | 0.082 |
| Mesh 3 | $-1.010$ | 0.248 | 0.078 |
| Wind Tunnel | $-0.980$ | 0.249 | 0.078 |

**Table 3.8:** Comparison of the results obtained from the 3 different meshes tested for the Truck model with the wind tunnel tests

# Chapter 4

# Vehicle Dynamics Models

Characterize the dynamic response of the vehicle with a good level of approximation is a crucial topic when the aim of the simulation is to provide a solution as much as possible close to the real scenario. But then, if a too simple model could take to wrong results, a too complex solution could not only be difficult to implement, but also to validate without proper experimental data. It is important so to find a good trade-off between the required level of accuracy of the solution and the quantity of data available to characterize the system.

There are many vehicle dynamics models fully described and validated in the scientific literature, from simple punctual mass models to complex multi-body models [50–53]. For the purpose of this work, it has been deemed necessary to choose a model complex enough to describe the degrees of freedom that are influenced most by a strong crosswind. For this reason, a "four contact model" (also known as "double track model") has been chosen.

The four contact model is a 6 d.o.f. model, in which w.r.t. a simple single track model, the wheels on the same axle are separated. This is the reason why it is possible to consider the lateral load transfer due to lateral acceleration and lateral forces that in this study are of fundamental importance. Moreover, thanks to the separation of the wheels on the same axle, there is a better modelling of the non-linearities of contact forces between tyres and road. The assumptions made for this particular case with respect to the complete four contact model presented in *The Science of Vehicle Dynamics*[51] are:

- Vehicle longitudinal speed $v_x$ is imposed to be constant,
- Vertical displacement and pitch are neglected (and so are longitudinal load transfers),
- Roll motion is considered simplified.

The degrees of freedom of the model are thus:

- Vehicle lateral speed $v_y$,
- Vehicle yaw rate $\dot{\psi}$,
- Vehicle roll rate $\dot{\rho}$.

Two reference frames are used:

1. A global inertial reference frame fixed on the ground $O - XYZ$
2. A moving reference frame on the ground, moving in the plane $X - Y$ with the $x$ axis aligned with vehicle roll axis pointing in the positive longitudinal vehicle motion, $z$ axis pointing upward and $y$ as a result from the right-hand rule.

Versors of the global reference frame are $i$, $j$ and $k$ and the Cartesian component are named with capitol letters (e.g. $V_x$, $V_y$). Versors of the moving reference frame are $i_L$, $j_L$ and $k_L$ and the Cartesian component are named with small letters (e.g. $v_x$, $v_y$). In the next two sections a full description of the model and of the parameters for the two investigated vehicles is provided.

# 4.1 Truck

## 4.1.1 Vehicle Geometry and Mass Distribution

The mass of the body $m_b$ and the position of the body c.o.g. $G_b$ are fixed. The distance between the body c.o.g. and the front axle of the vehicle is $a_b$, while we name the height of the c.o.g. from the ground $z_{Gb}$. For what concerns the lumped mass, the distance between the lumped mass c.o.g. and the front axle of the vehicle $a_l$ is assumed to be constant while the height of the c.o.g. from the ground $z_{Gl}$ could be calculated as:

$$z_{Gl} = z_{Glmin} + \lambda \cdot (z_{Glmax} - z_{Glmin}) \tag{4.1}$$

where $\lambda$ is the load ratio: if the vehicle is empty $\lambda = 0$, if the vehicle is fully loaded $\lambda = 1$. This simple hypothesis can be a good approximation in case of granular medium transported by the truck. The lumped mass could be evaluated thus as:

$$m_l = \lambda \cdot m_{lmax} \tag{4.2}$$

being $m_{lmax}$ the maximum mass that the vehicle can load.

Knowing the position of the body and of the lumped mass c.o.g., it is possible to compute the position of the c.o.g. of the total sprung mass:

$$a = \frac{a_b m_b + a_l m_l}{m_b + m_l} \tag{4.3a}$$

$$z_G = \frac{z_{Gb} m_b + z_{Gl} m_l}{m_b + m_l} \tag{4.3b}$$

Once evaluated the mass of the vehicle, the estimation of the moments of inertia along $x$ and $z$ axes is based on the assumption that the lumped mass is a homogeneous parallelepiped whose height grows with $\lambda$. Thus, the moments of inertia are:

$$J_{xl} = \frac{m_l}{12} \left( w_l^2 + (\lambda h_l)^2 \right) \tag{4.4a}$$

$$J_{zl} = \frac{m_l}{12}\left(l_l^2 + w_l^2\right) \tag{4.4b}$$

where: $h_l$ is the maximum height of the lumped mass, $w_l$ is the width and $l_l$ is the length of the parallelepiped which are assumed to be constant and equal to the cargo bed of the vehicle. The total moments of inertia, considering also the inertia of front and real axles $J_{za}$ and $J_{za}$ are:

$$J_x = J_{xb} + m_b\left(h_G - h_{Gb}\right)^2 + J_{xl} + m_l\left(h_G - h_{Gl}\right)^2 \tag{4.5a}$$

$$J_z = J_{zb} + m_b\left(a - a_b\right)^2 + J_{al} + m_l\left(a_l - a\right)^2 + J_{za} + J_{zp} \tag{4.5b}$$

In Figure 4.1 a scheme of the masses and c.o.g. of the vehicle is reported. In Table 4.1 all the parameters used to characterize the truck are listed. The reference model for this study is the same as in Sterling et al. [40].

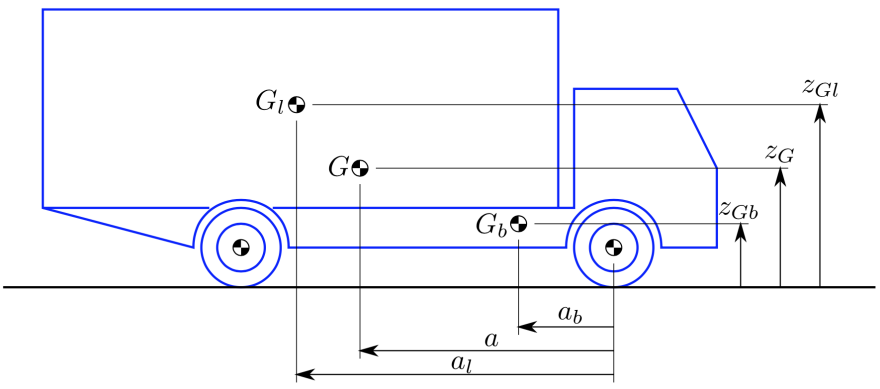


**Figure 4.1:** Vehicle mass distribution

| parameter | description | unit | value |
|---|---|---|---|
| $a$ | c.o.g./front axle distance | m | from eq. |
| $a_b$ | body c.o.g./front axle distance | m | 0.534 |
| $a_l$ | lumped mass c.o.g./front axle distance | m | 3.35 |
| $A_f$ | vehicle frontal surface | $m^2$ | 6.6 |
| $A_l$ | vehicle lateral surface | $m^2$ | 18.9 |
| $b$ | c.o.g./rear axle distance | m | $p - a$ |
| $c$ | vehicle front and rear track | m | 1.74 |
| $h_l$ | vehicle cargo bed height | m | 2.62 |
| $J_{xb}$ | vehicle body moment of inertia along $x$ axis | $kgm^2$ | 1016 |
| $J_{za}$ | front axle moment of inertia along $z$ axis | $kgm^2$ | 440 |
| $J_{zb}$ | vehicle body moment of inertia along $z$ axis | $kgm^2$ | 4795 |
| $J_{zp}$ | rear axle moment of inertia along $z$ axis | $kgm^2$ | 440 |
| $l_l$ | vehicle cargo bed length | m | 6.16 |
| $m_a$ | front axle unsprung mass | kg | 706 |
| $m_b$ | vehicle body sprung mass | kg | 2030 |
| $m_p$ | rear axle unsprung mass | kg | 706 |
| $m_{lmax}$ | maximum lumped mass | kg | $1200 - m_b$ |
| $p$ | vehicle wheelbase | m | 4.42 |
| $Rr$ | wheels roll radius | m | 0.4 |
| $x_P$ | wind application point x-distance from c.o.g. | m | $a$ |
| $w_l$ | vehicle cargo bed width | m | 2.50 |
| $z_{Gb}$ | height of body c.o.g. from ground | m | 1.058 |
| $z_{Glmin}$ | minimum height of load mass c.o.g. | m | 0.88 |
| $z_{Glmax}$ | maximum height of load mass c.o.g. | m | $z_{Glmin} + h_l/2$ |
| $z_P$ | wind application point coordinate on $z$ axis | m | 1.354 |
| $z_R$ | roll centre height from ground | m | 0.4 |
| $\lambda$ | load of the vehicle | - | $0 \leqslant \lambda \leqslant 1$ |

**Table 4.1:** Truck dynamics model parameters

### 4.1.2 Equations of Motion

In order to write the equations of motion, it is fundamental to state which forces are acting on the vehicle. In Figure 4.2 all the forces acting on the truck are reported, with a reference system fixed in the c.o.g. However, all the equations of motion will be referred to the two reference frames presented at the beginning of this chapter.

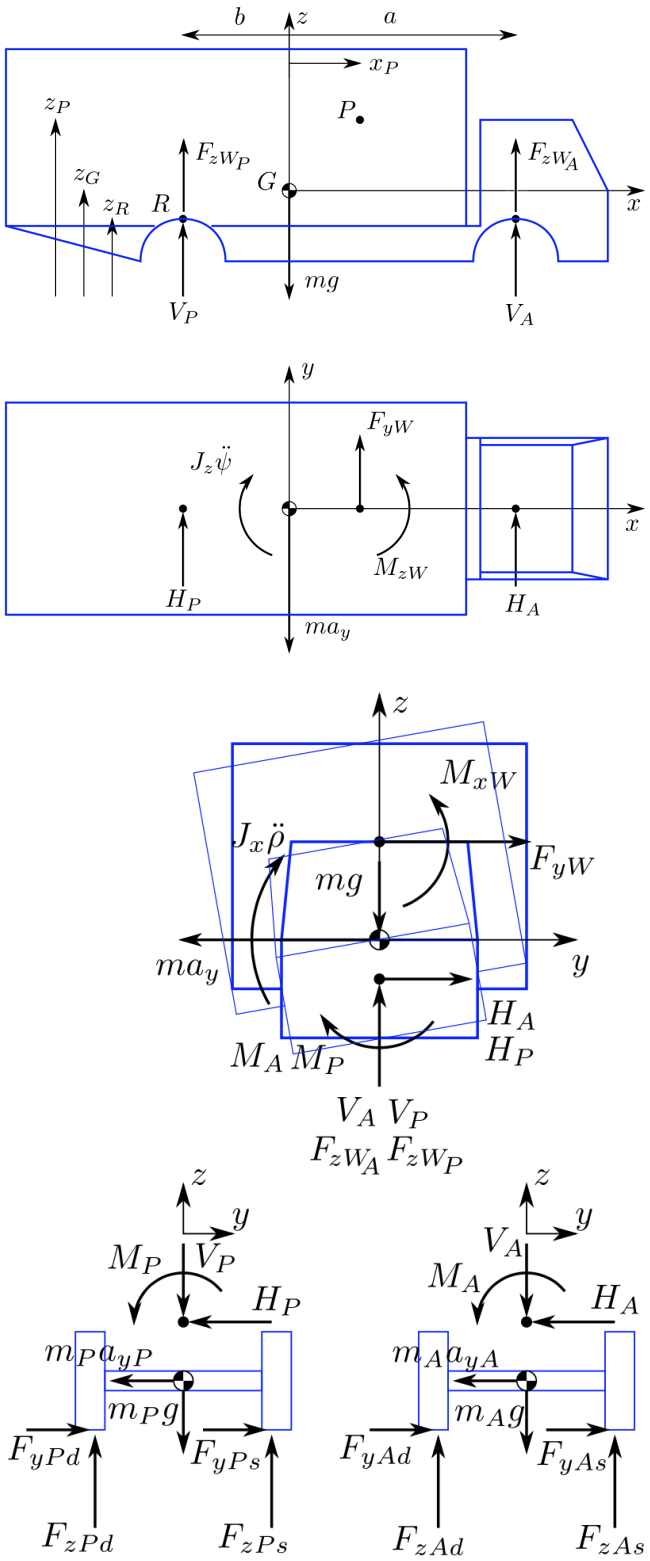


**Figure 4.2:** Scheme of the forces acting on the vehicle

### Vertical Equilibrium

The vertical translation and the moment equilibrium in the $x-z$ plane, considering the sprung masses of the vehicle give the expression of vertical reaction forces in the front and rear roll centres ($V_A$ and $V_P$ respectively):

$$V_A = mg\frac{b}{p} - F_{zW_A} \tag{4.6a}$$

$$V_P = mg\frac{a}{p} - F_{zW_P} \tag{4.6b}$$

where $F_{z_{WA}}$ and $F_{z_{WP}}$ are the wind lifting forces as detailed in Section 4.1.3. Considering then front and rear axles wheels vertical equilibrium and substituting Equations 4.6, the axles normal contact forces ($F_{zA}$ and $F_{zP}$) can be computed:

$$F_{zA} = F_{zAd} + F_{zAs} = V_A + m_A g = \left(m\frac{b}{p} + m_A\right) g - F_{zW_A} \tag{4.7a}$$

$$F_{zP} = F_{zPd} + F_{zPs} = V_P + m_P g = \left(m\frac{a}{p} + m_P\right) g - F_{zW_P} \tag{4.7b}$$

### Lateral Equilibrium

The lateral translation equilibrium, along $y$ axis in the $x-y$ plane is:

$$ma_y = H_A + H_P + F_{yW} \tag{4.8}$$

where $H_A$ and $H_P$ are the horizontal reaction forces in the front and rear roll centres, while $F_{yW}$ is the wind side force. For the front wheels the $y$ translation equilibrium is:

$$F_{yA} = F_{yAs} + F_{yAd} = m_A a_{yA} + H_A = m_A\left(a_y + a\ddot{\psi} + (z_G - z_R)\ddot{\rho}\right) + H_A \tag{4.9}$$

where $F_{yA}$ is the axle cornering force, while for the rear wheels:

$$F_{yP} = F_{yPs} + F_{yPd} = m_P a_{yP} + H_P = m_P\left(a_y + b\ddot{\psi} + (z_G - z_R)\ddot{\rho}\right) + H_P \tag{4.10}$$

Substituting Equations 4.9 and 4.10 in 4.8 it is possible to obtain the first equilibrium equation of the entire vehicle:

$$\left(m + m_A + m_P\right) a_y + \left(m_A a + m_P b\right)\ddot{\psi} + \left(m_A + m_P\right)\left(z_G - z_R\right)\ddot{\rho} = F_{yA} + F_{yP} + F_{yW} \tag{4.11}$$

### Yaw Equilibrium

Considering now the yaw rotation $\psi$ in the $x-y$ plane, the rotation equilibrium around the sprung mass c.o.g. is:

$$J_z\ddot{\psi} = H_A a - H_P b + M_{zW} + F_{yW} x_P \tag{4.12}$$

where $M_{zW}$ is the aerodynamic yawing moment and so substituting Equations 4.9 and 4.10 in 4.12 we obtain the equation of motion:

$$\begin{aligned}&(m_A a - m_P b)\, a_y + \left(J_z + m_A a^2 + m_P b^2\right)\ddot{\psi} + (m_A a - m_P b)\,(z_G - z_R)\,\ddot{\rho} = \\ &= F_{yA} a - F_{yP} b + M_{zW} + F_{yW} x_P\end{aligned} \tag{4.13}$$

### Roll Equilibrium

The roll reaction moments due to the suspension total roll stiffnesses ($k_A$ and $k_P$) and damping coefficients ($r_A$ and $r_P$) are:

$$M_A = k_A \rho + r_A \dot{\rho} \tag{4.14}$$

$$M_P = k_P \rho + r_P \dot{\rho} \tag{4.15}$$

The roll equation of motion is thus:

$$J_x\ddot{\rho} = M_{xW} - F_{yW}\,(z_P - z_R) + m a_y\,(z_G - z_R) + mg\,(z_G - z_R)\sin\rho - M_A - M_P \tag{4.16}$$

The roll rotation equilibrium of front and rear wheels, is needed to write the load transfer equations on the two axles ($\Delta F_{zA}$ and $\Delta F_{zP}$) which allows to compute the wheels vertical forces that for the front wheels are:

$$F_{zAd} = \frac{F_{zA}}{2} + \Delta F_{zA} \tag{4.17a}$$

$$F_{zAs} = \frac{F_{zA}}{2} - \Delta F_{zA} \tag{4.17b}$$

The roll rotation equilibrium of front wheels is:

$$\Delta F_{zA} = \frac{1}{c_A}\left(M_A + H_A z_R + m_A a_{yA} R_r\right) \tag{4.18}$$

with $a_{yA} = a_y + a\ddot{\psi} + (z_G - z_R)\ddot{\rho}$.
The roll rotation equilibrium of rear wheels is instead:

$$\Delta F_{zP} = \frac{1}{c_P}\left(M_P + H_P z_R + m_P a_{yP} R_r\right) \tag{4.19}$$

with $a_{yP} = a_y - b\ddot{\psi} + (z_G - z_R)\ddot{\rho}$.

### Tyres Forces

In order to evaluate lateral tyres forces, a 94' Pacejka simple model [54, 55] with normal load dependency is used:

$$F_{yi} = -D_i \sin\left(C \arctan\left(B\alpha_i - E\left(B\alpha_i - \arctan\left(B\alpha_i\right)\right)\right)\right) \tag{4.20}$$

where $B$, $C$ and $E$ are constant coefficients, while $D$ is computed as:

$$D_i = \left(q + s\frac{F_{zi} - F_{zi0}}{N_{i0}}\right) F_{zi} \tag{4.21}$$

Slip angles of the equivalent single track vehicle model of front and rear axles are respectively:

$$\alpha_{Ad} = \delta - \arctan\left(\frac{v_y + \dot{\psi}a}{v_x + \frac{c}{2}}\right) \tag{4.22a}$$

$$\alpha_{As} = \delta - \arctan\left(\frac{v_y + \dot{\psi}a}{v_x - \frac{c}{2}}\right) \tag{4.22b}$$

$$\alpha_{Pd} = -\arctan\left(\frac{v_y - \dot{\psi}b}{v_x + \frac{c}{2}}\right) \tag{4.23a}$$

$$\alpha_{Ps} = -\arctan\left(\frac{v_y - \dot{\psi}b}{v_x - \frac{c}{2}}\right) \tag{4.23b}$$

### System of Equations

The system of equations to be solved numerically is so:

$$\begin{bmatrix} m + m_A + m_P & m_A a - m_P b & (m_A + m_P)(z_G - z_R) \\ m_A a - m_P b & J_z + m_A a^2 + m_P b^2 & (m_A a - m_P b)(z_G - z_R) \\ -m(z_G - z_R) & 0 & J_x \end{bmatrix} \begin{Bmatrix} a_y \\ \ddot{\psi} \\ \ddot{\rho} \end{Bmatrix} =$$

$$= \begin{Bmatrix} F_{yA} + F_{yP} + F_{yW} \\ F_{yA}a - F_{yP}b + M_{zW} + F_{yW}x_P \\ M_{xW} - F_{yW}(z_P - z_R) + mg(z_G - z_R)\sin\rho - M_A - M_P \end{Bmatrix}$$

$$\begin{bmatrix} 1 & 1 \\ a & -b \end{bmatrix} \begin{Bmatrix} H_A \\ H_P \end{Bmatrix} = \begin{Bmatrix} ma_y - F_{yW} \\ J_z\ddot{\psi} - M_{xW} - F_{yW}x_P \end{Bmatrix}$$

$$\Delta F_{zA} = \frac{1}{c_A}\left(M_A + H_A z_R + m_A a_{yA} R_r\right)$$

$$\Delta F_{zP} = \frac{1}{c_P}\left(M_P + H_P z_R + m_P a_{yP} R_r\right)$$

$$F_{yi} = -D_i \sin\left(C \arctan\left(B\alpha_i - E\left(B\alpha_i - \arctan\left(B\alpha_i\right)\right)\right)\right)$$

$$\alpha_{Ad} = \delta - \arctan\left(\frac{v_y + \dot{\psi}a}{v_x + \frac{c}{2}}\right)$$

$$\alpha_{As} = \delta - \arctan\left(\frac{v_y + \dot{\psi}a}{v_x - \frac{c}{2}}\right)$$

$$\alpha_{Pd} = -\arctan\left(\frac{v_y - \dot{\psi}b}{v_x + \frac{c}{2}}\right)$$

$$\alpha_{Ps} = -\arctan\left(\frac{v_y - \dot{\psi}b}{v_x - \frac{c}{2}}\right)$$

This system is implicit and has to be soled using a solver (e.g. Newton-Raphson) inside the ODE function. The state vector in the ODE function is:

$$x = \begin{Bmatrix} v_y & \dot{\psi} & \dot{\rho} & X_G & Y_G & \psi & \rho \end{Bmatrix}^T \tag{4.24}$$

$$\dot{x} = \begin{Bmatrix} \dot{v}_y & \ddot{\psi} & \ddot{\rho} & \dot{X}_G & \dot{Y}_G & \dot{\psi} & \dot{\rho} \end{Bmatrix}^T \tag{4.25}$$

Remember the relations:

$$\begin{aligned} \dot{v_y} &= a_y - v_x\dot{\psi} \\ \dot{X}_G &= v_x\cos\psi - v_y\sin\psi \\ \dot{Y}_G &= v_x\sin\psi + v_y\cos\psi \end{aligned} \tag{4.26}$$

### 4.1.3 Wind Forces and Moments on the Vehicle

The wind forces and moments terms in the equations of the Section 4.1.2 are computed in the CFD simulations in the point P visible in Figure 4.2 (apart from the lift forces that are divided on front and rear axles) as explained in *OpenFOAM User Guide* and imported in MATLAB.

It is important to underline that in CFD simulations the vehicle motion is assumed to be straight. This is obviously not true in reality and the purpose of this vehicle dynamics model is exactly to simulate a realistic response to the wind. Being the forces computed on a vehicle that is going straight could take to an underestimation or overestimation of the real forces acting on the vehicle. For this reason in Section 5.2 a study of the influence of different yaw angles on the aerodynamic coefficients has been reported.

For what concerns the moving mesh CFD simulations, since the vehicle goes straight on the $x$ direction and the wind is assumed to flow from the negative to the positive $y$ direction, the wind yaw angles could be computed as:

$$\alpha = \arctan\frac{U_W}{v_x} \tag{4.27}$$

For a more general discussion, as depicted in Figure 4.3, if the wind velocity $\overrightarrow{U}$ is assumed to have a $y$ component only and the vehicle speed $\overrightarrow{V}$ is written with its two components:

$$\overrightarrow{U} = U_x\overrightarrow{i} + U_y\overrightarrow{j} = U\overrightarrow{j} \tag{4.28}$$

$$\overrightarrow{V} = V_x\overrightarrow{i} + V_y\overrightarrow{j} = (v_x\cos\psi - v_y\sin\psi)\overrightarrow{i} + (v_x\sin\psi + v_y\cos\psi)\overrightarrow{j} \tag{4.29}$$

the relative wind speed would be:

$$\overrightarrow{V_r} = \overrightarrow{U} - \overrightarrow{V} = V_{rx}\overrightarrow{i} + V_{ry}\overrightarrow{j} = v_{rx}\overrightarrow{i_L} + v_{ry}\overrightarrow{j_L} \tag{4.30}$$

and the wind yaw angle would be given by:

$$\alpha = \psi + \varphi = \arctan\frac{V_{ry}}{-V_{rx}} \tag{4.31}$$

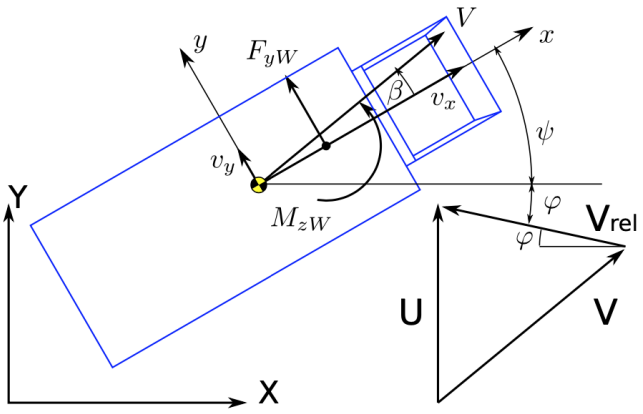


**Figure 4.3:** Scheme of the relative wind speed

### 4.1.4 Driver Model

The vehicle is able to follow a reference path that in these simulations is a straight line (since the purpose is to keep the lane while responding to the crosswind) thanks to a path follower PD control like in Figure 4.4. The tuning of this model has been based on the path follower model presented in [57]. The driver applies a steering angle defined as:

$$\delta = k_p(Y_{ref} - Y_{obs}) + k_d(0 - \dot{Y}_{obs}) \tag{4.32}$$

where $Y_{ref}$ is the $Y$ coordinate of reference path evaluated at vehicle $X$ position plus a prevision length $L$. This prevision length depends on the speed of the vehicle and on the reaction time of the driver:

$$L = t_{react}v_x \tag{4.33}$$

$Y_{obs}$ is instead the observed vehicle position which is the actual $Y$ coordinate of the c.o.g of the vehicle plus the mentioned prevision length:

$$\begin{aligned} Y_{ref} &= Y_{ref}(X_G + L\cos\psi) \\ Y_{obs} &= Y_G + L\sin\psi) \\ \dot{Y}_{obs} &= \dot{Y}_G + L\dot{\psi}\cos\psi) \end{aligned} \tag{4.34}$$

$k_p$ and $k_d$ are the proportional and derivative gain of the controller. The resulting steering angle is then saturated to $\pm 45°$ to avoid excessive and unrealistic values.

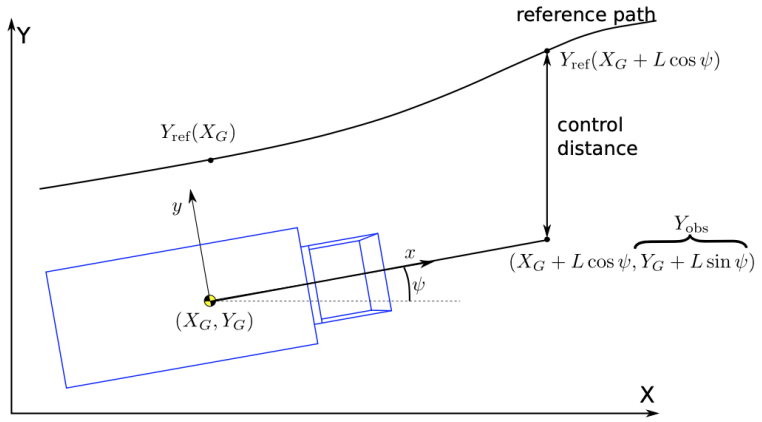


**Figure 4.4:** Scheme of the driver path follower model

## 4.2 DrivAer (Car)

For the vehicle dynamics model of the car, the same approach as in Section 4.1 has been used. However, since there is no lumped mass on the car, the evaluation of the mass distribution is much easier. Apart from this simplification, the model is the same described in Section 4.1. As for the truck, to write the equations of motion, it is fundamental to state which forces are acting on the vehicle, but since they have been widely described in Section 4.1, only the actual dimensions of the considered model are reported in Figure 4.5 while the parameters of the model are listed in Table 4.2.

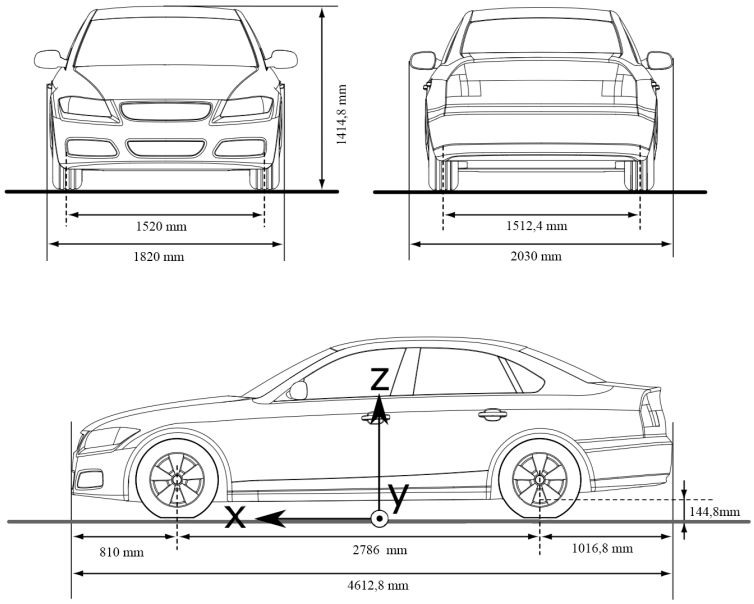


**Figure 4.5:** Dimensions of the considered car model

| parameter | description | unit | value |
|---|---|---|---|
| $a$ | c.o.g./front axle distance | m | $p/2$ |
| $A_f$ | vehicle frontal surface | $m^2$ | 2.165 |
| $b$ | c.o.g./rear axle distance | m | $p-a$ |
| $c$ | vehicle front and rear track | m | 1.52 |
| $J_x$ | vehicle body moment of inertia along $x$ axis | $kgm^2$ | 340 |
| $J_z$ | vehicle body moment of inertia along $z$ axis | $kgm^2$ | 2200 |
| $m_a$ | front axle unsprung mass | kg | 60 |
| $m$ | vehicle body sprung mass | kg | 1470 |
| $m_p$ | rear axle unsprung mass | kg | 60 |
| $p$ | vehicle wheelbase | m | 2.786 |
| $Rr$ | wheels roll radius | m | 0.3 |
| $x_P$ | wind application point x-distance from c.o.g. | m | $p/2-b$ |
| $z_G$ | height of body c.o.g. from ground | m | 0.5 |
| $z_P$ | wind application point coordinate on $z$ axis | m | 0.5 |
| $z_R$ | roll centre height from ground | m | 0.15 |

**Table 4.2:** Car dynamics model parameters

## 4.3 Vehicle Rollover Condition and Safety Indices

Being the purpose of this work the study of the effectiveness of wind-break fences against strong crosswind, it is necessary to introduce the quantities that will be used to evaluate the safety condition during the simulations. The first two quantities will be particularly useful for the Truck that due to its high lateral surface suffers from big roll angles and lateral load transfers. These last may cause unsafe driving conditions or even a rollover condition. The rollover condition during the simulation could be easily evaluate looking at the normal load on each tyre: if this becomes 0 on one tyre, the vehicle starts to roll over. In other words, the rollover condition could be evaluated for each tyre as the load on that tyre over the static load of that tyre:

$$\frac{F_{zi}}{F_{zi0}} \leqslant 0 \tag{4.35}$$

However, as perfectly explained in 'Numerical–experimental approach for evaluating cross-wind aerodynamic effects on heavy vehicles' [15], there are many situations in which the rollover condition is not yet verified, but the vehicle is highly unstable and so in a very dangerous situation. For this reason Cheli et al. [15] define an index that takes into account the load transfer of the axle, thus giving information on the rollover risk for the vehicle; if the threshold value is exceeded, the vehicle starts to be in danger. The so-called safety index condition is defined as:

$$\eta = \frac{F_{zAs} - F_{zAd}}{F_{zA}} \leqslant 0,9 \tag{4.36}$$

$$\eta = \frac{F_{zPs} - F_{zPd}}{F_{zP}} \leqslant 0,9 \tag{4.37}$$

It has to be noticed that this condition is not a sufficient condition for the complete rollover of the vehicle, but points out a very critical and potentially dangerous situation for the vehicle stability [15].

The third index, concerns the lateral displacement, since there are cases in which the vehicle does not roll over, but could anyway be dangerous for other vehicles due to a big lateral displacement, that in some cases could even take to an undesired lane change. Being the minimum width of a highway lane in Italy equal to 3,5 m [34], the following condition has been defined:

$$\xi = \frac{3,5}{2} - \left(Y + \frac{w}{2}\right) \geqslant 0{,}2\,\mathrm{m} \tag{4.38}$$

where $\xi$ is the lateral safety limit, $Y$ is the lateral position of the vehicle w.r.t. the lane centre and $w$ is the width of the vehicle.

# Chapter 5

# Numerical Simulations and Results

## 5.1 Moving Mesh Simulations

In the next sections, all the results obtained with the moving mesh simulations will be reported. The numerical setup of the case study as well as the geometries of the two vehicles and two kinds of fences tested have been reported in Chapter 2.

Four parameters have been investigated for both the vehicles: the presence of the fences, the kind of fences, the wind speed and the vehicle speed. Moreover, for the truck it has been also investigated the weight of the cargo bed and for the car the lane in which it runs.

In this chapter so, after a brief explanation of the logical scheme followed to run all the simulations optimizing the computational time, the influence of the mentioned parameters will be reported. In order to better understand the trajectory graphs of this chapter, it could be very useful to look at Figure 5.1, 5.2 and 5.3. In Figure 5.1 a top overview of the simulated case studies is reported. Performing now a cut on the second and third lanes of Figure 5.1 and then again on the emergency lane, it is possible to obtain what reported in Figure 5.2. Figure 5.3 shows also a side view of the same case, that could help to understand the position of the vehicle w.r.t. the fences. Finally, squeezing the width of the lane and of the vehicle w.r.t. the width of the vehicle, what will be reported in all the trajectory graphs is obtained. This is very useful in order to describe the position of the whole vehicle in the lane just reporting the motion of the c.o.g. of the vehicle. For example if in this graph the blue lane overcomes the dashed white lane, in reality this would mean that the left wheels of the vehicle would overrun the lane.

For the sake of clarity an example that will be discussed in a later paragraph is reported in Figure 5.4. In this picture two different cases are plotted: in blue the trajectory that the vehicle follows without the presence of the fences, in orange the trajectory with the fences. In black the end of the tunnel and of the fences (present only in the second case) are reported.

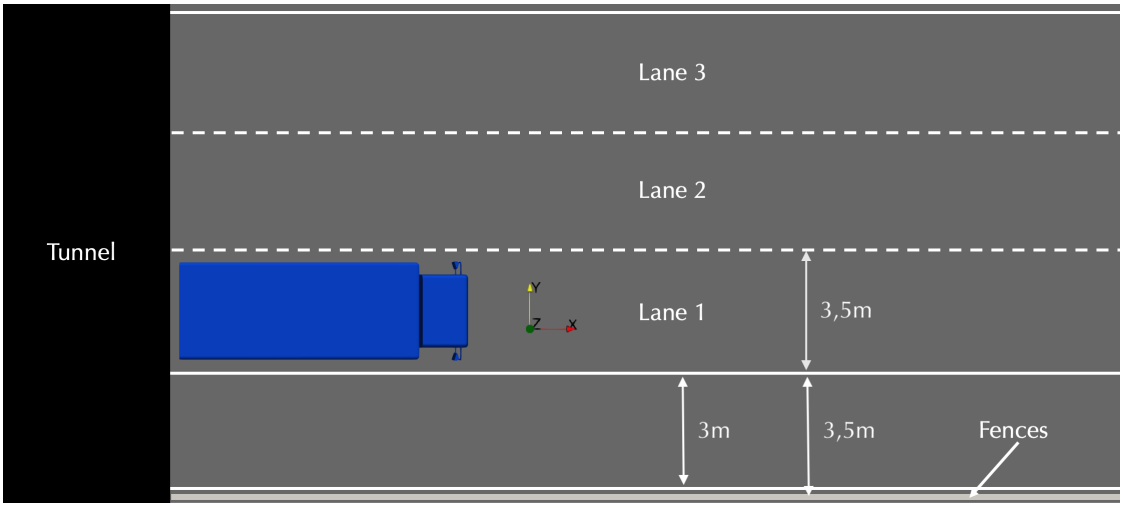


**Figure 5.1:** Top overview of the simulated case studies

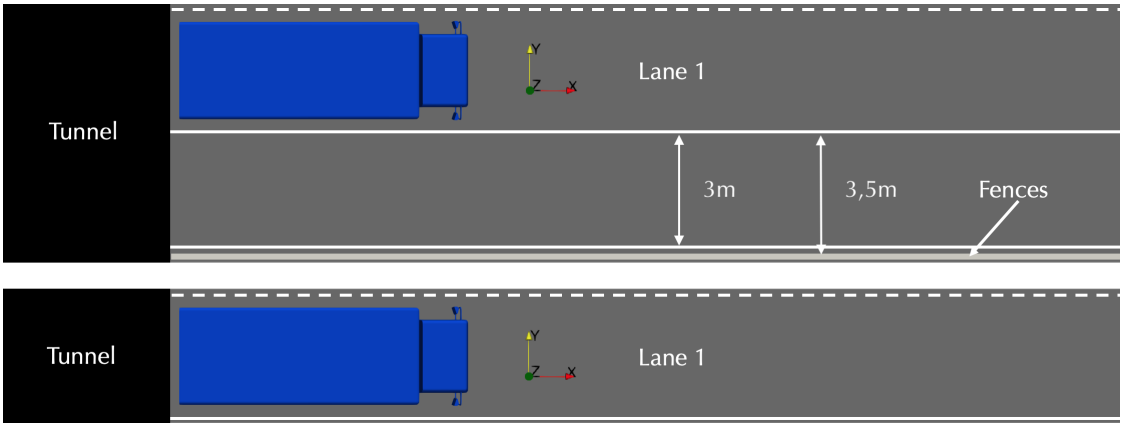


**Figure 5.2:** Some graphical visualization steps starting from Figure 5.1 to ease the comprehension of the trajectory graphs of this chapter

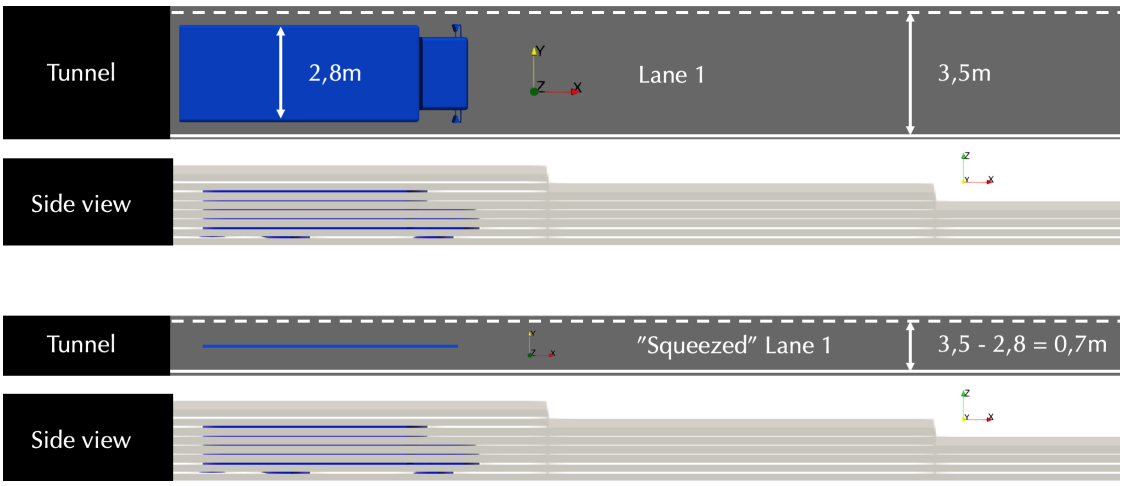


**Figure 5.3:** Some other graphical visualization steps to ease the comprehension of the trajectory graphs of this chapter following the ones of Figure 5.2

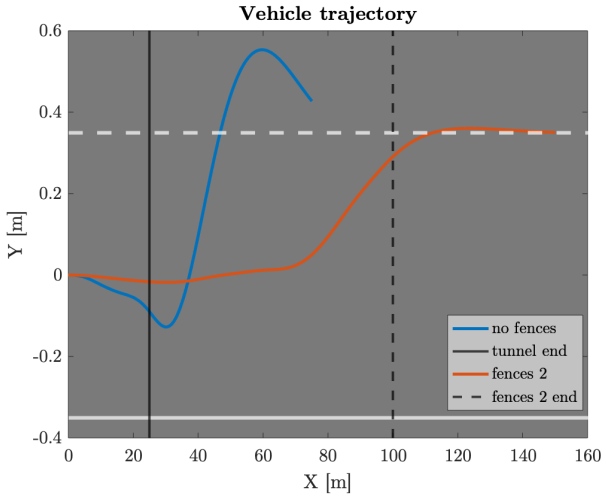


**Figure 5.4:** Example of the trajectory graphs that will be reported in this chapter

### 5.1.1 Influence of the Kind of Fences

In this section the influence of the presence and of the kind of fences will be investigated, keeping the speed of the wind and of the vehicles constant. In addition to these conditions, the weight of the truck and the lane in which the car runs will be kept constant too. Being the wind-break fences the core of this work, this analysis is a fundamental step to assess the effectiveness of these last, comparing the two designed fences with the base case. Keeping all the other parameters constant and changing just the kind of fences is the only way to state clearly if there could be a benefit with the implementation of the designed fences. After this first comparison, in the next sections only the best option identified within the two will be reported and compared with the base case in the plots, while also the other option will be reported in the final table of each section.

#### Truck

As it is easy to imagine, being the truck the vehicle with the greatest side area, it will undergo the greatest aerodynamic loads. If the vehicle is also half-empty, it will generate lower contact forces with the ground, and so it will suffer more from the crosswind. For this reason, it has been decided to test the truck at a condition of $m = 0,5m_{max}$. For what concerns the speed of the wind and of the truck, since their influence will be investigated in the next sections, only the most critical couple of $v_{vehicle}$ and $U_{wind}$ will be reported. These conditions are $v_{vehicle} = 25\,\mathrm{m/s}$ which is a totally reasonable speed for a truck of this kind on a highway and $U_{wind} = 30\,\mathrm{m/s}$ which is a low probability but still realistic very strong wind condition [58].

In Figure 5.5 the trajectory graph (as explained at the beginning of this chapter) with the addition of the lateral safety limit $\xi$ boundaries and a comparison of the safety indices $\eta$ are reported. Looking at the blue lane of the first graph, that is the trajectory of the base case (no fences after the end of the tunnel), it is clear that with such critical conditions of wind speed, the vehicle after an initial little displacement towards the right due to the suction generated by the flow passing

through the space between the truck and the wall of the tunnel at the end of this last, a sudden tremendous displacement of around 0,65 m occurs in just 1 s (from $X = 30$ m to $X = 55$ m, the c.o.g. moves from $Y = -0{,}127$ m to $Y = 0{,}529$ m). This implies that the vehicle invades the contiguous lane in a very low time generating a very dangerous condition that requires great driving skills from the drivers in the other lane to avoid an accident. Moreover, in Figure 5.6 some other information that could help to understand the seriousness of this base case are reported. As clear from the first graph of Figure 5.6, in just one second the driver has to move the steering wheel from $-17{,}5°$ to $28{,}5°$ to keep the lane and this requires a good promptness and a high attention level of the driver.

Moving now to the two other cases, it is clear that the medium size length fences (the so-called fences 1, reported in orange), in this case provide a benefit that is not enough, reducing the maximum displacement from $Y_{basecase} = 0{,}553$ m to $Y_{fences1} = 0{,}471$ m (-14,8%), while the long size length fences (the so-called fences 2, reported in yellow), thanks to the much more smooth increase of the aerodynamic loads, permits to be in a safer condition reducing the maximum displacement from $Y_{basecase} = 0{,}553$ m to $Y_{fences2} = 0{,}362$ m (-34,5%) and stretching the transient time from 1 s (base case) to 3,5 s. It is worth mentioning that due to the critical conditions tested, none of the three cases fulfil the restrictive condition of the lateral safety limit. In Table 5.1 a recap of the maximum displacements for the base case and for the two cases with fences is reported.

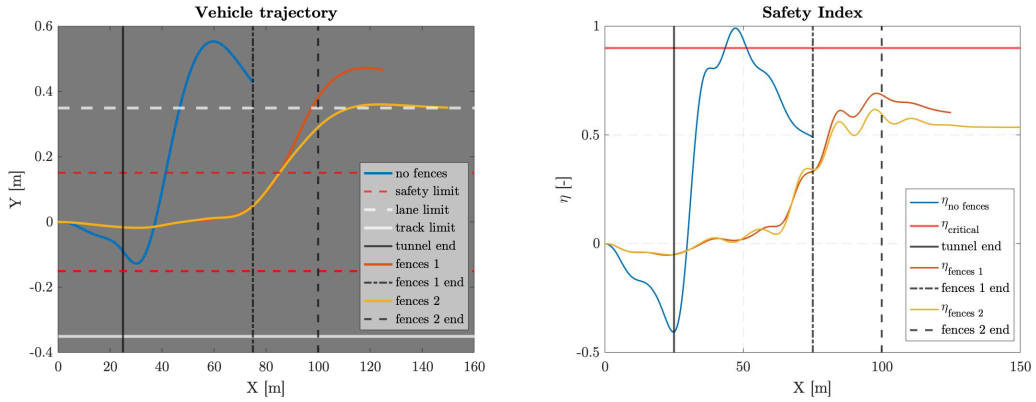


**Figure 5.5:** Trajectory graph (left) and safety index graph (right) of the three cases keeping $v_{vehicle} = 25$ m/s, $U_{wind} = 30$ m/s and $m = 0,5m_{max}$

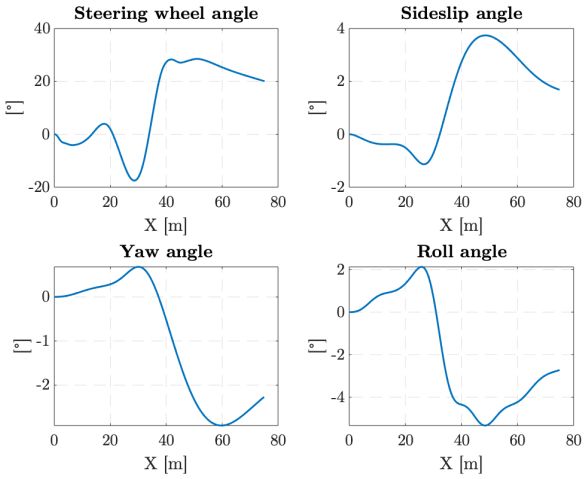


**Figure 5.6:** Some useful parameters of the base case simulation keeping $v_{vehicle} = 25\,\mathrm{m/s}$, $U_{wind} = 30\,\mathrm{m/s}$ and $m = 0,5m_{max}$

An important consideration could be made looking at the two graphs reported in Figure 5.7 in which as an example the wind yaw moment $M_z$ over the longitudinal position of the vehicle is reported for the base case and for the case with the long size fences (fences 2). From these plots it is even more clear how this kind of fences smooths the rising of the aerodynamic loads: the final value is obviously the same, but the transient in the second case is much longer as previously explained. This smoother behaviour of the aerodynamic loads is the reason why the load shifts on the two axles are safer with the fences w.r.t. the base case; this is clear from the second plot of Figure 5.5. One last comment on the safety index plot is that both the kinds of fences are capable to reduce significantly the load shift on the axle lowering this crucial parameter.

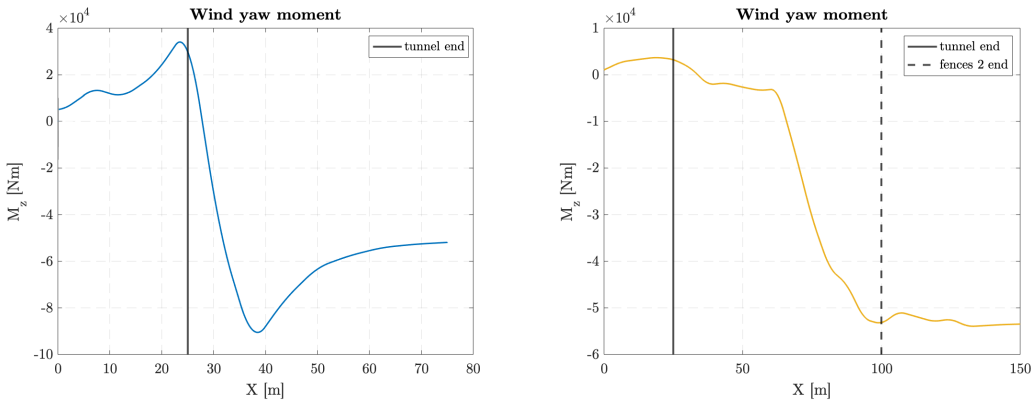


**Figure 5.7:** Wind yaw moment plot of the base case (left) and of the case with the fences 2 (right), keeping $v_{vehicle} = 25\,\mathrm{m/s}$, $U_{wind} = 30\,\mathrm{m/s}$ and $m = 0,5m_{max}$

Once assessed the benefits of the designed fences in these critical conditions for the truck, although these first results seems very promising, it is important to understand the influence of all the other parameters before drawing some conclusions. For this reason Section 6.4 will be dedicated to discuss the results.

| $Y_{basecase}$ $[m]$ | $Y_{fences1}$ $[m]$ | $\Delta$ | $Y_{fences2}$ $[m]$ | $\Delta$ |
|---|---|---|---|---|
| 0,553 | 0,471 | -14,8% | 0,362 | -34,5% |

**Table 5.1:** Maximum lateral displacement keeping $v_{vehicle} = 25\,\text{m/s}$, $U_{wind} = 30\,\text{m/s}$ and $m = 0,5m_{max}$

### DrivAer

Due to the much lower side area w.r.t. the truck, the DrivAer will be subjected to lower aerodynamic loads. For what concerns the speed of the wind and of the vehicle, since their influence will be investigated in the next sections, only the most critical couple of $v_{vehicle}$ and $U_{wind}$ will be reported. These conditions are $v_{vehicle} = 30\,\text{m/s}$ which is a totally reasonable speed for a car on a highway and $U_{wind} = 30\,\text{m/s}$ which is a low probability but still realistic very strong wind condition [58].

In Figure 5.8 the trajectory graph (as explained at the beginning of this chapter) with the addition of the lateral safety limit $\xi$ boundaries is reported. The lane limits are not reported since the displacements are small and they would be less visible enlarging the graph. In this case due to the dynamics of the car the rollover risk is so low that it wouldn't make sense to look at the changes in the safety index graph as done for the truck. As it is possible to notice, also in the base case the vehicle suffers a maximum displacement that is within the boundaries of the lateral safety limit $\xi$. Anyway, some considerations could be made on the three cases at least on the maximum displacements that are: $Y_{basecase} = 0,195\,\text{m}$, $Y_{fences1} = 0,163\,\text{m}$ (-16,4% w.r.t. the base case) and $Y_{fences2} = 0,125\,\text{m}$ (-35,9% w.r.t. the base case). The medium size length fences, whom height in the last section is 1,5 m (the DrivAer is 1,41 m high), give results not so satisfying w.r.t. the base case (thanks to the porosity some minor effects are obtained). On the other hand, the long size length fences, give better results since they have been designed precisely to be optimized also for the car model. In Table 5.2 a recap of the maximum displacements for the base case and for the two cases with fences is reported.

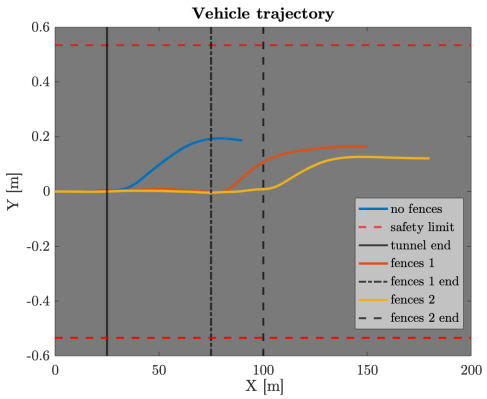


**Figure 5.8:** Trajectory graph of the three cases keeping $v_{vehicle} = 30\,\text{m/s}$, $U_{wind} = 30\,\text{m/s}$ and the vehicle in the first lane of the highway

Before moving to the study of the influence of the other parameters, it is important to remark that as stated ad the beginning of this section, from now on only the best identified option within the two fences, and so fences 2, will be compared with the base case in the plots, but also the other option will be reported in the final table of each section.

| $Y_{basecase}$ $[m]$ | $Y_{fences1}$ $[m]$ | $\Delta$ | $Y_{fences2}$ $[m]$ | $\Delta$ |
|---|---|---|---|---|
| 0,195 | 0,163 | -16,4% | 0,125 | -35,9% |

**Table 5.2:** Maximum lateral displacement keeping $v_{vehicle} = 30\,\mathrm{m/s}$, $U_{wind} = 30\,\mathrm{m/s}$ and the vehicle in the first lane of the highway

### 5.1.2 Influence of the Speed of the Wind

#### Truck

In this section the influence of the speed of the wind is reported. As in the previous section, it has been decided to test the truck at a condition of $m = 0,5m_{max}$. For what concerns the speed of the vehicle, a velocity of $v_{vehicle} = 25\,\mathrm{m/s}$ which is a totally reasonable speed for a truck of this kind on a highway has been set. Two wind conditions have been investigated: $U_{wind} = 25\,\mathrm{m/s}$ and $U_{wind} = 30\,\mathrm{m/s}$, the first is a reasonable strong wind speed, the second as in the previous section is a low probability but still realistic very strong wind condition [58].

In Figure 5.9 the trajectory graphs (as explained at the beginning of this chapter) with the addition of the lateral safety limit $\xi$ boundaries and a comparison of the safety indices $\eta$ are reported. The reduction of the aerodynamic loads, when reducing the wind speed, is linked not only to the module of the speed of the wind itself, but also to the lower yaw angles. It is very interesting to notice in Figure 5.9 that the initial suction of the base case discussed in the previous section for $U_{wind} = 30\,\mathrm{m/s}$ is much lower when $U_{wind} = 25\,\mathrm{m/s}$ and could be easily handled by the driver. This is the reason why the safety index changes less rapidly in this case. Looking now at the two cases with the fences 2 after the tunnel it is interesting to notice that the trend is exactly the same for both cases, with an obvious difference in the maximum lateral displacement $Y$. Also in these cases the fences seem to respond very well to the strong wind, reducing the maximum displacement of -51,1% when $U_{wind} = 25\,\mathrm{m/s}$ and of -34,5% when $U_{wind} = 30\,\mathrm{m/s}$ and reducing significantly the safety index in both cases. In Table 5.3 a recap of the maximum displacements for the base case and for the two cases with fences is reported.

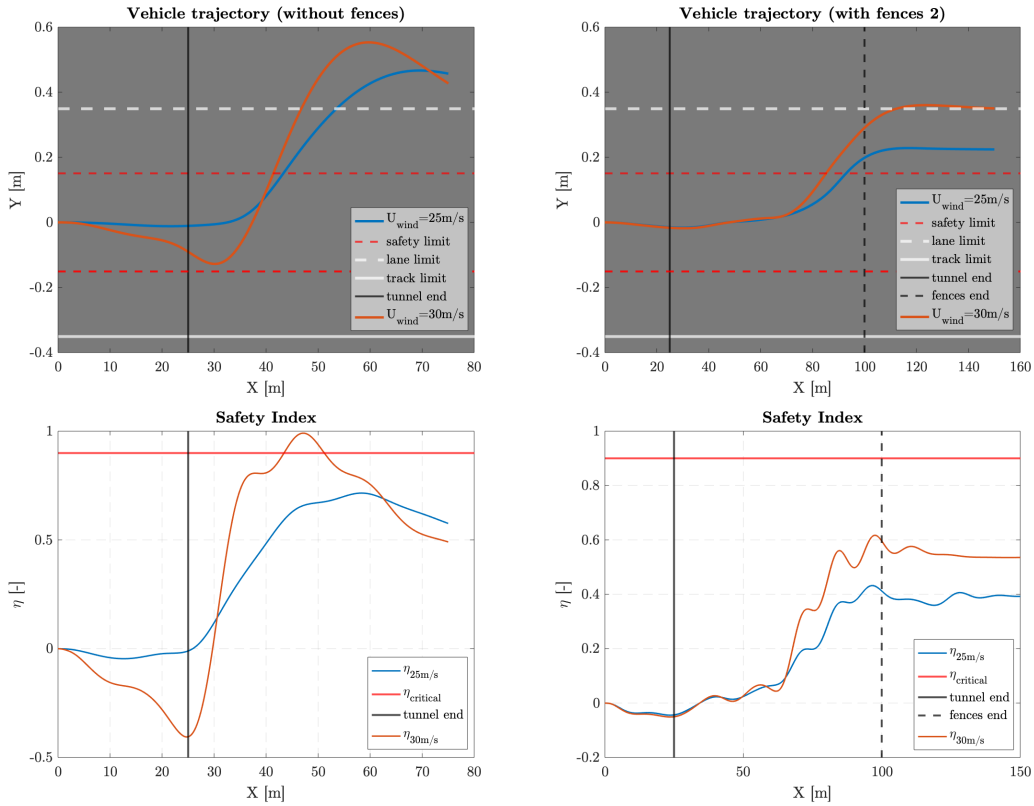


**Figure 5.9:** Trajectory graph of the base case (top left) and of the case with fences 2 (top right) and safety index graph of both the cases (bottom left and right) keeping $v_{vehicle} = 25\,\mathrm{m/s}$ and $m = 0,5m_{max}$

| $U_{wind}$ $[m/s]$ | $Y_{basecase}$ $[m]$ | $Y_{fences1}$ $[m]$ | $\Delta$ | $Y_{fences2}$ $[m]$ | $\Delta$ |
|---|---|---|---|---|---|
| 25 | 0,466 | 0,303 | -35,0% | 0,228 | -51,1% |
| 30 | 0,553 | 0,471 | -14,8% | 0,362 | -34,5% |

**Table 5.3:** Maximum lateral displacement keeping $v_{vehicle} = 25\,\mathrm{m/s}$ and $m = 0,5m_{max}$

### DrivAer

For what concerns the DrivAer the speed of the vehicle has been set to $v_{vehicle} = 30\,\mathrm{m/s}$ which is a totally reasonable speed for a car on a highway. Two wind conditions have been investigated: $U_{wind} = 25\,\mathrm{m/s}$ and $U_{wind} = 30\,\mathrm{m/s}$, the first is a reasonable strong wind speed, the second as in the previous section is a low probability but still realistic very strong wind condition [58].

In Figure 5.10 the trajectory graphs (as explained at the beginning of this chapter) with the addition of the lateral safety limit $\xi$ boundaries are reported. The reduction of the aerodynamic loads, when reducing the wind speed, is linked not only to the module of the speed of the wind itself, but also to the lower yaw angles. For this reason there is an obvious great difference for the two speeds in the base case. Looking now at the two cases with the fences 2 after the tunnel it is interesting to notice that the trend is exactly the same for both cases, with an obvious difference in the maximum lateral displacement $Y$. Also in these cases

the fences seem to respond very well to the strong wind, reducing the maximum displacement of -45,9% when $U_{wind} = 25\,\mathrm{m/s}$ and of -35,9% when $U_{wind} = 30\,\mathrm{m/s}$. In Table 5.4 a recap of the maximum displacements for the base case and for the two cases with fences is reported.

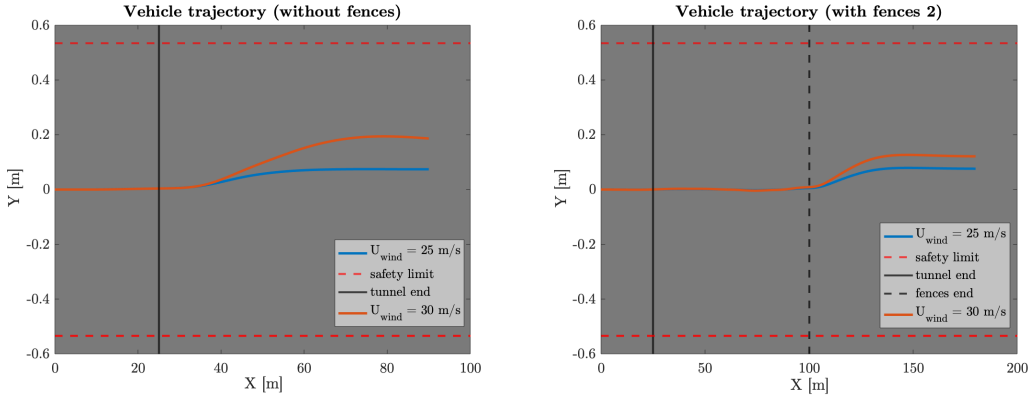


**Figure 5.10:** Trajectory graph of the base case (left) and of the case with fences 2 (right) keeping $v_{vehicle} = 30\,\mathrm{m/s}$

| $U_{wind}\ [m/s]$ | $Y_{basecase}\ [m]$ | $Y_{fences1}\ [m]$ | $\Delta$ | $Y_{fences2}\ [m]$ | $\Delta$ |
|---|---|---|---|---|---|
| 25 | 0,074 | 0,064 | -13,5% | 0,040 | -45,9% |
| 30 | 0,195 | 0,163 | -16,4% | 0,125 | -35,9% |

**Table 5.4:** Maximum lateral displacement keeping $v_{vehicle} = 30\,\mathrm{m/s}$

### 5.1.3 Influence of the Speed of the Vehicle

#### Truck

In this section the influence of the speed of the vehicle is reported. As in the previous section, it has been decided to test the truck at a condition of $m = 0,5m_{max}$. For what concerns the speed of the wind, a velocity of $U_{wind} = 30\,\mathrm{m/s}$ which is a low probability but still realistic very strong wind condition, has been set [58]. Two vehicle speeds have been investigated: $v_{vehicle} = 22{,}5\,\mathrm{m/s}$ and $v_{vehicle} = 25\,\mathrm{m/s}$, the first is a quite low speed, the second is a normal speed for a truck on a highway. The purpose of this investigation is to understand if reducing the speed limits when a strong crosswind occurs could make sense or not.

In Figure 5.11 the trajectory graphs (as explained at the beginning of this chapter) with the addition of the lateral safety limit $\xi$ boundaries and a comparison of the safety indices $\eta$ are reported. The reduction of the aerodynamic loads, when reducing the speed of the vehicle, is linked only to the module of the speed of the wind itself, because in this case the yaw angles are higher. Also in this case in Figure 5.9 it could be noticed that the initial suction of the base case discussed in the previous section for $v_{vehicle} = 25\,\mathrm{m/s}$, could be easily handled by the driver when $v_{vehicle} = 22{,}5\,\mathrm{m/s}$ thanks to the lower speed and so the slower action required. This is the reason why the safety index changes less rapidly in this case. Looking now at the two cases with the fences 2 after the tunnel it is interesting to notice that the

trend is once again exactly the same for both cases, with an obvious difference in the maximum lateral displacement $Y$. Also in these cases the fences seem to respond very well to the strong wind, reducing the maximum displacement of -30,1% when $v_{vehicle} = 22{,}5\,\mathrm{m/s}$ and of -34,5% when $v_{vehicle} = 25\,\mathrm{m/s}$ and reducing significantly the safety index in both cases. In Table 5.5 a recap of the maximum displacements for the base case and for the two cases with fences is reported.

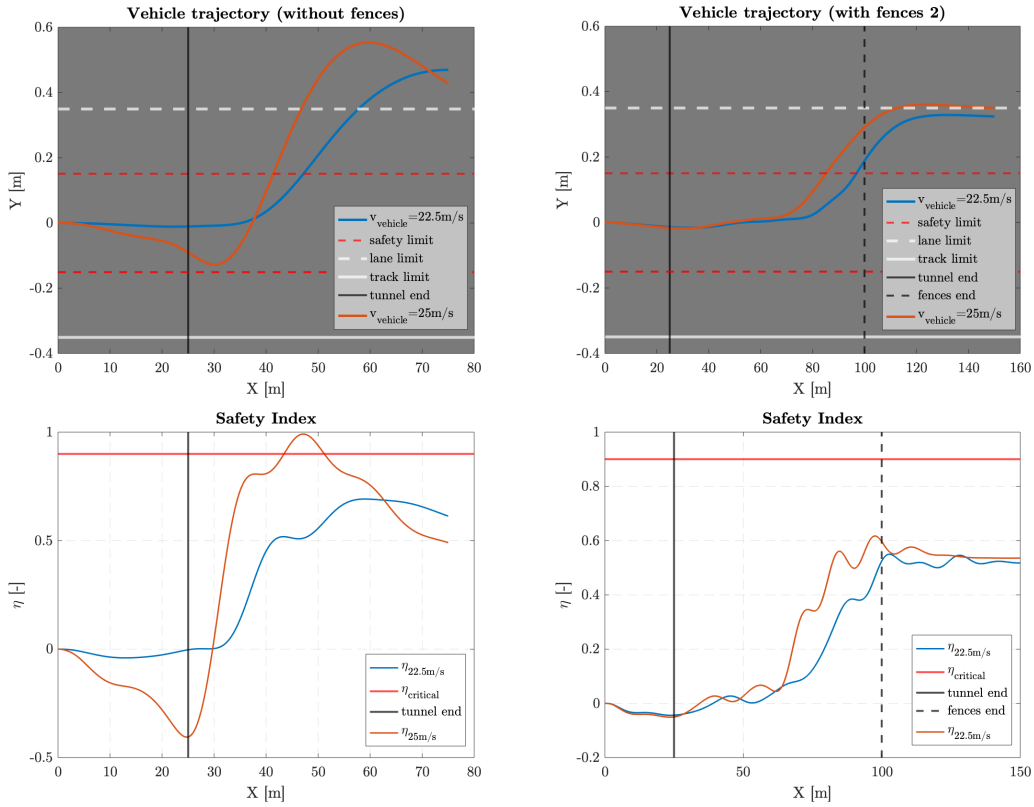


**Figure 5.11:** Trajectory graph of the base case (top left) and of the case with fences 2 (top right) and safety index graph of both the cases (bottom left and right) keeping $U_{wind} = 30\,\mathrm{m/s}$ and $m = 0,5m_{max}$

| $v_{vehicle}\ [m/s]$ | $Y_{basecase}\ [m]$ | $Y_{fences1}\ [m]$ | $\Delta$ | $Y_{fences2}\ [m]$ | $\Delta$ |
|---|---|---|---|---|---|
| 22.5 | 0,469 | 0,451 | -3,8% | 0,328 | -30,1% |
| 25 | 0,553 | 0,471 | -14,8% | 0,362 | -34,5% |

**Table 5.5:** Maximum lateral displacement keeping $U_{wind} = 30\,\mathrm{m/s}$ and $m = 0,5m_{max}$

### DrivAer

For what concerns the DrivAer, as in the previous section, it has been decided to set the speed of the wind to $U_{wind} = 25\,\mathrm{m/s}$ which is a reasonable strong wind speed [58]. Two vehicle speeds have been investigated: $v_{vehicle} = 25\,\mathrm{m/s}$ and $v_{vehicle} = 30\,\mathrm{m/s}$, the first is a quite low speed, the second is a normal speed for a car on a highway. Once again, the purpose of this investigation is to understand if reducing the speed limits when a strong crosswind occurs could make sense or not.

In Figure 5.12 the trajectory graphs (as explained at the beginning of this chapter) with the addition of the lateral safety limit $\xi$ boundaries are reported. The reduction of the aerodynamic loads, when reducing the speed of the vehicle, is linked only to the module of the speed of the wind itself, because in this case the yaw angles are higher. It is interesting to notice that even the two base cases show a quite low maximum lateral displacement $Y$, this is higher when the speed of the vehicle is lower, and this is linked to the higher yaw angles of this case. Looking now at the two cases with the fences 2 after the tunnel it is interesting to notice that the trend is very similar for both cases, and that also in this case the maximum lateral displacement $Y$ is higher when the speed of the vehicle is lower, even if there are almost equal in this case. Also in these cases the fences seem to respond very well to the strong wind, reducing the maximum displacement of -55,3% when $v_{vehicle} = 25\,\mathrm{m/s}$ and of -45,9% when $v_{vehicle} = 30\,\mathrm{m/s}$. In Table 5.6 a recap of the maximum displacements for the base case and for the two cases with fences is reported.

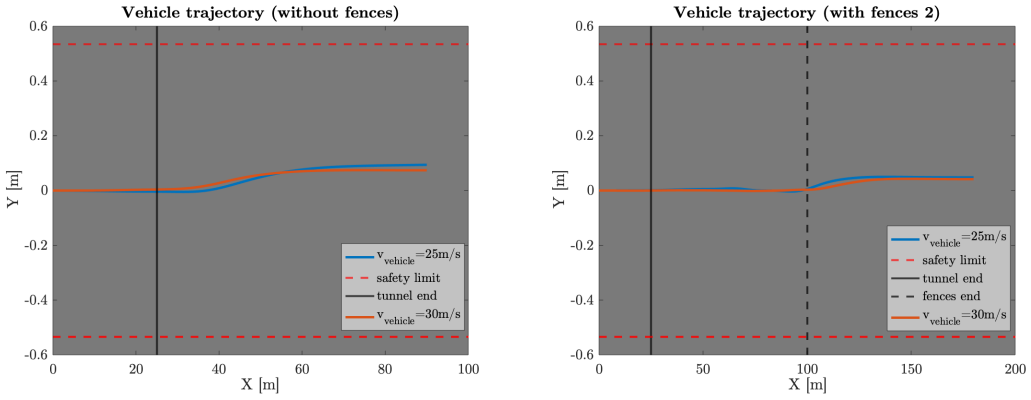


**Figure 5.12:** Trajectory graph of the base case (left) and of the case with fences 2 (right) keeping $U_{wind} = 25\,\mathrm{m/s}$

| $v_{vehicle}\ [m/s]$ | $Y_{basecase}\ [m]$ | $Y_{fences1}\ [m]$ | $\Delta$ | $Y_{fences2}\ [m]$ | $\Delta$ |
|---|---|---|---|---|---|
| 25 | 0,094 | 0,072 | -23,4% | 0,042 | -55,3% |
| 30 | 0,074 | 0,064 | -13,5% | 0,040 | -45,9% |

**Table 5.6:** Maximum lateral displacement keeping $U_{wind} = 25\,\mathrm{m/s}$

### 5.1.4 Influence of the Weight of the Truck

In this section the influence of the weight of the truck is reported. For this reason, it has been decided to test the truck at a condition of $m = 0,5m_{max}$, $m = 0,75m_{max}$ and $m = m_{max}$. This because a truck of the N2 category of Italian regulations could be loaded from 3,5 t to 12 t, which is a wide range and have a big impact on vehicle dynamics [59]. For what concerns the speed of the wind, a velocity of $U_{wind} = 30\,\mathrm{m/s}$ which is a low probability but still realistic very strong wind condition, has been set [58], while regarding the speed of the vehicle it has been decided to test $v_{vehicle} = 25\,\mathrm{m/s}$, a normal speed for a truck on a highway.

The purpose of this investigation is to understand the impact of the weight of the truck on the response of the vehicle to crosswind.

In Figure 5.13 the trajectory graphs (as explained at the beginning of this chapter) with the addition of the lateral safety limit $\xi$ boundaries and a comparison of the safety indices $\eta$ are reported. In Figure 5.14 the load on the front right wheel over the static load for the base cases varying the weight of the truck and load on the four wheels over the static load when $m = m_{max}$ are reported. These last two pictures could help to understand what happens in the trajectory graph of the base cases: increasing the load, the inertia of the vehicle grows, taking to lower displacements with the same aerodynamic loads. This is the reason why when $m = 0,75m_{max}$, the vehicle does not invade the contiguous lane, while when $m = 0,5m_{max}$ this happens. However, increasing the load, means also lifting the total centre of gravity of the vehicle increasing so its roll instability; this is exactly what happens moving from $m = 0,75m_{max}$ to $m = m_{max}$: the vehicle that didn't fulfil the safety index requirements also in the other two cases, in this case when $X = 41{,}6\,\text{m}$ rolls over. This is perfectly visible in Figure 5.14: when $m = m_{max}$ at $X = 41{,}6\,\text{m}$, the load on the front right wheel becomes 0. Looking now to the other graph, it is interesting to notice how the load on the wheels changes from the beginning in which the vehicle undergoes the suction due to the air flow between the vehicle and the wall of the tunnel to the end in which the driver is trying to turn right to face the crosswind.

Looking now at the two cases with the fences 2 after the tunnel, in this case it is very interesting to see how the situation changes completely: in the three cases the vehicle moves from a situation of danger (that could lead to catastrophic accidents sometimes) to a much more safe situation as perfectly visible comparing the two safety index plots of Figure 5.13. Moreover, when the vehicle is fully loaded, despite the critical wind condition, the vehicle not only does not roll over any more, but undergoes a maximum lateral displacement $Y$ that is very close to the lateral safety limit and so perfectly acceptable.

This demonstrates perfectly that there are many cases in which the danger is due more to the sudden rise of the aerodynamic loads rather than to the steady state value of the wind which can be, instead, managed by a driver.

As for the other cases, in Table 5.7 a recap of the maximum displacements for the base case and for the two cases with fences is reported.

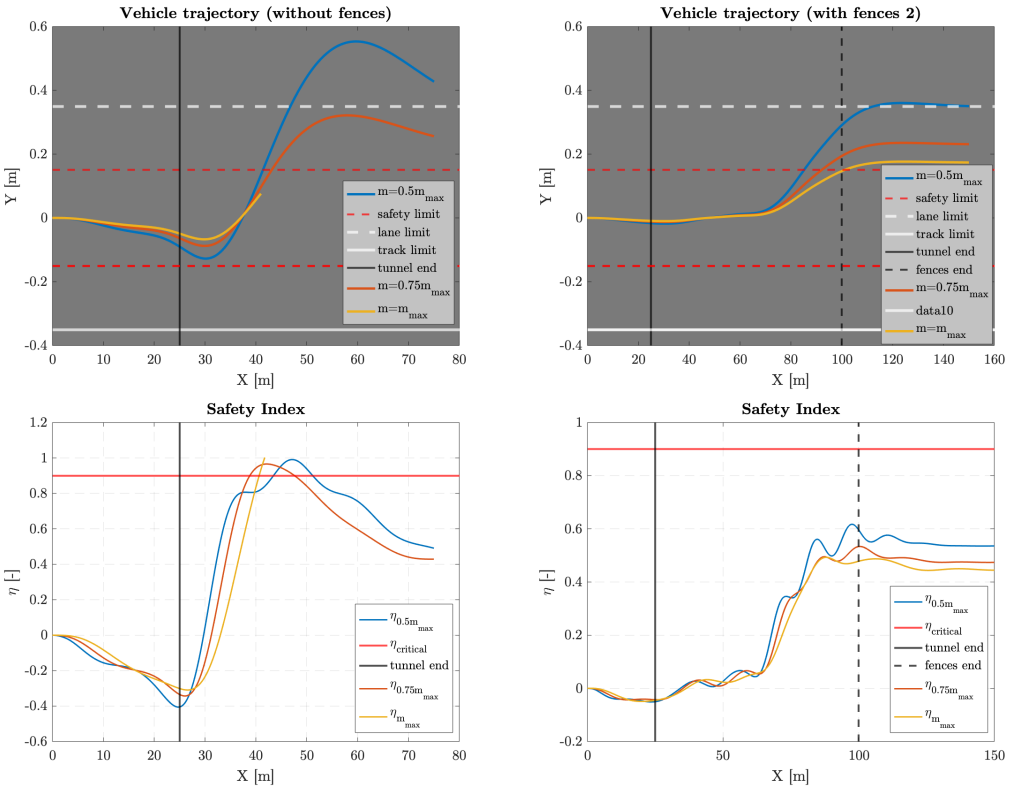


**Figure 5.13:** Trajectory graph of the base cases (top left) and of the case with fences 2 (top right) and safety index graph of both the cases (bottom left and right) keeping $v_{vehicle} = 25\,\mathrm{m/s}$ and $U_{wind} = 30\,\mathrm{m/s}$

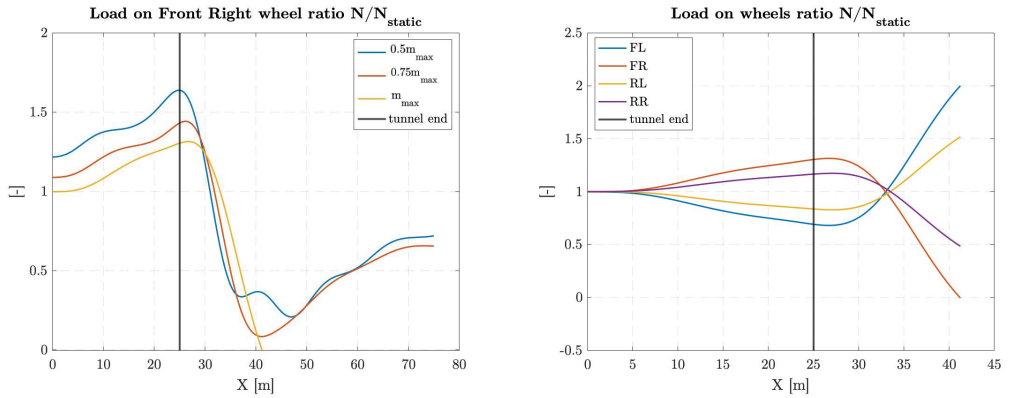


**Figure 5.14:** Load on the front right wheel over the static load for the base case varying the weight of the truck (left) and load on the four wheels over the static load when $m = m_{max}$ (right) keeping $v_{vehicle} = 25\,\mathrm{m/s}$ and $U_{wind} = 30\,\mathrm{m/s}$

| $m$ | $Y_{basecase}\ [m]$ | $Y_{fences1}\ [m]$ | $\Delta$ | $Y_{fences2}\ [m]$ | $\Delta$ |
|---|---|---|---|---|---|
| $0,5m_{max}$ | 0,553 | 0,471 | -14,8% | 0,362 | -34,5% |
| $0,75m_{max}$ | 0,321 | 0,286 | -10,9% | 0,235 | -26,8% |
| $m_{max}$ | rollover | 0,209 | - | 0,176 | - |

**Table 5.7:** Maximum lateral displacement keeping $v_{vehicle} = 25\,\mathrm{m/s}$ and $U_{wind} = 30\,\mathrm{m/s}$

### 5.1.5 Influence of the Lane in which the Car Runs

In this section the influence of the lane in which the car runs is reported. The aim of this study is to understand if there could be any benefit from protecting the vehicle from crosswind with fences even if this last is running in the second lane and so farther w.r.t. the tests that have been conducted up to now. This would be a more realistic scenario for a car running on a highway. For what concerns the speed of the wind, a velocity of $U_{wind} = 30\,\mathrm{m/s}$ which is a low probability but still realistic very strong wind condition, has been set [58], while regarding the speed of the vehicle it has been decided to test $v_{vehicle} = 30\,\mathrm{m/s}$, a normal speed for a car on a highway.

In Figure 5.15 the trajectory graphs (as explained at the beginning of this chapter) with the addition of the lateral safety limit $\xi$ boundaries are reported; obviously in order to compare the results, the trajectory in the second lane has been shifted to the first just for a matter of visualization. What is interesting to notice from the comparison of the two lanes with the fences is that when the vehicle is in the second lane, the maximum lateral displacement $Y$ is lower than when the vehicle is in the first lane. This has been widely investigated, and seems linked to the low pressure zone visible in Figure 5.16 that due to the small height of the DrivAer model, is just above the edge of the vehicle when this last is in the first lane.

As for the other cases, in Table 5.7 a recap of the maximum displacements for the base case and for the two cases with fences is reported. In this case the reduction moves from -35,9% when the vehicle is in the first lane to -49,2% when is in the second.

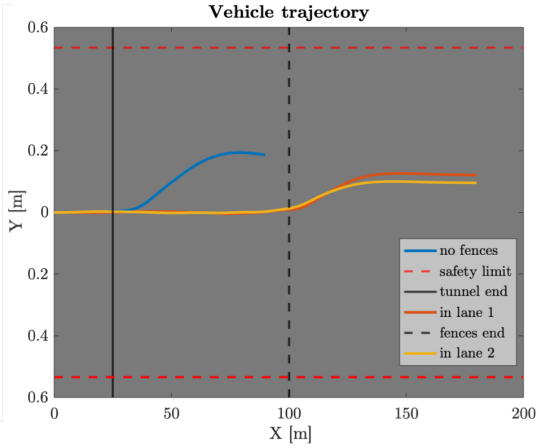


**Figure 5.15:** Trajectory graph to compare the base case with the case with fences 2 in two different situations: the car running in the first and in the second lane keeping $v_{vehicle} = 30\,\mathrm{m/s}$ and $U_{wind} = 30\,\mathrm{m/s}$

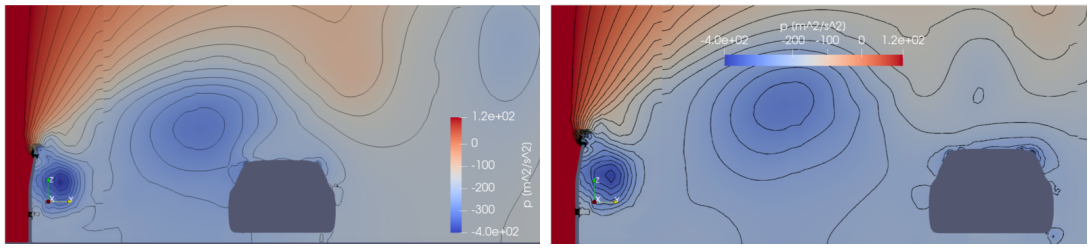


**Figure 5.16:** Pressure contours in the middle of the car of the two cases with fences 2: the car running in the first (left) and in the second lane (right) keeping $v_{vehicle} = 30\,\mathrm{m/s}$ and $U_{wind} = 30\,\mathrm{m/s}$

| lane | $Y_{basecase}$ | $Y_{fences2}$ | $\Delta$ |
|---|---|---|---|
| 1 | 0,195 | 0,125 | -35,9% |
| 2 | 0,195 | 0,099 | -49,2% |

**Table 5.8:** Maximum lateral displacement keeping $v_{vehicle} = 30\,\mathrm{m/s}$ and $U_{wind} = 30\,\mathrm{m/s}$

## 5.2 Static Mesh Simulations

In this chapter, all the results obtained with the static mesh simulations will be reported. The numerical setup as well as the geometries of the two vehicles and two kinds of fences tested have been reported in Chapter 2. As already mentioned, one of the main limits of the moving mesh simulations of this study is that the vehicles during the simulations move straight. Apart from the longitudinal motion, the position of the vehicle in terms of yaw angle does not change during the CFD simulations. For this reason, it has been deemed important to state if this means an underestimation or an overestimation of the aerodynamic loads during the simulations studying the influence of yaw angles on the aerodynamic coefficients. This study has been made with a more "classical" CFD approach (i.e. with a static mesh simulation) w.r.t. the other studies of this work. In the next two sections so the influence of yaw angles on the aerodynamic coefficients of the two vehicles will be reported. These results will be then discussed in Section 6.4.

### 5.2.1 Truck

In Figure 5.17, the aerodynamic coefficients over the yaw angles for the truck model are reported. In order to be consistent with the two reference works for this analysis reported in Figure 5.18 and 5.19 the frontal area of the model has been used as a reference for the drag coefficient calculation, while the lateral surface area has been used as a reference for the others aerodynamic coefficients. It is important to notice that while in this work the yaw angle tested have been from 0° to 60°, in the other two mentioned works they have been from 0° to 90°. The obtained results match really well what previously showed by Cheli et al. [13] (obtained with wind tunnel simulations) and Tagliavia Ramírez [2] (with CFD simulations).

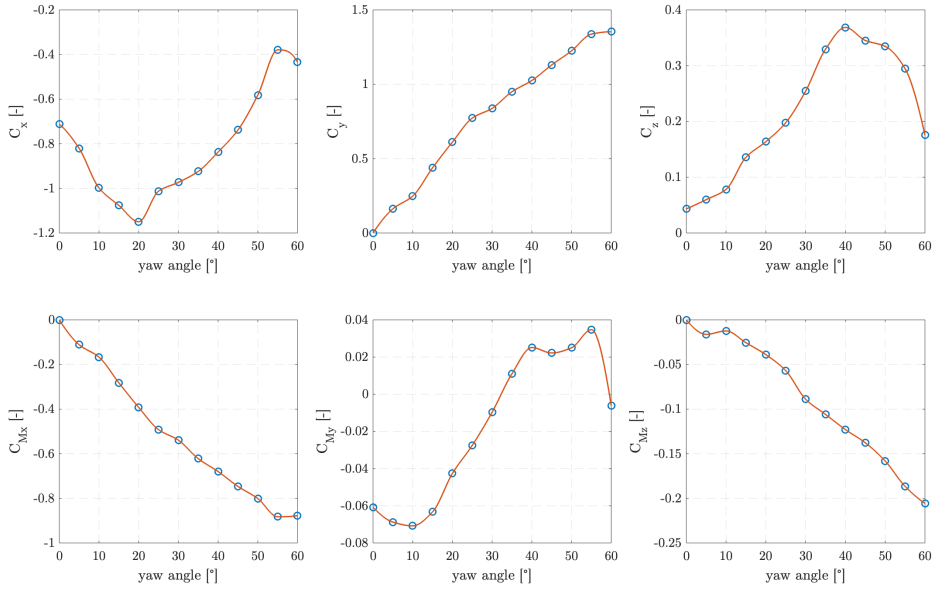


**Figure 5.17:** Aerodynamic coefficients over yaw angles from 0° to 60° for the Truck model

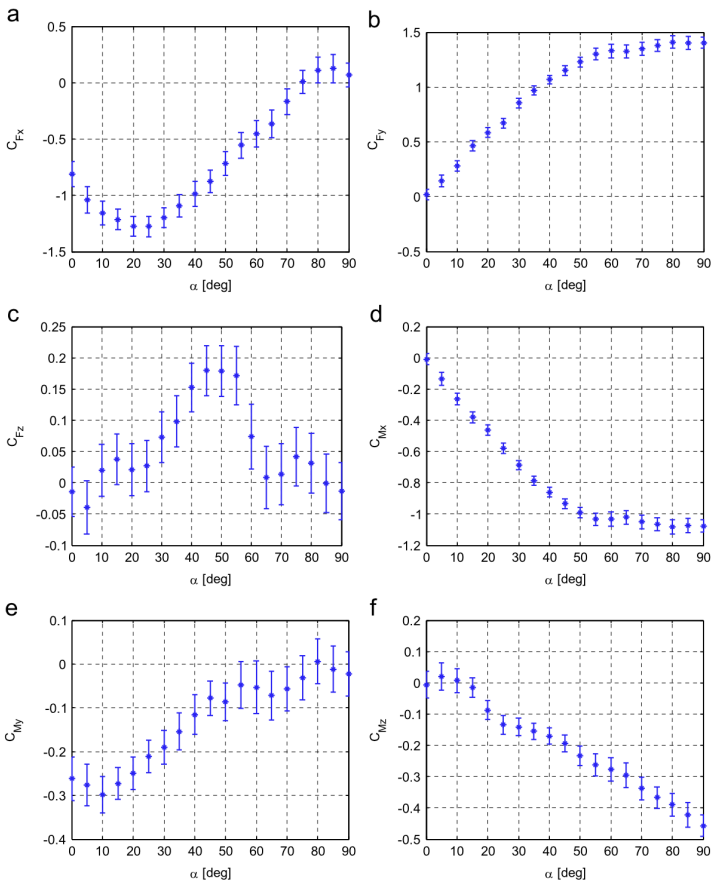


**Figure 5.18:** Aerodynamic coefficients over yaw angles from 0° to 90° taken from 'Wind tunnel tests on heavy road vehicles: Cross wind induced loads—Part 1'[13]

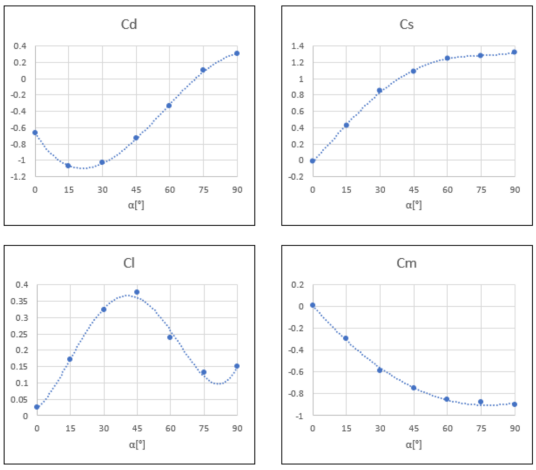


**Figure 5.19:** Aerodynamic coefficients over yaw angles from 0° to 90° taken from 'Study of aerodynamic behavior of different types of vehicle behind windbreak fences under crosswind'[2]

### 5.2.2 DrivAer

In Figure 5.20, the aerodynamic coefficients over the yaw angles for the DrivAer model are reported. Since no other similar studies have been found in the scientific literature, particular attention has been put when running the simulations. In particular, the simulations at 30° and 35° have been run several times in order to be sure that the discontinuities in the coefficients were due to some characteristics of the model (for example the side mirrors of the car) and not to numerical errors. The results reported in Figure 5.20 are the one obtained with the numerical setup explained in Chapter 2.

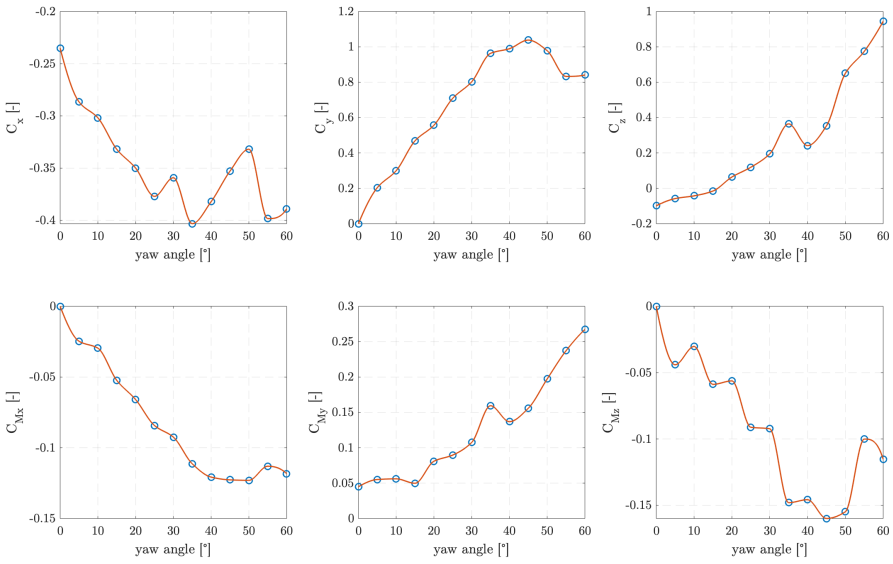


**Figure 5.20:** Aerodynamic coefficients over yaw angles from 0° to 60° for the DrivAer model

# Chapter 6

# Driving Simulator Experiments

In this chapter, the preliminary experiments conducted in the DiM400 dynamic driving simulator recently installed at Politecnico di Milano are reported [60]. These experiments would have never been possible without the support of Prof. Stefano Melzi, Prof. Edoardo Sabbioni, Eng. Antonio Cioffi and Eng. Fabio Semeraro to whom goes a special thanks. I gratefully acknowledge the supervisor of this work Prof. Paolo Schito and the co-supervisor Prof. Michele Vignati for the great opportunity.

The aim of these experiments has been to understand if there could be a good correlation between the results coming from the CFD and vehicle dynamics model simulations reported in Chapter 5 and the results of some simulations conducted on the DiM400 driving simulator keeping the setup as much as possible similar to the previous experiments. Moreover, some other experiments with a realistic wind profile have been conducted and will be reported as a preliminary analysis on some possible applications of the crosswind problem to the dynamic simulator.

## 6.1 The Dim400 Simulator

As reported on the VI-Grade website, the DiM400 dynamic driving simulator (visible in Figure 6.1), is a system consisting of a real cockpit as well as a large panoramic screen that reproduces a virtual scenario, simulating a realistic driving experience. In addition, the driver is immersed in a vibro-acoustic environment that resembles reality. When executing commands to the vehicle, the driver receives the same feedback that he would receive when driving a real car. In the cockpit the driver is subjected to exactly the same forces as in the real driving experience, thanks to the simulator's movements and the integrated active systems of the seat and seatbelts.

From a technical point of view, the simulator works with a 14 d.o.f. vehicle dynamics model provided by the VI-CarRealTime software and a driver in the loop. It is possible to build external Matlab/Simulink models and implement them in the simulator. The 14 d.o.f. vehicle dynamics model is just the basis of the complex model that is set in the driving simulator, that can be modified with some lookup tables. For this application some modifications (e.g. the position of the c.o.g. of the vehicle) have been made to the Compact Car model already present in

the simulator in order to match as much as possible the parameters presented in Chapter 4.

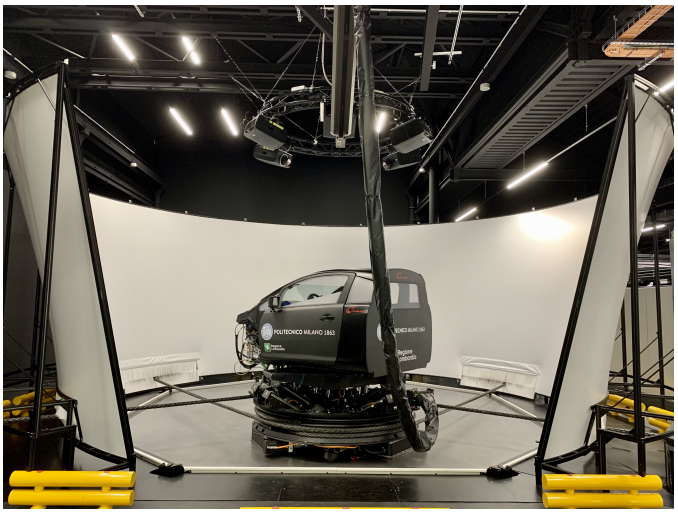

**Figure 6.1:** An overview of the DiM400 dynamic driving simulator

## 6.2 Experimental Setup

For the purpose of this study, a Matlab/Simulink model has been implemented in the loop in order to have a real-time application of the aerodynamic loads acting on the vehicle while running. The inputs of the model are: the absolute yaw angle and the two speed components of the running vehicle (to compute the relative wind yaw angle and velocity), a trigger for the start of the wind gust and the two components of the wind profile (to be loaded before the simulation). If necessary, also a spatial wind speed profile could be loaded, but in this case also the two components of the vehicle position would be needed as an input. The model gives as an output the aerodynamic loads in a specified point, that are then moved to the point of application of the external forces defined by VI-CarRealTime. The aerodynamic loads out of the model are computed with some lookup tables containing the aerodynamic coefficients for different yaw angles presented in Section 5.2.

For what concerns the wind profile, it has been chosen to use realistic random two-dimensional wind profiles as described in Argentini et al. [61]. As an example, in Figure 6.2 the two components of one of the tested wind profiles are reported.

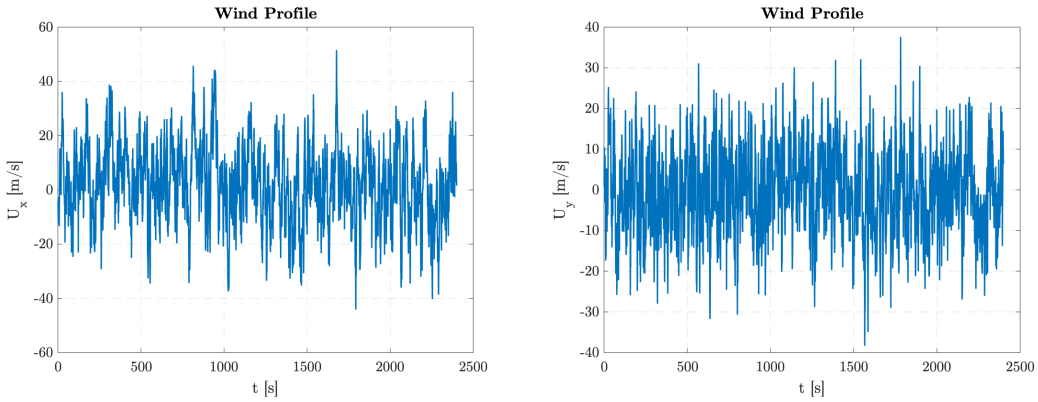


**Figure 6.2:** Longitudinal and transversal component time histories of the turbulent wind used for the driving simulator experiments

Two kinds of simulations have been run: a base case similar to the one presented in Chapter 5 and a more realistic case. The first one has been a simple lane keeping manoeuvre with just one wind peak (of $U_{wind} = 25\,\mathrm{m/s}$ and $U_{wind} = 30\,\mathrm{m/s}$) keeping the speed of the vehicle as much as possible near to $v_{vehicle} = 30\,\mathrm{m/s}$; these tests have been thought to investigate the correlation with the results presented in Chapter 5. The second kind of simulation that has been made is a long run under a realistic wind profile in which two manoeuvres have been tested: a lane keeping and some lane changes. The aim of these last cases has been to investigate some possible experiments that could be done in future and to experience a realistic driving feeling under a strong crosswind.

## 6.3 Results

### 6.3.1 Base Case

In this section, the two base case simulations will be reported. As already mentioned, these tests have been thought to investigate the correlation with the results presented in Chapter 5 and in particular with the ones reported in Figure 6.3.

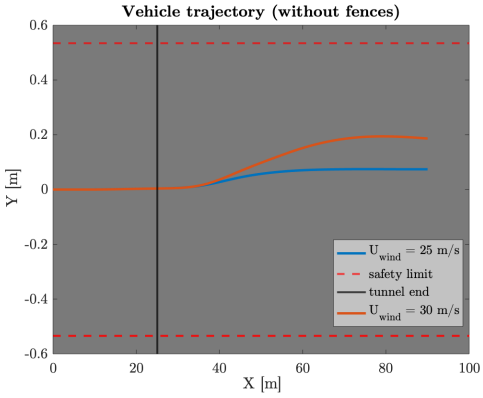


**Figure 6.3:** Trajectory graph of the base case of Chapter 5 keeping $v_{vehicle} = 30\,\mathrm{m/s}$

The trajectory graph of the base case of Chapter 5, reported in Figure 6.3 has been obtained keeping $v_{vehicle} = 30\,\mathrm{m/s}$ and varying the speed of the wind from $U_{wind} = 25\,\mathrm{m/s}$ to $U_{wind} = 30\,\mathrm{m/s}$. This setup has been the reference for the experiments reported in Figure 6.4 and 6.5. Obviously being involved a real driver, there is a slight variation in the speed of the vehicle due to the difficulty to keep a perfectly constant speed under crosswind. The driver could not know the moment in which the wind arises and this should make the response as much as possible realistic. This is very interesting thinking about a possible usage of the simulator for the tuning of driver models in future applications, however this has not been possible for this study. In Table 6.1 a comparison of the results obtained is reported: in both the cases, the results of the simulations of Chapter 5 are slightly smaller than the one obtained with the driving simulator, suggesting that there could be a little difference in the contact forces between vehicle and road or that the driver model has a higher promptness w.r.t. a real driver. Another difference is that the real driver completely adjust the trajectory after almost 75 m, while the driver model needs 60 m. Anyway, it is interesting to notice that the trend is very similar. Obviously many other simulation comparisons would be needed to assess the reliability of these results, but this preliminary study seems to be very promising for future researches on this topic.

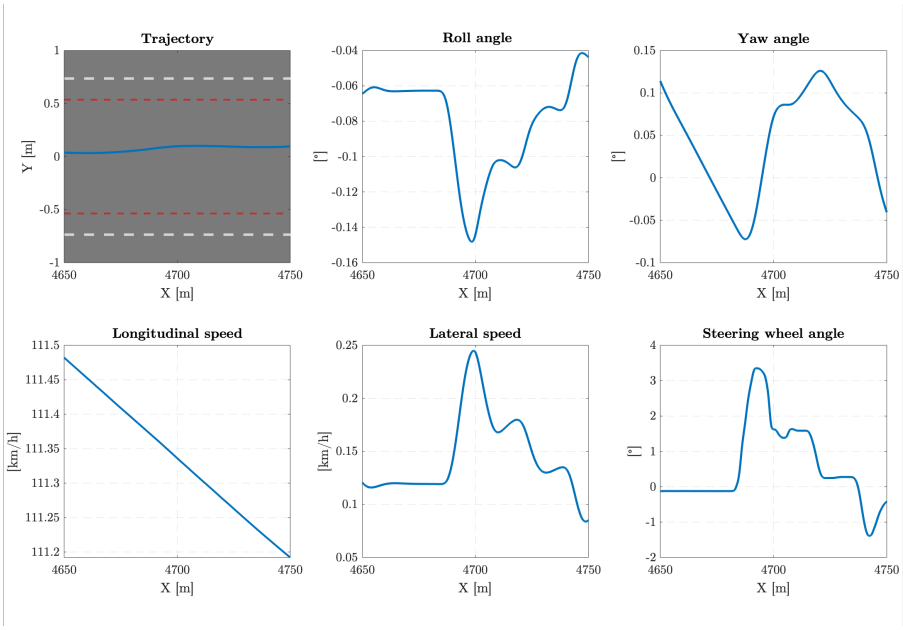


**Figure 6.4:** Results of the base case simulation keeping $v_{vehicle} = 30\,\mathrm{m/s}$ and $U_{wind} = 25\,\mathrm{m/s}$

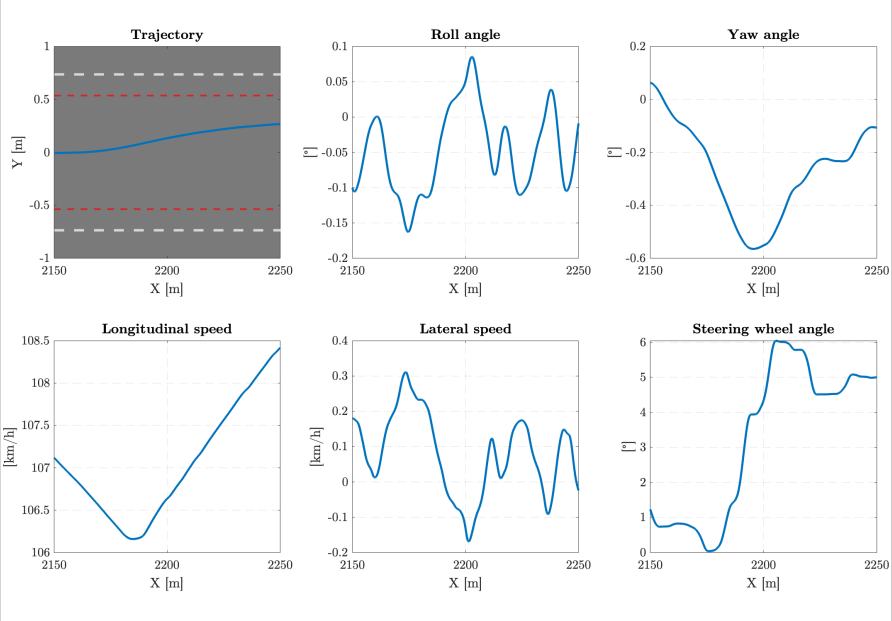


**Figure 6.5:** Results of the base case simulation keeping $v_{vehicle} = 30\,\mathrm{m/s}$ and $U_{wind} = 30\,\mathrm{m/s}$

| $U_{wind}\ [m/s]$ | $Y_{simulations}\ [m]$ | $Y_{DiM400}\ [m]$ |
|---|---|---|
| 25 | 0,074 | 0,102 |
| 30 | 0,195 | 0,231 |

**Table 6.1:** A comparison between the maximum lateral displacement obtained in the simulations reported in Chapter 5 and the ones obtained with the driving simulator keeping $v_{vehicle} = 30\,\mathrm{m/s}$

### 6.3.2 Realistic Scenario Case

In this section, two realistic scenario simulations will be reported. As already mentioned, the aim of these simulations has been to investigate some possible experiments that could be done in future and to experience a realistic driving feeling under a strong crosswind. Two different kinds of simulations have been performed: the first has been a long run lane keeping manoeuvre under a sudden strong crosswind given by the realistic profile reported in Figure 6.2, while the second has been made of several lane changes under crosswind with a lower intensity wind profile.

Looking at the lane keeping manoeuvre reported in Figure 6.6, it is clear the beginning and the end of the wind gust. Even if the lateral displacement never overcomes 0,3 m, there is a feeling of danger while driving the vehicle that is due to the rapid roll angle changes. In this case the DiM400 simulator seems to represent very well the motion of a real vehicle under this kind of wind gust. This simulation demonstrates once again the importance of studying the effects of crosswind on road vehicles even when these last are not affected as much as high-sided lorries and trucks by the wind.

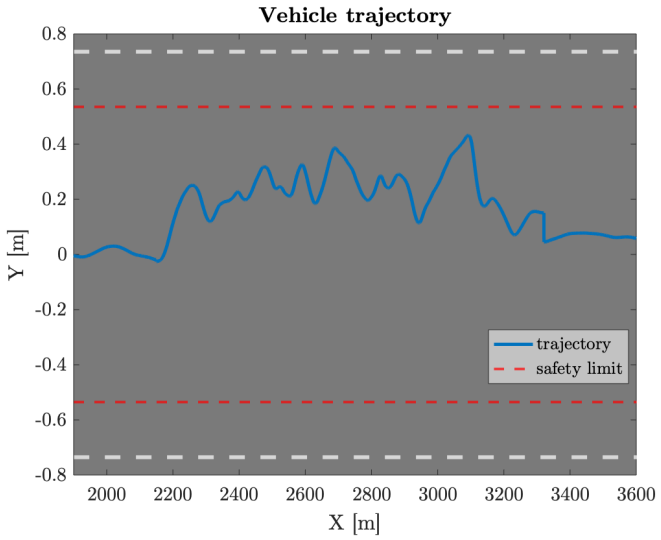


**Figure 6.6:** A lane keeping manoeuvre under crosswind

The second simulation, reported in Figure 6.7 shows the results of some lane changes manoeuvres under crosswind whom aim has been to understand the feeling of the driver while doing a normal manoeuvre in such conditions of crosswind. In this case even if the wind profile has been weaker than in the lane keeping manoeuvre, the instability feeling has been much higher. This kind of simulation could be useful to understand the response of the vehicle and of the driver to a dangerous situation in which a fast lane change would be needed to avoid an accident while there is a strong crosswind.

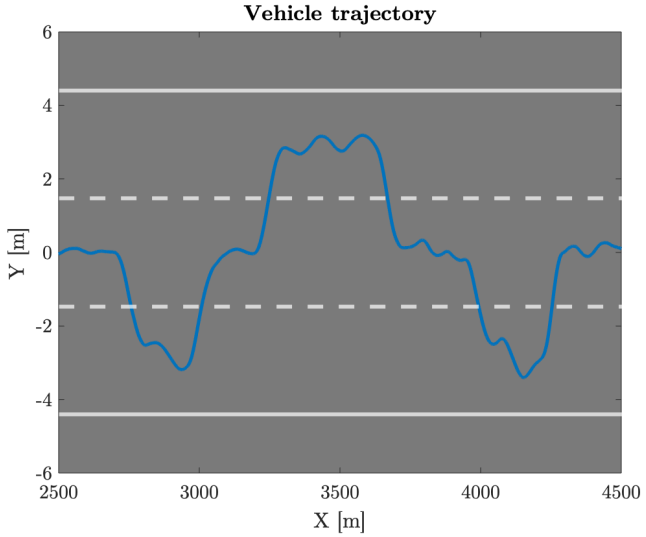


**Figure 6.7:** Some lane change manoeuvres under crosswind

As an example, in Figure 6.8, a section of the roll over longitudinal position graph of the lane changes simulation is reported. Apart from the feeling of being in danger due to the roll angle changes, in both the simulations a tendency of the driver to initially slow down the vehicle has been noticed; this is clearly visible in

Figure 6.9. After this first slowing down, due to the smaller value of the speed of the vehicle, the relative wind yaw angle increases and so the feeling is of a worsening of the situation; for this reason the driver starts to increase the speed once again feeling safer (once again this is clear observing Figure 6.9). This suggests how the feeling to be in danger influences the driver behaviour and could be worth to be studied in future.

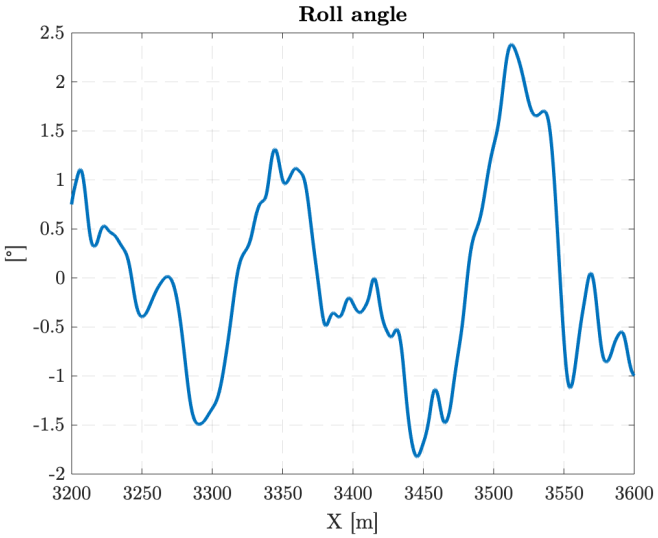


**Figure 6.8:** An example of the rapid roll changes under crosswind

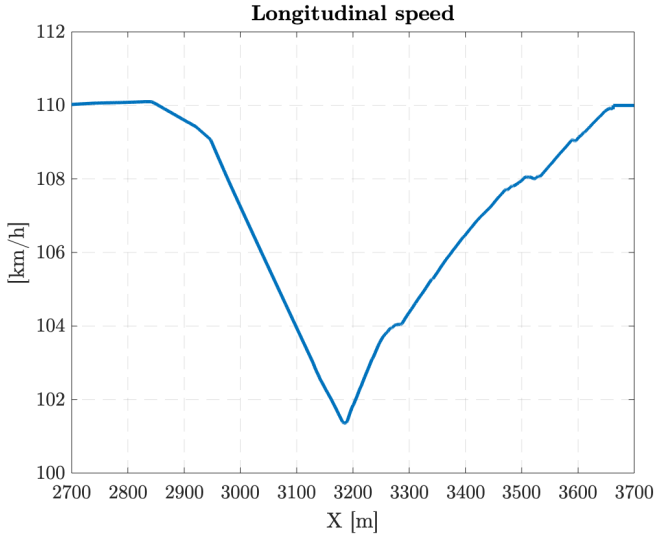


**Figure 6.9:** Speed profile during the lane changes simulation

# Conclusions

## 6.4 A Discussion on the Results

In this work, the effectiveness of two designed wind-break fences on a sudden strong crosswind has been investigated. For the purpose of these investigations, CFD models have been developed and validated by means of wind tunnel tests and a robust vehicle dynamics model has been developed as well.

In this section, all the results presented in Chapter 5 will be discussed in order to draw some conclusions about this work. As reported in the introduction to this work, following the hypothesis that there are many situations in which the danger of crosswind is due to the sudden rise of the aerodynamic loads, the goal of this work has been to design and test ad hoc wind-break fences in order to mitigate the effects of a sudden strong crosswind on two kinds of vehicles (a truck model and a car model). These fences have been designed to stretch the transient time of rise of the aerodynamic loads so as to reduce the instability of the vehicles due to low transient time. In other words, the hypothesis to be demonstrated has been that there are many cases in which the danger is due more to the sudden rise of the aerodynamic loads rather than to the steady state value of the wind which can be, instead, managed by a driver. This hypothesis has found a demonstration in Section 5.1.4 in which a clear switch from a dangerous situation to a much more safe situation is obtained by means of the presence of the designed wind-break fences.

In this work, as reported in Section 2.1, two different kinds of fences have been designed. The main differences between the two are the total length and the height of the final section, that in the case of the long size length fences (the so-called "fences 2") have been optimized in order to be more effective on a car whom height is clearly lower than a truck. All the tests reported in all the tables in the end of each section of Chapter 5 have shown in fact a higher effectiveness of the longer model w.r.t. the shorter one (the so-called "fences 1").

Many parameters have been investigated in order to understand the effects on the defined safety indices and on the maximum lateral displacement. Different wind speed conditions take to very different scenarios, that in some cases could be catastrophic. In Section 5.1.2, for both the vehicles two strong wind conditions have been tested keeping a normal speed for the vehicles on a highway. In particular both the vehicles have been tested for $U_{wind} = 25\,\mathrm{m/s}$ and $U_{wind} = 30\,\mathrm{m/s}$ keeping a speed of $v_{vehicle} = 25\,\mathrm{m/s}$ for the truck and $v_{vehicle} = 30\,\mathrm{m/s}$ for the car. The very dangerous situations for both the base cases of the truck, have been perfectly mitigated by the presence of the fences, while the car even if never in such dangerous

situations has anyway great benefits due to the presence of the fences.

For what concerns the reduction of the speed of the vehicle, as expectable, takes to some minor improvements linked to the slower actions required to the driver (see Section 5.1.3), but takes also to the increasing of the relative wind yaw angle that could lead to dangerous situations. For this reason some other investigations would be necessary to state if a reduction of the speed limits in strong crosswind conditions could be a possible solution, in particular for high-sided vehicles which suffers more these conditions.

Another key parameter tested has been the weight of the truck: a truck of the N2 category of Italian regulations could be loaded from 3,5 t to 12 t, which is a wide range and have a big impact on vehicle dynamics [59]. For this reason, it has been decided to test the truck at a condition of $m = 0,5m_{max}$, $m = 0,75m_{max}$ and $m = m_{max}$. These tests show the great variability of the dynamic response of this kind of vehicle to the variation of its cargo bed load. Of course Section 5.1.4 gives a clear demonstration of the hypothesis behind this thesis as explained at the beginning of this chapter, but takes also to some important considerations to be taken into account when analysing these simulations. These considerations are linked to the variability on the response of the vehicle due to the combination of all the investigated parameters (and many others not investigated in this work) and will be discussed in Section 6.5.

For what concerns the car, since it has been deemed more realistic that a car runs on the central line w.r.t. a truck that in general runs on the first line of a highway, also this possibility has been tested. What it has been found out is that due to the lower height of the car w.r.t. the truck, and to the low pressure zones that hit the upper edge of the car, the response of the vehicle is better when it is in the second lane w.r.t. the first lane. This is an important result since would mean that a car that normally runs on that lane could safely continue its run without any problem.

Summing up the results, both the fences models have shown a great effectiveness on the truck model, reducing the maximum lateral displacement of -14,8% and -34,5% respectively in the most critical case ($v_{vehicle} = 25\,\mathrm{m/s}$, $U_{wind} = 30\,\mathrm{m/s}$ and $m = 0,5m_{max}$). Similar results have been obtained for the car model (even if this last resulted to be much less affected by crosswind), with a reduction of -16,4% and -35,9%. The key result has been obtained studying the influence of the weight of the truck: increasing this last, also the roll instability of the truck increases. For this reason some tests have been done keeping $v_{vehicle} = 25\,\mathrm{m/s}$ and $U_{wind} = 30\,\mathrm{m/s}$, for $m = 0,5m_{max}$, $m = 0,75m_{max}$ and $m = m_{max}$. When no fences are placed at the end of the tunnel, the truck undergoes a tremendous lateral displacement (invading the contiguous lane) when $m = 0,5m_{max}$, and rolls over when $m = m_{max}$. Both the fences have shown the capability to reduce significantly the lateral displacement (avoiding the lane limit overlap in the case of the "fences 2") when $m = 0,5m_{max}$ and avoiding the roll over when $m = m_{max}$ decreasing significantly the rollover risk. This has demonstrated that there are many cases in which the danger is due more to the sudden rise of the aerodynamic loads rather than to the steady state value of the wind which can be, instead, managed by a driver.

A study on the variations of the aerodynamic loads with yaw angles has been then conducted in order to understand if due to the straight motion of the vehicle

in the moving mesh simulation there could be some important underestimations or overestimations of the aerodynamic loads. From the vehicle dynamics simulations it has been assessed that the vehicles under the loads imported from the CFD simulations, never overcomes about 50° of yaw angle. For this reason yaw angles between 0° and 60° have been tested. The important observations to be done are for yaw angles between 40° and 50°, that are in the ranges of these simulations. Moreover, the important coefficients to be analysed for the purpose of this study are the side and lift forces coefficients, and the roll and yaw moments coefficients. What it is possible to state from the graphs reported in Section 5.2 is that for the DrivAer model only the lift coefficient changes significantly (leading to an underestimation of lift forces) while for the Truck model side force and roll moment are overestimated while lift forces and yaw moments are underestimated. Anyway as it is clear there are no significant underestimations or overestimations of the forces and this is fundamental to assess the reliability of the results of the moving mesh simulations of this study.

## 6.5 Final Remarks, Possible Improvements and Future Researches

Before analysing all the possible improvements and ideas for future researches on the base of this work, it is important to make some final considerations. In this work the effectiveness of two designed wind-break fences has been studied in a realistic scenario case study. This has been possible thanks to the coupling of validated moving mesh CFD simulations and vehicle dynamics simulations; moreover, the influence of many parameters such as the kind of fences, the speed of the wind and of the vehicle for both the vehicles, the weight of the cargo bed of the truck and the lane in which the car runs has been studied. The two safety indices defined in Section 4.3 as well as the rollover condition has been used to assess the level of danger of all the tests while a study on the maximum lateral displacements has turned out to be fundamental to compare the results. Due to the wide range of results given from the combination of all the studied parameters, for what concerns some tests (e.g. the ones on the weight of the truck) only the most critical cases have been deeply analysed and reported since these last are the more interesting ones for the purpose of this study. This may lead to think that the lateral safety index $\xi$ which is a very restrictive condition due to the width of the truck is quite never fulfilled. However, this is not true since there are cases in which increasing the weight of the vehicle, the condition is perfectly fulfilled. Two examples are reported for completeness in Figure 6.10.

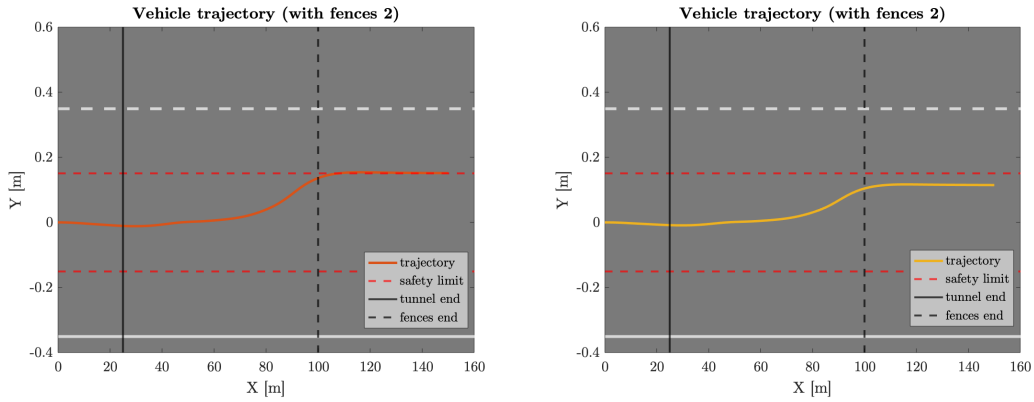


**Figure 6.10:** Trajectory graph of a truck running at $v_{vehicle} = 25\,\mathrm{m/s}$ with $U_{wind} = 25\,\mathrm{m/s}$ behind fences 2 keeping $m = 0,75 m_{max}$ (left) and $m = m_{max}$ (right)

Even though in Chapter 5 and in particular in Section 5.1.4 it has been demonstrated the effectiveness of the designed wind-break fences and in particular of the long size length model (the so-called "fences 2"), there are some possible improvements and ideas for future researches that it is worth mentioning. First of all, among the other parameters that could be tested, the asphalt condition is probably one of the most interesting. As reported in the introduction to this work, the combination of strong wind and other bad weather conditions could lead to critical situations that it is worth studying. In order to conduct a proper analysis, very precise data for the various conditions would be needed in order to fully represent the contact forces with the Pacejka model discussed in Chapter 4 [54] and for this reason due to the difficulty to find proper data in the scientific literature this analysis has not been conducted.

Another possible improvement that at this early state stage would be incomplete due to the need of other data (and so simulations) could be to define the Critical Wind Curves (CWC) like the one defined in 'Numerical–experimental approach for evaluating cross-wind aerodynamic effects on heavy vehicles'[15]. Finding a way to correlate the speed of the wind, the speed of the vehicle, the weight of the vehicle and many other parameters could be the first step to propose an update to the Italian road regulations. This would obviously require also many others data related to other kind of vehicles. For this reason, another important improvement would be to test many other kinds of vehicles (in particular the high-sided ones). By doing these tests also with the presence of the proposed wind-break fences, a final demonstration of the effectiveness of these last could be achieved. This would be a fundamental step before the proposition of the designed fences as a possible solution on the roads to the danger due to the instability of the vehicles for the sudden rise of the aerodynamic loads due to strong crosswind.

Some other improvements whom aim would be to reduce the degree of approximation of the simulations (increasing the computational effort) should be considered. First of all, as explained ad the beginning of Chapter 5, in order to save mesh elements reducing so the computational effort, the tunnel of this work has been replaced with a high wall. This has not been a big approximation due to horizontal wind tested; however, a better reproduction of the tunnel as

well as the other elements of the infrastructure like the guard-rails could be an important improvement. Obviously this would lead to a tremendous increase in the computational effort, but since the cost of computational resources decreases significantly every year, in some years this might not be a problem anymore.

For what concerns the wind model, also in this field an improvement could be made in order to simulate wind gusts that are as much as possible similar to the real ones. This would need the availability of wind gusts measurements, that are not easy to be found in the scientific literature.

Moving to the vehicle dynamics, it could be worth developing a Multi Body model of the vehicles to be studied, in order once again to represent as much as possible the real scenario. However, Multi Body are very complex models and this would increase even more the computational effort; for this reason a more simple model, i.e. a 14 d.o.f. model should be considered. In Chapter 6 some preliminary experiments on the DiM400 dynamic driving simulator have been reported; these experiments are just a starting point for all the possible investigations that could be made with such a powerful tool. As explained in Section 6.1, this simulator is based on a 14 d.o.f. model and for this reason the choice of a 14 d.o.f. model for the simulations of a future study could make the obtained results more comparable to the same experiments conducted on this driving simulator. The first results obtained with the simulator seem very promising, suggesting that a deeper investigation should be conducted with it.

Knowing a priori an approximate trajectory that the vehicle would follow, it could be interesting to implement the predicted trajectory (imposing to the moving mesh a 6 d.o.f. translation) aiming to minimize the yaw and roll angles changes that otherwise would not be taken into account.

Another possible research topic, could be the response of a motorcycle to the strong crosswind and the effectiveness of the designed fences for this kind of vehicle. This would need also a proper vehicle dynamics model and for this reason it has been considered out of the scope of this work.

The addition of more than one vehicle in the CFD simulations even if would increase tremendously the computational effort, it would be a key step to have a complete overview on the crosswind problem and on the effectiveness of the designed fences in a real scenario.

In conclusion, this work and all its challenges, apart taking to many interesting results thanks to whom many useful considerations have been drawn, has most of all been food for thought, pushing continuously the motivation to find new solutions to maximize the results with the available resources.

# Bibliography


[1] Istituto Nazionale di Statistica - ISTAT. *Incidenti Stradali - Anno 2018*. URL: https://www.istat.it/it/archivio/232366 (visited on 11/13/2020) (cit. on pp. xvii, xviii, 1).

[2] Íñigo Andrés Tagliavia Ramírez. 'Study of aerodynamic behavior of different types of vehicle behind windbreak fences under crosswind'. Bachelor's Thesis. Universidad Pontificia Comillas, Politecnico di Milano, 2020 (cit. on pp. xvii, xviii, 1, 5–7, 21–23, 55, 56, 89, 91).

[3] Luigi Salati. 'Aerodynamics of heavy trucks'. PhD thesis. Politecnico di Milano, 2018 (cit. on pp. 1, 4–7, 10, 25, 27).

[4] Gazzetta Ufficiale della Repubblica Italiana. *Regolamento di esecuzione e di attuazione del nuovo codice della strada, Art. 101 (Art. 39 Cod. Str.), Segnale forte vento laterale*. URL: https://www.gazzettaufficiale.it/atto/serie_generale/caricaDettaglioAtto/originario?atto.dataPubblicazioneGazzetta=1992-12-28&atto.codiceRedazionale=092G0531&elenco30giorni=false (visited on 11/15/2020) (cit. on pp. 1, 6).

[5] Thomas Christian Schuetz. *Aerodynamics of Road Vehicles, Fifth Edition*. SAE International, Dec. 2015 (cit. on pp. 2, 3, 18, 19).

[6] W. Hucho. *Aerodynamic of Road Vehicles*. Butterworth-Heinemann, 1990 (cit. on p. 2).

[7] W. Hucho. *Aerodynamik der stumpfen Körper*. Springer, 2012 (cit. on p. 2).

[8] S.R. Ahmed and G. Ramm. 'Some Salient Features of the Time-Averaged Ground Vehicle Wake'. In: *SAE-Paper 840300* (1984) (cit. on pp. 3, 22, 46).

[9] 'Seventh Annual Report of the Aëronautical Society of Great Britain, for the Year 1872'. In: *Annual Reports of the Aeronautical Society of Great Britain* 7 (1872), pp. 6–12 (cit. on pp. 4, 17).

[10] R. J. F. Kieselbach. *Stromlinienautos in Deutschland—Aerodynamik im Pkw-Bau 1900 bis 1945*. Kohlhammer Edition Auto Verkehr, 1982 (cit. on p. 4).

[11] C.J. Baker. 'A simplified analysis of various types of wind-induced road vehicle accidents'. In: *Journal of Wind Engineering and Industrial Aerodynamics* 22.1 (1986), pp. 69–85 (cit. on p. 5).

[12] C.J. Baker and S. Reynolds. 'Wind-induced accidents of road vehicles'. In: *Accident Analysis and Prevention* 24.6 (1992), pp. 559–575 (cit. on p. 5).

[13] F. Cheli et al. 'Wind tunnel tests on heavy road vehicles: Cross wind induced loads—Part 1'. In: *Journal of Wind Engineering and Industrial Aerodynamics* 99.10 (2011), pp. 1000–1010 (cit. on pp. 5, 39, 43, 44, 55, 56, 89, 90).

[14] F. Cheli et al. 'Wind tunnel tests on heavy road vehicles: Cross wind induced loads—Part 2'. In: *Journal of Wind Engineering and Industrial Aerodynamics* 99.10 (2011), pp. 1011–1024 (cit. on p. 5).

[15] F. Cheli et al. 'Numerical–experimental approach for evaluating cross-wind aerodynamic effects on heavy vehicles'. In: *Vehicle System Dynamics* 44.sup1 (2006), pp. 791–804 (cit. on pp. 5, 72, 73, 104).

[16] L. Salati, P. Schito, and F. Cheli. 'Strategies to reduce the risk of side wind induced accident on heavy truck'. In: *Journal of Fluids and Structures* 88 (2019), pp. 331–351 (cit. on p. 5).

[17] L. Salati et al. 'Aerodynamic Study on a Heavy Truck Passing by a Bridge Pylon under Crosswinds Using CFD'. In: *Journal of Bridge Engineering* 23.9 (2018), p. 04018065 (cit. on p. 5).

[18] S. Charuvisit, K. Kimura, and Y. Fujino. 'Experimental and semi-analytical studies on the aerodynamic forces acting on a vehicle passing through the wake of a bridge tower in cross wind'. In: *Journal of Wind Engineering and Industrial Aerodynamics* 92.9 (2004), pp. 749–780 (cit. on p. 5).

[19] Songpol Charuvisit, K Kimura, and Yozo Fujino. 'Effects of wind barrier on a vehicle passing in the wake of a bridge tower in cross wind and its response'. In: *Journal of Wind Engineering and Industrial Aerodynamics - J WIND ENG IND AERODYN* 92 (June 2004), pp. 609–639 (cit. on p. 5).

[20] D. Fintelman et al. 'A numerical investigation of the flow around a motorbike when subjected to crosswinds'. In: *Engineering Applications of Computational Fluid Mechanics* 9.1 (2015), pp. 528–542 (cit. on pp. 5, 6).

[21] Bin Wang et al. 'Crosswind Effect Studies on Road Vehicle Passing by Bridge Tower using Computational Fluid Dynamics'. In: *Engineering Applications of Computational Fluid Mechanics* 8.3 (2014), pp. 330–344 (cit. on pp. 5, 6).

[22] Christoph Strangfeld et al. 'Experimental Study of Baseline Flow Characteristics for the Realistic Car Model DrivAer'. In: (Apr. 2013) (cit. on pp. 5, 50, 53, 54).

[23] Dirk Wieser, Christian Nayeri, and Christian Paschereit. 'Wake Structures and Surface Patterns of the DrivAer Notchback Car Model under Side Wind Conditions'. In: *Energies* 13 (Jan. 2020), p. 320 (cit. on pp. 5, 50).

[24] David Forbes et al. 'A Fully Coupled, 6 Degree-of-Freedom, Aerodynamic and Vehicle Handling Crosswind Simulation using the DrivAer Model'. In: *SAE International Journal of Passenger Cars - Mechanical Systems* 9 (Apr. 2016) (cit. on pp. 5, 6).

[25] Dirk Wieser et al. 'Experimental Comparison of the Aerodynamic Behavior of Fastback and Notchback DrivAer Models'. In: *SAE International Journal of Passenger Cars - Mechanical Systems* 7 (May 2014), pp. 682–691 (cit. on pp. 5, 53, 54).

[26] Chris Baker et al. 'Cross-wind effects on road and rail vehicles'. In: *Vehicle System Dynamics* 47.8 (2009), pp. 983–1022 (cit. on p. 5).

[27] A. Alonso-Estébanez et al. 'Performance analysis of wind fence models when used for truck protection under crosswind through numerical modeling'. In: *Journal of Wind Engineering and Industrial Aerodynamics* 168 (2017), pp. 20–31 (cit. on pp. 5, 6, 23).

[28] D. Rocchi et al. 'A numerical–experimental methodology for simulating the aerodynamic forces acting on a moving vehicle passing through the wake of a bridge tower under cross wind'. In: *Journal of Wind Engineering and Industrial Aerodynamics* 104-106 (2012). 13th International Conference on Wind Engineering, pp. 256–265 (cit. on p. 5).

[29] Edoardo Sabbioni et al. 'Dynamic Response of Vehicle-Driver Couple to the Aerodynamic Loads due to the Crossing of a Bridge Tower Wake'. In: *SAE International Journal of Commercial Vehicles* 5 (July 2012), pp. 83–93 (cit. on p. 5).

[30] Soon-duck Kwon et al. 'Design criteria of wind barriers for traffic. Part 1: Wind barrier performance'. In: *Wind and Structures An International Journal* 14 (Jan. 2011), pp. 55–70 (cit. on p. 5).

[31] Dong Kim et al. 'Design criteria of wind barriers for traffic. Part 2: Decision making process'. In: *Wind and Structures* 14 (Jan. 2011) (cit. on p. 5).

[32] Tommaso Argentini et al. 'Cross-wind effects on a vehicle crossing the wake of a bridge pylon'. In: *Journal of Wind Engineering and Industrial Aerodynamics - J WIND ENG IND AERODYN* 99 (June 2011), pp. 734–740 (cit. on p. 5).

[33] Şemsi Çoşkun et al. 'Experimental investigation of wake flow field and wind comfort characteristics of fractal wind fences'. In: *Journal of Wind Engineering and Industrial Aerodynamics* 168 (2017), pp. 32–47 (cit. on p. 5).

[34] Gazzetta Ufficiale della Repubblica Italiana. *Norme funzionali e geometriche per la costruzione delle strade*. URL: https://www.gazzettaufficiale.it/eli/gu/2002/01/04/3/so/5/sg/pdf (visited on 11/13/2020) (cit. on pp. 6, 31, 73).

[35] Kundu K.P. and Cohen I.M. *Fluid Mechanics*. Academic Press - Elsevier Science (USA), 2002 (cit. on p. 9).

[36] Ferziger J.H. and Perić M. *Computational Methods for Fluid Dynamics*. Springer, 2002 (cit. on pp. 9, 12, 13, 15).

[37] H.K. Versteeg and Malalasekera W. *An Introduction to Computational Fluid Dynamics*. Pearson Prentice Hall, 2007 (cit. on pp. 9–11, 14–17, 19, 28, 29, 34, 35, 52, 54, 56, 58).

[38] The OpenFOAM Foundation. *OpenFOAM User Guide*. 8th ed. The OpenFOAM Foundation Ltd. PO Box 56676, London, W13 3DB, United Kingdom, July 2020 (cit. on pp. 12, 69).

[39] NASA - National Aeronautics and Space Administration. *Beginner's Guide to Wind Tunnels*. URL: https://www.grc.nasa.gov/www/k-12/airplane/shortt.html (visited on 01/18/2021) (cit. on p. 18).

[40] M. Sterling et al. 'A comparison of different methods to evaluate the wind induced forces on a high sided lorry'. In: *Journal of Wind Engineering and Industrial Aerodynamics* 98.1 (2010), pp. 10–20 (cit. on pp. 21, 39, 63).

[41] TUM Department of Mechanical Engineering - Chair of Aerodynamics and Fluid Mechanics. *DrivAer*. URL: https://www.mw.tum.de/en/aer/research-groups/automotive/drivaer/geometry/ (visited on 01/20/2021) (cit. on pp. 22, 46, 53).

[42] CFDHub. *CFDHUB@POLIMI - Computational Fluid Dynamics Laboratory*. URL: https://www.polimi.it/en/scientific-research/research-at-the-politecnico/laboratories/interdepartmental-laboratories/cfdhubpolimi-computational-fluid-dynamic-laboratory/ (visited on 01/23/2021) (cit. on pp. 25, 35).

[43] CINECA. *Italian SuperComputing Resource Allocation - ISCRA*. URL: https://www.hpc.cineca.it/services/iscra (visited on 01/23/2021) (cit. on pp. 25, 35).

[44] A. Marinoni et al. 'Drag and Lift investigations on a 1:4 Car Model'. Unpublished Manuscript. 2019 (cit. on p. 39).

[45] Pelin Yılmazer. 'Design of a Low-Speed Subsonic Portable Wind Tunnel for Educational Purposes'. PhD thesis. Politecnico di Milano, 2019 (cit. on pp. 39, 40).

[46] A. Pope J. B. Barlow W. H. Rae Jr. *Low-speed wind tunnel testing*. Ed. by Wiley-Interscience. Wiley-Interscience, 1999 (cit. on pp. 41, 44).

[47] 'The wind tunnel testing of heavy trucks to reduce fuel consumptions'. In: *SAE Transactions* 91.4 (1982), pp. 4118–4130 (cit. on p. 43).

[48] Technische Universität Berlin. *Institut für StrÖmungsmechanik und Technische Akustik*. URL: http://fd.tu-berlin.de/einrichtungen/windkanaele/growika/ (visited on 01/27/2021) (cit. on pp. 46, 47).

[49] SAE International Surface Vehicle Recommended Practice. 'Guidelines for Aerodynamic Assessment of Medium and Heavy Commercial Ground Vehicles Using Computational Fluid Dynamics'. In: *SAE Standard J2966* (2017) (cit. on pp. 51, 56).

[50] F. Cheli and G. Diana. *Advanced Dynamics of Mechanical Systems*. Springer, Chaml, 2015 (cit. on p. 61).

[51] Massimo Guiggiani. *The Science of Vehicle Dynamics*. Jan. 2014 (cit. on p. 61).

[52] J. E. Bernard, J. E. ABernard, and C. L. Clover. 'Validation of Computer Simulations of Vehicle Dynamics'. In: *SAE Transactions* 103 (1994), pp. 162–170 (cit. on p. 61).

[53] G. Genta and A. Genta. *Road Vehicle Dynamics: Fundamentals Of Modeling And Simulation*. World Scientific Publishing Co Pte Ltd, 2017 (cit. on p. 61).

[54] H.B. Pacejka. *Tire and Vehicle Dynamics*. Springer, 2012 (cit. on pp. 68, 104).

[55] W.F. Milliken and D.L. Milliken. *Race Car Vehicle Dynamics*. SAE International, 1995 (cit. on p. 68).

[56] MATLAB. *version 9.9 (R2020b)*. Natick, Massachusetts: The MathWorks Inc., 2020 (cit. on p. 69).

[57] Christoforos Chatzikomis and Konstantinos Spentzas. 'A path-following driver model with longitudinal and lateral control of vehicle's motion'. In: *Forschung Im Ingenieurwesen-engineering Research - FORSCH INGENIEURW* 73 (Dec. 2009), pp. 257–266 (cit. on p. 70).

[58] Massimiliano Burlando et al. 'Wind climate analysis in complex terrains'. In: *Journal of Wind Engineering and Industrial Aerodynamics* 123 (2013). The Twelfth Italian National Conference on Wind Engineering, IN-VENTO-2012, Venezia, Italy, October 7th–10th 2012, pp. 349–362 (cit. on pp. 77, 80–85, 88).

[59] Gazzetta Ufficiale della Repubblica Italiana. *Art. 39 Cod. Str., Classificazione dei veicolo*. URL: http://www.aci.it/i-servizi/normative/codice-della-strada/titolo-iii-dei-veicoli/art-47-classificazione-dei-veicoli.html (visited on 02/27/2021) (cit. on pp. 85, 102).

[60] VI-grade GmbH. *Politecnico di Milano announces the world's first commercial installation of the DiM400 dynamic driving simulator*. URL: https://www.vi-grade.com/en/about/news/politecnico-di-milano-announces-the-world-s-first-commercial-installation-of-the-dim400-dynamic-driving-simulator_1203/ (visited on 03/23/2021) (cit. on p. 93).

[61] T. Argentini et al. 'A case-study of double multi-modal bridge flutter: Experimental result and numerical analysis'. In: *Journal of Wind Engineering and Industrial Aerodynamics* 151 (2016), pp. 25–36 (cit. on p. 94).